

SOURCE PARAMETERS OF UTTARKASHI EARTHQUAKE OF OCTOBER 19, 1991 BY WAVEFORM MODELLING

A THESIS

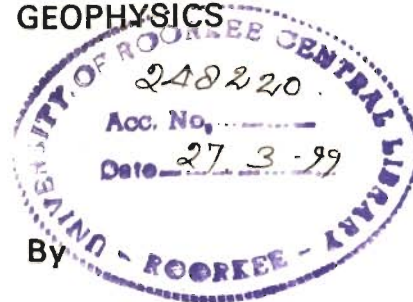
*submitted in fulfilment of the
requirements for the award of the degree*

of

DOCTOR OF PHILOSOPHY

in

APPLIED GEOPHYSICS



By

AJAY PAUL



DEPARTMENT OF EARTH SCIENCES
UNIVERSITY OF ROORKEE
ROORKEE-247 667, INDIA

DECEMBER, 1997

CANDIDATE'S DECLARATION

I hereby certify that the work which is being presented in the thesis entitled "**SOURCE PARAMETERS OF UTTARKASHI EARTHQUAKE OF OCTOBER 19, 1991 BY WAVEFORM MODELLING**" in fulfilment of the requirement of the award of the Degree of Doctor of Philosophy and submitted in the Department of Earth Sciences of the University is an authentic record of my own work carried out during a period from January 1993 to December 1997 under the supervision of **Prof. V. N. Singh**.

The matter presented in this thesis has not been submitted by me for the award of any other degree of this or any other University.



(AJAY PAUL)

Signature of the candidate

This is to certify that the above statement made by the candidate is correct to the best of my knowledge.

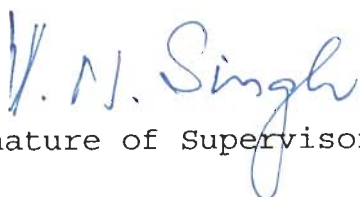


(Prof. V. N. SINGH)

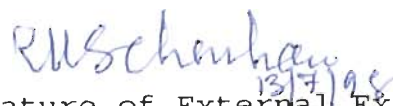
Signature of Supervisor

Date : December 12, 1997

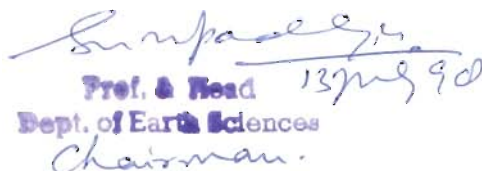
The Ph.D. Viva-Voce examination of AJAY PAUL, Research Scholar has been held on July 13, 1998



Signature of Supervisor



Signature of External Examiner



Prof. & Head 13/7/98
Dept. of Earth Sciences
Chairman.

ABSTRACT

A detailed analysis of strong motion data recorded during an earthquake makes it possible to infer the physics of the earthquake source which is quite complicated and can be difficult to work out. The faulting process (Mikumo and Miyatake, 1987) during an earthquake may be highly inhomogeneous. The distribution of slip (Wald et al., 1991) over the fault can vary both in amount and direction. There are regions on the fault where large slip might occur which corresponds to asperities. Regions of small slip are found to be close to regions of aftershock activity. Some details of this variability of slip distribution over the fault plane can be inferred from modelling of strong motion data.

In the present work the strong motion data recorded during the 1991 Uttarkashi earthquake have been modelled. The source parameters of the earthquake as given by USGS were chosen as the starting point. The objective was to determine whether these parameters need any modification to generate synthetic accelerograms. The details of the slip distribution and the orientation and location of fault plane in relation to recording stations were found to be important factors. All these aspects were considered in generating the strong motion synthetics.

The Uttarkashi Earthquake of October 19, 1991 (Ms = 7.0) occurred in Garhwal Himalayas. Its epicentre was located to the north of the Main Central Thrust (MCT) in the Higher Himalayan sub-province which is composed of crystalline rocks. The epicentre of this earthquake was located about 58 km from the site of the 268 m high Tehri dam which is under construction in the lesser Himalayas. A detailed study of the strong motion data, at seven of the thirteen stations (Chandrasedkaran and Das, 1992) where it was recorded, has been used to learn about the details of the source of this earthquake.

For the purposes of modelling the earthquake source has been represented by a number of point shear dislocations distributed over the model fault plane buried in an elastic, homogeneous and isotropic half space. The ground motion at a near distance has been calculated by adopting a simplified source radiation process and making use of simple theory (Aki and Richard, 1980). The method adopted consists in integrating the far field contributions of Green's function for a number of point sources distributed at the observation point. The radiation begins at the focus where the rupture initiates and moved outwards. The fault is divided into number of sub-faults, all of them of the same size (1km X 1km). The computational process has been so designed that it represents radiation from a circular rupture front, i.e., all sub faults where rupture front reaches at the same time, radiate simultaneously. Radiation pattern

terms have been evaluated for each subfault separately and effect of the free surface has also been taken into account in an adequate manner. The rupture propagates at a constant speed and the direction of slip vector remains the same during the entire rupture process. The source pulse is taken as a step function with a finite rise time and rounded shoulders (Ben Menahem and Singh, 1981).

The location of the point of initiation of rupture, rise time and rupture velocity along with slip amplitude distribution on the fault plane are of critical importance in obtaining a good match of synthetic accelerograms with the observed ones. A number of numerical experiments were carried out to arrive at the proper values of the above mentioned parameters. Synthetic accelerograms have been generated at seven recording stations and compared with the observed ones following the arrival of S waves.

The present study has demonstrated that simple theory applied for an elastic half space earth model, taking a simple source pulse and a fault plane with varying slip amplitude are able to reproduce most of the important features of recorded accelerograms. A pattern of slip distribution has been obtained on the fault plane.

The results obtained in the present study are comparable to the other results obtained for this earthquake,

e.g., Khattri et al. (1994). The importance of present work lies in the fact that the technique used for generating strong motion synthetics is very simple and has been applied for the case of a simple earth model (half space). This technique needs specification of a limited set of input parameters which are easy to specify yet yields good results.

ACKNOWLEDGEMENTS

With a deep sense of gratitude I would like to thank my supervisor **Prof. V. N. SINGH** for his guidance, immense help and encouragement and for providing a healthy professional environment during the course of my research work. It is because of his total cooperation that I am able to complete the present work.

I express my sincere thanks to **Prof. S. K. Upadhyay**, Head of the department, for his kind help in providing me the departmental facilities as and when required. I am also grateful to **Prof. A. K. Jain** former head, for his invaluable help during his tenure.

I am grateful to **Prof. R. Chander** for his kind help , valuable suggestions and moral support at various stages of the work.

I am thankful to **Prof. H. Sinvhal**, **Dr. (Mrs) I. Sarkar** , **Dr. D. C. Sirivastava**, **Dr. P. K. Gupta**, **Dr. Kamal** and **Dr. (Mrs.) Kalpana** from the department of Earth Sciences, **Dr. M. L. Sharma**, **Dr. Vineet Gehlaut**, **Dr. J. D. Das** and **Mr. Subhash Gupta** (Scientist) of the department of Earthquake Engineering, **Mr. R. Dharamraj** (Scientist) of the Central Building Research Institute, **Prof. K. N. Khattri** and **Dr. Sushil Kumar** of the Wadia


Institute of Himalayan Geology for the help in carrying out this work.

I am also thankful to all my colleagues and friends who assisted me in different ways during my stay at the department. Those who deserve special mention include **Pradeep, Nipun, Paras, Ajay Jayprakash, Premanand and Rakesh.**

It would have been a difficult job for me to complete this task without support from my **parents** and my wife (**Seema**). Their encouragement and moral support helped me to complete the work. I use to feel an immense pleasure to hear " Wish you good luck" every morning, from my child (**Anu**), when I start from my place for the work.

I would also like to thank **Vineet, Deepak, Raju and Sanjeev** for their great help in the last stages of my work.

Finally, I express my thankfulness to all others who helped me at various points of time and are not mentioned explicitly.


(AJAY PAUL)

CONTENTS

Certificate

Abstract

Acknowledgements

Contents

List of Figures

List of Tables

| | |
|--|----|
| Chapter 1 : INTRODUCTION | 1 |
| 1.1 Preamble | 1 |
| 1.2 Uttarkashi Earthquake | 2 |
| 1.3 Seismotectonic Setup | 4 |
| 1.4 Focal Mechanism of the Uttarkashi Earthquake | 7 |
| 1.5 Strong Motion Data of Uttarkashi Earthquake | 9 |
| 1.6 Literature Review | 9 |
| 1.7 Seismological Studies of Uttarkashi Earthquake | 15 |
| 1.8 Motivation | 18 |
| 1.9 Plan of the Thesis | 19 |
| Chapter 2 : THEORY OF RADIATION FROM FINITE MOVING SOURCE | 20 |
| 2.1 Introduction | 20 |
| 2.2 Body Forces and Surface Forces | 21 |
| 2.3 Equations of Motion | 23 |
| 2.4 Stress Strain Law | 24 |
| 2.5 Reciprocity Relation | 26 |
| 2.6 Green's Function | 27 |
| 2.7 Body Force Equivalent | 30 |
| 2.8 Radiation from a Concentrated Force | 34 |
| 2.9 Radiation from a Point Double Couple Source | 38 |
| 2.10 Far Field Radiation from a Point Double Couple Source | 40 |
| 2.11 Radiation Pattern in terms of Fault Parameters | 41 |
| 2.12 Free Surface Effect | 46 |
| 2.13 Radiation from a Finite Moving Source | 53 |

| | |
|--|-----|
| Chapter 3 : COMPUTATION OF SYNTHETIC ACCELEROGRAM FOR UTTARKASHI EARTHQUAKE | 62 |
| 3.1 Introduction | 62 |
| 3.2 Source Model | 62 |
| 3.2.1 Spatio-Temporal Parameters | 64 |
| 3.2.2 Focal mechanism Solution | 66 |
| 3.2.3 Velocity Model | 69 |
| 3.2.4 The Source Time Function | 69 |
| 3.2.5 Source Size | 70 |
| 3.2.6 Slip Distribution over the Fault Plane | 74 |
| 3.3 Choice of Global Coordinate System | 77 |
| 3.4 Choice of Local Coordinate System | 78 |
| 3.5 Rotation of the Axes | 80 |
| 3.6 Computation Procedure | 81 |
| 3.7 Rupture Propagation Model | 83 |
| Chapter 4: RESULTS AND DISCUSSIONS | 87 |
| 4.1 Introduction | 87 |
| 4.2 Results | 91 |
| 4.2.1 Comparison of Observed and Synthetic Accelerograms | 91 |
| 4.2.2 Source Parameters | 121 |
| 4.2.3 Slip Distribution | 122 |
| 4.2.4 Location of the point of rupture initiation | 122 |
| 4.3 Discussion | 122 |
| Chapter 5: CONCLUSIONS | 127 |
| SUGGESTIONS FOR FUTURE WORK | 128 |
| REFERENCES | 129 |

LIST OF FIGURES

- Fig 1.1 Seismotectonic setup of the region. MCT : Main Central Thrust, MBT: Main Boundary Thrust , E: Epicenter, Utta: Uttarkashi.
- Fig 1.2 Strong motion network in Garhwal region. Filled triangles denote stations which recorded the Uttarkashi earthquake with its epicentre at E.
- Fig 2.1 A finite elastic body, with volume V and external surface S , and an internal surface Σ (modeling a buried fault) across which discontinuities may arise. The normal to Σ is ν (pointing from Σ^- to Σ^+).
- Fig 2.2 Definition of the fault orientation parameters (strike ϕ_s , dip δ), and slip direction.
- Fig 2.3 Radiation pattern of P, SV and SH wave for four elementary faults for an earthquake with focus on the surface.
- Fig 2.4 Direct and reflected rays emanating from a buried source and received at a buried receiver.
- Fig 2.5 Amplification of P and SV wave amplitude at the free surface as a function of angle of incidence.
- Fig 2.6 Unilateral faulting on a rectangular fault. (a) The fault plane. (b) ψ is the angle between the direction to the receiver and the direction of rupture propagation.
- Fig 3.1 Locations of seven selected stations with directions of L and T components. bark: Barkot, bhat: Bhatwari, ghan: Ghansyali, kote: Koteshwar, puro: Purola, tehr: Tehri, utta: Uttarkashi
- Fig 3.2 Accelerograms of Uttarkashi earthquake recorded at Uttarkashi.
- Fig 3.3 Fault plane solution, NP1: Strike 317° dip 14° , NP2: Strike 112° dip 78° , of Uttarkashi earthquake of October 19,1991, as used in this study
- Fig 3.4(a) Vertical section perpendicular to strike of the fault

showing that the fault lies in the first layer.
(b) Strike of the fault plane and dip in a three dimensional view.

- Fig 3.5 Source time function (a) slip displacement (b) slip velocity (c) slip acceleration.
- Fig 3.6 Spectrum of source time function (a) slip displacement spectrum (b) slip velocity spectrum (c) slip acceleration spectrum
- Fig 3.7 Epicentral map of the shallower aftershocks (depth < 5 km). Two elliptical volumes of the aftershocks E1 and E2 are shown. Rectangle with broken lines shows the aftershock area. (Modified after Kayal et al., 1995).
- Fig 3.8 Epicentral map of the deeper aftershocks (depth :5-26 km). An elliptical volume of the aftershocks E3 is shown. Other symbols are same as in Fig 3.7 (Modified after Kayal et al., 1995).
- Fig 3.9 Global and local coordinate systems ϕ_s : strike, δ :dip, λ :slip angle, i_o :take off angle , ϕ :azimuth of recording station, Δ : epicentral distance , E: epicentre v : fault normal
- Fig 3.10 Particle motion diagram at Uttarkashi station at the time of arrival of S wave
- Fig 3.11 Contours on the fault plane showing the travel time (in seconds) of (a) P and (b) S waves to the recording station at Uttarkashi.
- Fig 4.1 Distribution of slip amplitude on the fault plane. Contour values are in cm
- Fig 4.2(a) Observed and Synthetic accelerograms for the N10E component at Barkot
- Fig 4.2(b) Synthetic accelerogram superimposed over the observed ones for the N10E component at Barkot.
- Fig 4.2(c) Observed and Synthetic accelerograms for the N80W component at Barkot.
- Fig 4.2(d) Synthetic accelerogram superimposed over the observed ones for the N80W component at Barkot.

- Fig 4.3(a) Observed and Synthetic accelerograms for the N85E component at Bhatwari
- Fig 4.3(b) Synthetic accelerogram superimposed over the observed ones for the N85E component at Bhatwari.
- Fig 4.3(c) Observed and Synthetic accelerograms for the N5W component at Bhatwari.
- Fig 4.3(d) Synthetic accelerogram superimposed over the observed ones for the N5W component at Bhatwari.
- Fig 4.4(a) Observed and Synthetic accelerograms for the N00E component at Ghansyali.
- Fig 4.4(b) Synthetic accelerogram superimposed over the observed ones for the N00E component at Ghansyali.
- Fig 4.4(c) Observed and Synthetic accelerograms for the N90W component at Ghansyali.
- Fig 4.4(d) Synthetic accelerogram superimposed over the observed ones for the N90W component at Ghansyali.
- Fig 4.5(a) Observed and Synthetic accelerograms for the N30W component at Koteshwar.
- Fig 4.5(b) Synthetic accelerogram superimposed over the observed ones for the N30W component at Koteshwar.
- Fig 4.5(c) Observed and Synthetic accelerograms for the N60E component at Koteshwar.
- Fig 4.5(d) Synthetic accelerogram superimposed over the observed ones for the N60E component at Koteshwar.
- Fig 4.6(a) Observed and Synthetic accelerograms for the N65W component at Purola.
- Fig 4.6(b) Synthetic accelerogram superimposed over the observed ones for the N65W component at Purola.
- Fig 4.6(c) Observed and Synthetic accelerograms for the N25E component at Purola.
- Fig 4.6(d) Synthetic accelerogram superimposed over the observed ones for the N25E component at Purola.
- Fig 4.7(a) Observed and Synthetic accelerograms for the N63W component at Tehri.

Fig 4.7(b) Synthetic accelerogram superimposed over the observed ones for the N63W component at Tehri.

Fig 4.7(c) Observed and Synthetic accelerograms for the N27E component at Tehri.

Fig 4.7(d) Synthetic accelerogram superimposed over the observed ones for the N27E component at Tehri.

Fig 4.8(a) Observed and Synthetic accelerograms for the N15W component at Uttarkashi.

Fig 4.8(b) Synthetic accelerogram superimposed over the observed ones for the N15W component at Uttarkashi.

Fig 4.8(c) Observed and Synthetic accelerograms for the N75E component at Uttarkashi.

Fig 4.8(d) Synthetic accelerogram superimposed over the observed ones for the N75E component at Uttarkashi.

Fig 4.9 Rectangle shows the trace of fault plane in relation to the tectonic features (MCT and MBT) which has been used for generating synthetic accelerograms , utta: Uttarkashi

LIST OF TABLES

- Table 1.1 Focal Parameters of the Uttarkashi Earthquake.
- Table 1.2 Focal Mechanism of the Uttarkashi Earthquake.
- Table 3.1 Details of Selected stations.
- Table 3.2 Time of Arrivals of P and S Waves in Observed and Synthetic Accelerograms.
- Table 4.1 Source Parameters of Uttarkashi Earthquake of October 19,1991.
- Table 4.2 Details of the Superimposed Accelerograms.
- Table 4.3 Comparison of Source Parameters.

CHAPTER - 1

INTRODUCTION

1.1 PREAMBLE

Earthquakes are the most potent natural hazards known to mankind. The strong ground shaking in the epicentral region of a large earthquake causes considerable damage to all types of man-made structures. The risk posed by a future earthquake can be partially mitigated by earthquake resistant design of all structures, big or small. Design of a structure to resist forces induced by strong ground shaking depends critically on the ground motions used in analysing behaviour of a structure to strong shaking. For a good, effective and economic design a knowledge of site specific and realistic ground accelerations is needed. It is difficult to have a sufficient number of strong ground motion records for earthquakes having different source mechanisms, magnitudes, and for diverse site conditions. In view of the above generation of synthetic accelerograms for prescribed earthquakes and given local site conditions has been attempted by seismologists.

The computation of the ground motions (displacements, velocities and accelerations) that would be caused by a given earthquake occurring in a specified geological setting is termed

"forward modelling". Prediction of ground motion for earthquake resistant design and for determining earthquake source parameters requires the solution of the above mentioned forward problem. Computation of strong motions in the vicinity of large earthquake is more involved due to the finiteness and inhomogeneity of the earthquake source. The source mechanism of the earthquake has to be carefully specified to obtain synthetic ground motions which will compare more realistically with strong motion records. The choice of a suitable computation technique is also important.

In this thesis an attempt has been made to synthesize strong ground motion for the Uttarkashi earthquake of October 19, 1991 in order to determine source parameters of this earthquake and to obtain a model of slip distribution on the fault plane.

1.2 UTTARKASHI EARTHQUAKE

The Uttarkashi earthquake occurred on October 19, 1991 at about 21 hrs 23 min (GMT). This earthquake had a surface wave magnitude of 7.0 and body wave magnitude of 6.5. The highly damaged area was situated at and around Uttarkashi in the higher reaches of Garhwal Himalaya. It claimed about 2000 lives and caused considerable damage to property. The earthquake parameters of this earthquake as determined by different agencies are given

in Table (1.1). The location of the epicentre of this earthquake is to the north of the Main Central Thrust (MCT) in the Higher Himalayan sub-province which is composed of crystalline rocks. The Higher Himalaya are bounded to the south by MCT. To the south of MCT lie the lesser Himalayan sub-province which is composed of meta-sedimentary formations. The occurrence of this well

Table - 1.1

FOCAL PARAMETERS OF THE UTTARKASHI EARTHQUAKE

| Sl. No. | Source | Epicentral Location | Focal Depth (km) | Origin Time (hh:mm:ss) |
|---------|--------------------------------|----------------------|------------------|------------------------|
| 1 | PDE Weekly | 30.738 N 78.792 E | 19 | not reported |
| 2 | PDE Monthly October 1991 | 30.780 N 78.774 E | 10 | 21:23:14.3 |
| 3 | IMD | 30.75 N 78.86 E | 12 | not reported |
| 4 | CMT Havard | 30.22 N 78.24 E | 15 | 21:23:21.6 |

recorded large earthquake to the north of surface trace of MCT falsified the notion that MCT and the Higher Himalayan subprovince to the north of it, are aseismic (Khattari et al., 1994).

The Uttarkashi earthquake was also notable from another point of view. Its epicentre lies at an estimated distance of 54km from the site of 260m high Tehri dam, under construction, in the Lesser Himalaya. The occurrence of this earthquake has raised many questions regarding safety of Tehri dam in the event of a future large earthquake. A detailed study of this earthquake is a must to understand the nature of earthquake sources in Garhwal Himalaya and the seismic hazard to which this region will be subjected to in future.

1.3 SEISMOTECTONIC SETUP

Fig. 1.1 shows the seismotectonic setup of the region. The earthquakes in this region are caused by the strain generated by the convergence of the Indian and the Eurasian plates. The Indian plate is moving at a rate of 5 cm/yr relative to the Eurasian plate in a north easterly direction (Yu et al., 1995). There are three major sets of active northward dipping thrusts namely Main Central Thrust (MCT), Main Boundary Thrust (MBT) and Himalayan Frontal Thrust (HFT). Along these thrusts, slabs of the subducting Indian plate have piled southward. These thrusts, form the boundaries of geological subprovinces having characteristic geology and physiography (Gansser, 1964). Along the MCT the crystallines of the Higher Himalaya (Precambrian) are

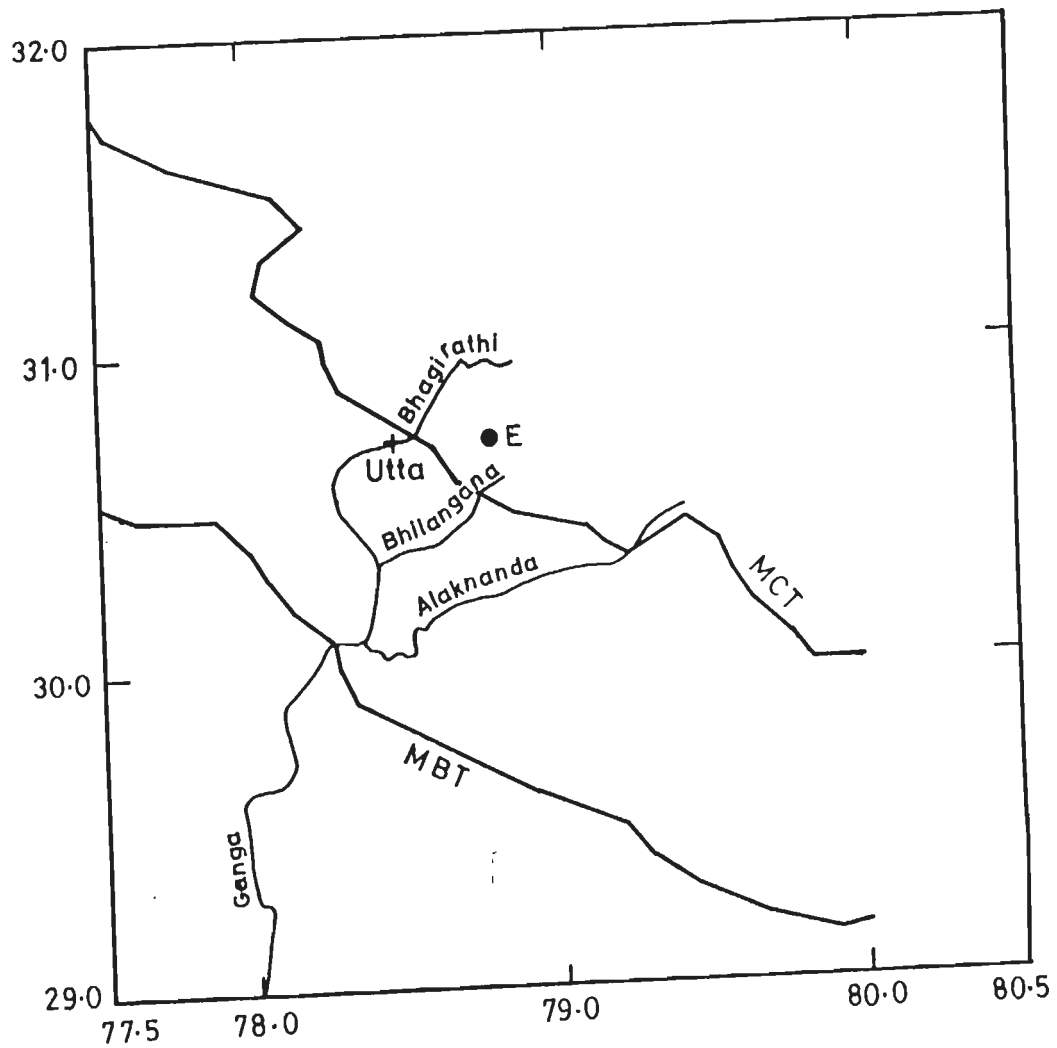


Fig 1.1 Seismotectonic setup of the region. MCT : Main Central Thrust, MBT: Main Boundary Thrust , E: Epicenter, Utta: Uttarkashi.

overthrust southward and have overridden the metasedimentary formations (Paleozoic) of the lesser Himalaya. These formations of lesser Himalayas have overridden the mollassic Siwalik (Cenozoic) sedimentary formations of the outer Himalaya along the MBT. Along HFT, sediments of the Ganga foredeep to the south are overridden by Shiwaliks. The formations lying to the north of MBT are highly folded and thrust.

The area is characterised by high seismicity. The highest seismic activity is confined to a narrow zone which follows the Himalayan trend and lies south of surface trace of the MCT. The foci of most of the earthquakes in this zone lie in the upper 20km of the crust (Ni and Barazangi, 1984). The fault plane solutions are mostly of thrust type with the P-axis normal to the trend of the Himalayan arc. One of the nodal planes in most of the fault plane solutions is shallow dipping towards the northeast in conformity with the surface geological evidence thrusting (Yu et al., 1995).

Seismicity studies based on microearthquake recording using local networks have shown that MCT lies to the south of the belt of local seismicity in a local region. The composite fault plane solutions based on these microearthquake studies show thrust as well as strike slip mechanism (Khatti, 1992a,b).

1.4 FOCAL MECHANISM OF THE UTTARKASHI EARTHQUAKE

The various focal mechanism solutions of the Uttarkashi earthquake are given in Table 1.2. For the purpose of forward modelling in this study the following solution has been used as the initial model.

$$\text{Seismic Moment } (M_0) = 1.8 \times 10^{26} \text{ dyne-cm}$$

$$M_s = 7.0$$

$$m_b = 6.5$$

$$M_w = 6.8$$

NP1 : strike 317° , dip 14° , slip 115°

NP2 : strike 112° , dip 78° , slip 84°

The epicentral location used in this study is the one determined by IMD as given in table 1.1. This is based on local and regional data and is likely to be closest to the actual epicentre. The focal depth used here is 10km (PDE monthly, October 1991)

Table 1.2

FOCAL MECHANISM OF THE UTTARKASHI EARTHQUAKE

| Sl. No. | Source | Focal Mechanism | Size M_0 (dyn-cm) |
|---------|-----------------------------|---|------------------------|
| 1 | PDE Weekly | NP1: strike332,dip 19,slip 133 NP2: strike108, dip 76,slip 77 | 1.0×10^{25} |
| 2 | PDE monthly October 1991 | First P-motion Solution NP1:strike 296, dip 5, slip 90 NP2:strike 116, dip 85,slip 90 Moment Tensor Solution NP1:strike 18, dip 38,slip 172 NP2:strike 115, dip 85,slip 52 | 1.8×10^{26} |
| 3 | CMT (Harvard) | Centroid Moment-Tensor Solution NP1:strike 317, dip 14,slip 115 NP1:strike 112, dip 78,slip 84 | 1.8×10^{26} |

M_0 : Seismic Moment

1.5 STRONG MOTION DATA OF UTTARKASHI EARTHQUAKE

A strong motion network of 28 stations has been installed in this region and is shown in Fig. 1.2. The instruments are Kinematics SMA - 1 accelerographs. These are triggered instruments which record three orthogonal components of acceleration on 70mm film, of the total of 28 strong motion accelerographs, 13 recorded the Uttarkashi earthquake (Chadrsekaran and Das, 1992b). The geological data on local site condition is not available. The stations are located in mountainous terrain. The effects of topography on recorded accelerations at many sites are expected to be significant.

The analog data have been converted into digital format by Chandrasekaran and Das (1992a). The sampling interval of the digital data is 0.02 sec and it has been bandpass filtered (0.17, 0.20 ; 25.0, 27.0 Hz) using an Ormsby filter. This processing may have resulted in filtering out of low frequency signals (with significant amplitudes) from recorded accelerograms. The digital data processed in this manner represents ground accelerations.

1.6 LITERATURE REVIEW

In strong motion seismology earthquakes of magnitude 5 or

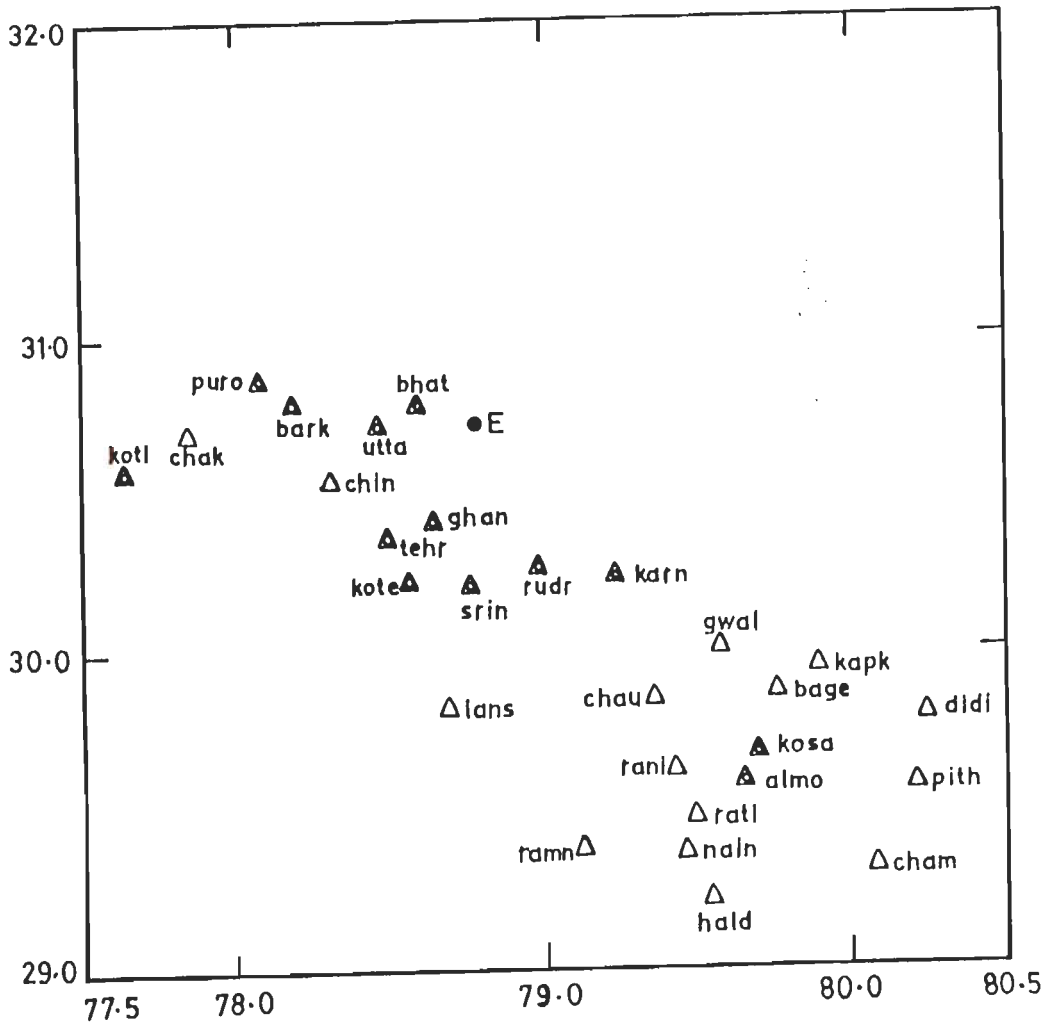


Fig 1.2 Strong motion network in Garhwal region. Filled triangles denote stations which recorded the Uttarkashi earthquake with its epicentre at E.

greater are considered important in view of their damage potential. Even in great earthquakes potentially damaging effects of earthquakes are observed within distances of several tens of kilometers of the causative fault (with some notable exceptions, e.g., Michoacan earthquake of September 19,1985). The ground motion recorded in the nearfield of large earthquakes is essentially of high frequency. Such high frequency ground motion is not recorded very often. Sufficient progress has however, been made over the past 25 years in understanding the mechanism of generation of high frequency waves during large earthquakes. This has been made possible due to the availability of digital accelerograms and the need for development of efficient mathematical tools for generating synthetic accelerograms.

The mathematical foundation of the various methods of strong motion synthetics was firmly established in the early sixties, Maruyama(1963) and Burridge and Knopoff(1964) showed that the body force equivalent of a point shear dislocation is a double couple and that a synthetic seismogram can be constructed by a space-time convolution of the slip function and Green's function. The slip function describes the form of fault displacement as a function of time and position of the fault plane. Green's function is the response of earth when an impulsive double couple is applied at a point on the fault plane. The slip function and Green's function express quantitatively the

source and propagation effect, respectively, on seismic motion.

The earliest and most fundamental synthesis of strong ground motion was carried out by Aki(1968) and Haskell(1969) based on Green's function approach. The response of horizontally layered crustal structure to a double couple point source has been computed using a number of techniques, e.g., generalized ray theory (Helmberger,1968; Heaton and Helmberger, 1977, 1978), the Cagniard-deHoop method (Helmberger and Harkrider), reflectivity methods (Fuchs and Mueller,1971;), direct frequency domain integration (Herrmann,1977),the normal mode method(Swanger and Boore, 1978), the discrete wave-number method (Bouchon,1979) and by the discrete wave number/finite element method (Olson,1982). Some of these methods generate the complete response of the medium, including all types of body and surface waves.

The above methods, however, do not take into account the real structure of the earth around fault zones which is in general more complicated than assumed. The earth in the vicinity of faults is characterised by lateral heterogenities, attenuation properties and local topographical site effects. Due to these complexities complete modelling with any given method is quite difficult. To overcome this difficulty Hartzell(1978) presented a semi-empirical approach in which strong ground motions from a large earthquake are modelled by using the aftershock records as

an empirical earth response. This is based on the premise that the ground motion associated with a small event may be regarded as a Green's function if its source can be approximated as a point source on the fault on which a large earthquake takes place.

This approach has been employed to predict the velocity spectra, peak accelerations and the maximum duration of ground motion from large earthquakes with complex multiple events (Hadley and Helmberger, 1980)

The models of earthquake source in the methods described above are kinematic in nature. In these models some simplifying assumptions are made in a somewhat arbitrary manner on the process of rupture propagation over the fault plane and the displacement time history. These models do not take into consideration the stress conditions on and around the fault. For a comprehensive understanding of complex ground motions in the near field in the event of a large earthquake, modelling of the actual rupture process must be done. This includes initiation, propagation and stoppage of the rupture of the fault plane. The development of dynamic slip motions under shearing stresses are modelled. An approach along this line considers faulting process as a propagating shear crack by taking into the initial stress field, friction and cohesive forces on the fault (Kostrov, 1966).

Dynamic crack problems have been solved analytically and numerically for two dimensional in-plane and anti-plane shear cracks growing at a constant velocity or with self similar propagation under different fracture criteria and boundary conditions (Burridge and Halliday, 1971; Ida and Aki,1972; Das and Aki,1977 a,b). It has been found that the results from the two dimensional crack studies are incomplete when compared with observations. Three dimensional modelling of the spontaneous rupture process has been carried out by Madariaga,1976, Mikumo and Miyatake,1978)

Haskell(1966) introduced a model involving statistical randomness of fault slip along the fault plane. In this model the fault displacement is represented by coherent waves only over segments of the fault and radiations from adjacent sections are assumed to be statistically independent or incoherent. Das and Aki (1977 a,b) considered a fault plane having various barriers distributed over it. Rupture starts near one of the barriers and then propagates over the fault plane until it was brought to rest or slowed at the next barrier. Sometimes the barriers are broken by the dislocation; sometimes the barriers remain unbroken but the dislocation reinitiates on the far side and continues; sometimes the barriers are not broken initially but, because of local repartitioning of the stresses and possibly non-linear effects, it eventually breaks, usually with the occurrence of

aftershocks.

Some of the recent attempts on new approaches to synthesize strong ground motion and inversion of strong motion records to obtain source parameters include those of Somerville et al. (1990), Somerville et al. (1991), Ahrhanson et al. (1990), Makaris et al. (1992), Mendoza and Hartzell (1988), Barker et al. (1988, 1989), Wald (1991), Zeng et al. (1993 a,b), Zeng et al. (1994a,b), Khattri et al. (1994), Yu et al. (1995).

1.7 SEISMOLOGICAL STUDIES OF THE OF THE UTTARKASHI EARTHQUAKE

The Uttarkashi Earthquake of October 19, 1991 has been declared to be the most significant earthquake of the year 1991. Prior to this earthquake a magnitude 7.3 earthquake had occurred on August 6, 1988 in a rather sparsely populated region of Indo-Burma border and had a focal depth of above 100km (Gupta and Gupta, 1995). This earthquake did not draw much attention. The Bihar-Nepal earthquake of August 20, 1988 had a magnitude of 6.6 which claimed 1000 human lives in India and Nepal. The Uttarkashi earthquake has been studied extensively. Some of the important such studies are briefly described below.

Narula et al. (1995) and Rastogi and Chadha (1988) analysed the damage pattern and presented isoseismals for this earthquake.

Kayal et al. (1995) reported the results of aftershock activity for a 33 day period from November 3, 1991 through December 5, 1991. During this period about 600 aftershocks were recorded of which 124 could be located. From the distribution of the aftershocks the presence of a thrust, parallel to the Main Central Thrust and located south of it and responsible for the October 19, 1991 main shock and its aftershocks was inferred. Rastogi (1995) reported the focal mechanism solution for the Uttarkashi earthquake.

Chadha (1995) made use of the focal mechanism solution for the main-shock obtained by the United States Geological Survey, field observations and trend of the aftershocks to infer that the block between the Bhagirathi and Bhilangana river has been thrust under a northwest-southeast fault causing the earthquake.

Chandrasedkaran and Das (1992a,b), Chandra et al. (1995) and Jain and Das (1995) studied and analysed the strong motion data recorded at 13 stations during the earthquake. It has been found that the maximum horizontal acceleration recorded was 304 cm/sec^2 (at Uttarkashi station) and the maximum vertical acceleration recorded was 289 cm/sec^2 (at Bhatwari station). From the shape of the spectra it was found that energy is concentrated in the frequency range 5-10 Hz.

Jain and Chander (1995) proposed two dynamic models for the Uttarkashi earthquake. The first of these two models implies origin of the earthquake along a gently inclined basal detachment in the Garhwal Himalaya at a depth of about 10 km. The second model implies occurrence of the Uttarkashi earthquake within the flats of the Main Central Thrust and its splays merging with the basal detachment.

Khattari et al. (1994) and Yu et al. (1995) carried out synthesis of strong motion for the Uttarkashi earthquake. Khattri et al. (1994) carried out the forward modelling using the isochrone method and inverted the observed accelerograms by recursive stochastic inverse algorithm to obtain the earthquake source slip function and slip distribution over the fault plane. It was found that slip was highest in two localities, one around the hypocentre, and the other, the larger, further westward. The largest slip value obtained was 300cm.

Yu et al. (1995) generated synthetics using the composite source model and synthetic Green's function. The synthetic accelerograms so produced matched the observed accelerograms in a realistic manner. The strong ground motion expected from a possible future earthquake of magnitude 8.5 was also predicted for a hypothetical source model.

1.8 MOTIVATION

A number of computational techniques have been devised for solving the forward problem in strong motion seismology, viz., predicting the form of acceleration time history at a given point on the earth's surface for an earthquake with prescribed source mechanism. The source mechanism includes following specifications: location and orientation of the fault plane in terms of its dip and strike, distribution of slip on the fault plane, source time function, dimensions of the fault plane and location of the point on the fault plane (i.e., the focus) at which the rupture initiates. Other specifications relate to properties of the medium between the fault and receiving point on earth's surface, details of recording instrumentation, etc. The properties of the intervening medium may be prescribed in terms of its velocity structures, e.g., in terms of a layered earth model and its Q structure if the effect of frequency dependent attenuation on predicted ground motion are sought to be included. In addition the effect of topography near the point of observation may also be considered.

The solution of forward problem carried out by Yu et al. (1995) have taken into account the velocity structure in the Uttarkashi area and its Q structure. The computational techniques on which the solution is based are quite involved. The method of

generating synthetics, depends on the knowledge of many input parameters like velocity and Q structure of the layered earth model. The composite source model itself requires sufficient computational effort.

The present work is aimed at presenting a simple method of solving the forward problem and generating a synthetic accelerogram based on simple and straight forward application of geometric ray theory. The input data required to solve the forward problem are minimal and are easy to specify. The computational effort is quite modest giving results which are quite acceptable.

1.9 PLAN OF THE THESIS

Chapter 2 presents a brief description of the theoretical framework of the mathematical formulation used in this work for generating synthetic accelerograms. In Chapter 3 the details of computational strategy are presented. The results of the computations have been presented and discussed in Chapter 4 followed by conclusions arrived at in Chapter 5.

Chapter-2

THEORY OF RADIATION FROM FINITE MOVING SOURCE

2.1 INTRODUCTION

The basic physical model for the computation of synthetic accelerograms is contained in the elastic rebound theory, first proposed by H.F.Reid, on the basis of the studies of the 1906 San Francisco earthquake. According to this model strains are built up in the faulted rocks until a failure point is reached. Rupture then takes place and the strained rock rebounds on each side of the fault under its own elastic stress until the strain is largely or wholly relieved. The whole movement is not instantaneous but proceeds in irregular steps. Rupture starts suddenly and also stops suddenly producing vibrations which propagate to large distances. The rupture propagation over the fault is not smooth but is subject to irregular variations related to roughness of the fault plane (Abrahamson and Bolt, 1986).

The computation of the synthetic accelerograms in the near field is thus based on a dislocation moving over a fault plane. The computed ground motions have to take into account the radiation pattern effects, presence of free surface (i.e., the free surface effect), layering in the earth between the

source and free surface, and effect of finite moving source. In the kinematic approach time history of the slip on the causative fault is specified in terms of shape, rise time and amplitude of the source time function. In addition velocity of rupture propagation and final area over which slip occurred are also specified. The computation of synthetic accelerograms in the present work is based on the Green's function approach. In the following paragraphs theoretical basis of such an approach is presented which is based on the treatment of the subject given in Aki and Richards (1980). This approach makes it possible to compute synthetic accelerograms from a finite moving source.

2.2 BODY FORCES AND SURFACE FORCES

In order to synthesize and interpret seismograms there is a need to know how to characterize a seismic source (e.g. an explosion or a spontaneous fault motion) and how to satisfy boundary conditions at the earth's free surface. For an elastic medium this problem has a definite solution. When an elastic medium is deformed internal forces come into existence which tend to resist this deformation. These internal forces act mutually between adjacent particles within elastic medium. These forces consist of (a) contact forces between adjacent particles, (b) forces between particles that are not adjacent and (c) forces due to the application of physical processes external to the medium

itself.

The contact forces between adjacent particles are expressed in terms of traction and stress tensor. Traction is a vector, being the force per unit area across an internal surface within the elastic continuum and quantifies the contact force (per unit area) with which particles on one side of the surface act upon particles on the other side. For a given point of the internal surface traction is defined by considering the infinitesimal force $\delta\mathbf{F}$ acting across an infinitesimal area δS of the surface and taking the limit of $\delta\mathbf{F}/\delta S$ as $\delta S \rightarrow 0$. With a unit normal \mathbf{n} to the surface the traction is denoted as $\mathbf{T}(\mathbf{n})$. The stress tensor p_{ij} is introduced through the following relation

$$T_i = P_{ij}n_j \quad (i, j = 1, 2, 3) \quad \dots (2.1)$$

The stress tensor P_{ij} is the j^{th} component of traction acting across the plane normal to the i^{th} axis, and has the property that $P_{ji}=P_{ij}$, i.e., stress tensor is symmetric.

The non-contact forces (b) and (c) are known as body forces and are denoted by $\mathbf{f}(\mathbf{x}, t)$ which represents the body force acting per unit volume on the particle originally at \mathbf{x} at some reference time t . An impulsive type of body force in the direction of x_n -axis acting on a particle situated at $\mathbf{x} = \mathbf{y}$ and time $t = \tau$ is

represented as

$$f_i(\mathbf{x}, t) = A \delta(\mathbf{x}-\mathbf{y}) \delta(t-\tau) \delta_{in} \quad (n=1,2,3) \quad \dots (2.2)$$

where A is a constant giving strength of an impulse.

2.3 EQUATIONS OF MOTION

Consider an elastic body occupying a volume V with a surface S with outward normal \mathbf{n} . If unbalanced tractions and body forces act throughout V, this body will move in the direction of the resultant of these forces with a certain acceleration. By equating the rate of change of momentum of particles constituting V to the forces acting on these particles the following relation is obtained

$$\left(\frac{\partial}{\partial t}\right) \int \int \int_V \rho (\partial \mathbf{u} / \partial t) dV = \int \int \int_V \mathbf{f} dV + \int \int_S \mathbf{T}(\mathbf{n}) dS \quad \dots (2.3)$$

where \mathbf{u} is particle displacement and ρ the density of the medium. The left hand side can be written as $\int \int \int_V \rho (\partial^2 \mathbf{u} / \partial t^2) dV$ since the particle mass (ρdV) is constant in time.

Applying Gauss's divergence theorem to the surface integral in equation (2.3) and using equation (2.1) yields equation of motion of a general particle. This is given by

$$\rho (\partial^2 u_i / \partial t^2) = f_i + \partial p_{ij} / \partial x_j \quad \dots (2.4)$$

where u_i represents i^{th} component of displacement vector \mathbf{u} and f_i ,

the i^{th} component of body force \mathbf{f} .

2.4 STRESS-STRAIN LAW

The distortion of a medium is expressed in the form of a strain tensor, denoted as e_{ij} and is defined as

$$e_{ij} = \frac{1}{2} (\partial u_i / \partial x_j + \partial u_j / \partial x_i) \quad \dots (2.5)$$

The strain tensor is also a symmetric tensor.

An elastic medium is said to possess a natural state (in which strains and stresses are zero) to which it will revert when applied forces are removed. When external forces are applied to an elastic medium, stress and strains will change together and the relation between them is described by a constitutive relation.

The generalized Hooke's law states that each component of the stress tensor is a linear combination of all components of the strain tensor i.e., there exist elastic constants C_{ijkl} such that

$$p_{ij} = C_{ijkl} (\partial u_k / \partial x_l) \quad \dots (2.6)$$

A body which obeys relation (2.7) is said to be linearly elastic.

The quantities C_{ijkl} are components of a fourth order tensor and here the symmetries

$$C_{jikl} = C_{ijkl} \quad , \text{ (due to } p_{ji}=p_{ij} \text{)} \quad \dots (2.7)$$

$$C_{ijlk} = C_{ijkl} \quad , \text{ (due to } e_{lk}=e_{kl} \text{)} \quad \dots (2.8)$$

and $C_{klij}=C_{ijkl}$ (due to existence of strain energy function) ... (2.9)

The C_{ijkl} are independent of strain. The symmetries given by relations (2.7), (2.8) and (2.9) reduce the number of independent components of C_{ijkl} from 81 to 21. Substituting relation (2.6) in equation (2.4) one gets

$$\rho \partial^2 u_i / \partial t^2 = f_i + (\partial / \partial x_j) C_{ijkl} (\partial u_k / \partial x_l) \quad \dots (2.10)$$

For a perfectly elastic , homogeneous and isotropic solid the stress strain relationship is given by the simpler form of Hooke's law

$$p_{ij} = \lambda \theta \delta_{ij} + 2\mu e_{ij} \quad \dots (2.11)$$

where $\theta = \text{div } \mathbf{u}$ and is called cubical dilatation. It expresses volumetric strains developed in a medium under stress. The two independent constants λ and μ are known as Lamé's constants.

2.5 RECIPROCITY RELATIONSHIP

The displacements produced in an elastic body on the application of body forces alone or surface forces alone or a combination therefore must satisfy equation (2.4). Specification of the body forces throughout V and tractions all over S is enough to determine uniquely the displacement field that will develop throughout V from given initial conditions. This is insured by the uniqueness theorem which states that the displacement $\mathbf{u}=\mathbf{u}(\mathbf{x},t)$ throughout the volume V with surface S is uniquely determined after time t_0 by the initial values of displacement and particle velocity at t_0 , throughout V ; and by values at all times $t \geq t_0$ of (i) the body forces \mathbf{f} and the heat Q , if any, supplied throughout V ; (ii) the tractions \mathbf{T} over any part S_1 of S ; and (iii) the displacement over the remainder of S with $S_1+S_2=S$. According to Betti's reciprocity theorem the displacement field $\mathbf{u}=\mathbf{u}(\mathbf{x},t)$ due to body forces \mathbf{f} and boundary condition on S and initial conditions at time $t=0$, and another displacement field $\mathbf{v}(\mathbf{x},t)$, body forces \mathbf{g} and a different set of boundary conditions and initial conditions at $t=0$ are related to each other by the following relation.

$$\iiint_V (\mathbf{f}-\rho\dot{\mathbf{u}}) \cdot \mathbf{v}dV + \iint_S \mathbf{T}(\mathbf{u},\mathbf{n}) \cdot \mathbf{v}ds = \iiint_V (\mathbf{g}-\rho\dot{\mathbf{v}}) \cdot \mathbf{u}dV + \iint_S \mathbf{T}(\mathbf{v},\mathbf{n}) \cdot \mathbf{u}ds \quad \dots (2.12)$$

where $\mathbf{T}(\mathbf{v},\mathbf{n})$ is used for traction due to \mathbf{u} and similarly for $\mathbf{T}(\mathbf{u},\mathbf{n})$. Betti's theorem does not involve initial conditions for

\mathbf{u} or \mathbf{v} . This theorem remains true even if the quantities $\mathbf{u}, \ddot{\mathbf{u}}, \mathbf{T}(\mathbf{u}, \mathbf{n})$ and \mathbf{f} are evaluated at a time t_1 but $\mathbf{v}, \dot{\mathbf{v}}, \mathbf{T}(\mathbf{v}, \mathbf{n})$ and \mathbf{g} are evaluated at a different time $t=t_2$. If $t_1=t$, $t_2=\tau-t$ and there is a time τ_0 before which \mathbf{u} and \mathbf{v} everywhere are zero throughout V then integrating equation 2.11 w.r.t t from $-\infty$ to ∞ gives

$$\int_{-\infty}^{\infty} dt \iiint_V \{ \mathbf{u}(\mathbf{x}, t) \cdot \mathbf{g}(\mathbf{x}; \tau-t) - \mathbf{v}(\mathbf{x}, \tau-t) \cdot \mathbf{f}(\mathbf{x}, t) \} dV$$

$$= \int_{-\infty}^{\infty} dt \iiint_S \{ \mathbf{u}(\mathbf{x}, \tau-t) \cdot \mathbf{T}(\mathbf{u}(\mathbf{x}, t), \mathbf{n}) - \mathbf{u}(\mathbf{x}, t) \cdot \mathbf{T}[\mathbf{v}(\mathbf{x}, \tau-t), \mathbf{n}] \} \dots (2.13)$$

2.6 GREEN'S FUNCTION

The earthquake source is complicated since it extends over a finite area (the fault plane) and over a finite amount of time. The rupture process produces dislocations over the fault which vary both in direction and magnitude. The displacement produced by such a realistic but complicated source model can in fact be synthesized from the displacement produced by the simplest of sources - the one which is localized precisely both in space and time. This is the unidirectional unit impulse. The displacement field from such a simple source is the elastodynamic Green's function. In equation (2.2) taking A =unit constant with dimension of impulse, the i^{th} component of displacement at general (\mathbf{x}, t) is denoted by $G_{in}(\mathbf{x}, t; y, \tau)$.

This Green's function is a tensor. G_{in} depends on both receiver and source coordinates and satisfies the equation

$$\rho(\partial^2/\partial t^2)G_{in} = \delta_{in} \delta(\mathbf{x}-\mathbf{y}) \delta(t-\tau) + (\partial/\partial x_j) [c_{ijkl} (\partial G_{km}/\partial x_l)] \dots (2.14)$$

throughout V . The following initial conditions are used

$$\begin{aligned} G(\mathbf{x}, t; \mathbf{y}, \tau) &= 0 \\ (\partial/\partial t) \{G(\mathbf{x}, t; \mathbf{y}, \tau)\} &= 0 \end{aligned} \dots (2.15)$$

for $t \leq \tau$ and $\mathbf{x} \neq \mathbf{y}$

If the boundary conditions are independent of time which will be the case when S is always rigid, the time origin can be shifted at will and \mathbf{G} depends on t and τ in the form of a combination $t-\tau$. Hence

$$\begin{aligned} G(\mathbf{x}, t; \mathbf{y}, \tau) &= G(\mathbf{x}, t-\tau; \mathbf{y}, 0) \\ &= G(\mathbf{x}, -\tau; \mathbf{y}, -t) \end{aligned} \dots (2.16)$$

which expresses the reciprocal relation for source and receiver times. If \mathbf{G} satisfies homogeneous boundary conditions on S then using equation (2.12) the following reciprocal relation for source and receiver positions are obtained.

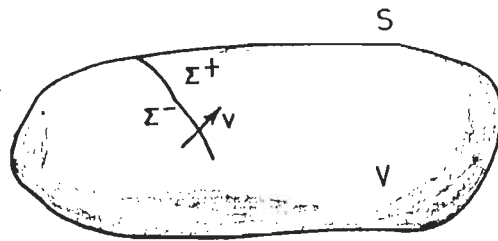


Fig 2.1 A finite elastic body, with volume V and external surface S , and an internal surface Σ (modeling a buried fault) across which discontinuities may arise. The normal to Σ is v (pointing from Σ^- to Σ^+).

$$G_{mn}(Y_2, \tau ; Y_1, 0) = G_{mn}(Y_1, \tau ; Y_2, 0) \quad \dots (2.17)$$

$$G_{mn}(Y_2, \tau_2 ; Y_1, \tau_1) = G_{mn}(Y_1, -\tau_1 ; Y_2, -\tau_2) \quad \dots (2.18)$$

Relation (2.17) expresses a purely spatial reciprocity whereas relation (2.18) a space time reciprocity.

2.7 BODY FORCE EQUIVALENTS

The theory of elastic rebound proposed by H.F.Reid led to the general recognition that ground motion caused by an earthquake is due to waves radiated from spontaneous slippage on active geological faults. The theory outlined above can be used to determine body force equivalents of slip on a fault. Towards this end the surface of V is taken to consist of an external surface labelled S (Fig 2.1) and two adjacent internal surfaces, labelled Σ^+ and Σ^- which represent opposite faces of the fault. In case of slippage across Σ , the displacement field has a discontinuity there. The equation of motion is now satisfied throughout the interior of $S+\Sigma^++\Sigma^-$.

In equation (2.12) the body force $g_i(\mathbf{x},t)$ is replaced with $\delta_{in}\delta(\mathbf{x}-\mathbf{y})\delta(t)$ for which the corresponding solution is $v_i(\mathbf{x},t)$ given by $G_{in}(\mathbf{x};t;\mathbf{y},0)$

It is assumed that both u and G satisfy homogeneous boundary

conditions on S . A general position within V is denoted by $\boldsymbol{\eta}$ and that on Σ , by \boldsymbol{y} . The normal to Σ is denoted by \boldsymbol{v} . The displacements \boldsymbol{u} on two sides of Σ may be different and so the displacement discontinuity is denoted by $[u(\boldsymbol{y}, \tau)]$ for \boldsymbol{y} on Σ , i.e., $[u(\boldsymbol{y}, \tau)] = u(\boldsymbol{y}, \tau)|_{\Sigma^+} - u(\boldsymbol{y}, \tau)|_{\Sigma^-}$. For spontaneous rupture, tractions must be continuous and so $[\mathbf{T}(\boldsymbol{u}, \boldsymbol{v})] = 0$. With these assumptions equation (2.12) can be simplified to give $u_n(\boldsymbol{x}, t)$, the displacement at a point \boldsymbol{x} and time t .

The final expression is

$$\begin{aligned}
 u_n(\boldsymbol{x}, t) = & \int_{-\infty}^{\infty} d\tau \int_V f_p(\boldsymbol{\eta}, \tau) G_{nk}(\boldsymbol{x}, t-\tau; \boldsymbol{\eta}, 0) dV(\boldsymbol{\eta}) \\
 & + \int_{-\infty}^{\infty} d\tau \int_{\Sigma} \{ [u_i(\boldsymbol{y}, \tau)] c_{ijkl} v_j (\partial G_{nk} / \partial y_l) (\boldsymbol{x}, t-\tau; \boldsymbol{y}, 0) \} d\Sigma
 \end{aligned}
 \dots (2.19)$$

The discontinuities on Σ are localized within V by using the delta function $\delta(\boldsymbol{\eta}-\boldsymbol{y})$. It is possible to write

$$(\partial / \partial y_l) G_{nk}(\boldsymbol{x}, t-\tau; \boldsymbol{y}, 0) = \int_V (\partial / \partial \eta_l) \delta(\boldsymbol{x}-\boldsymbol{y}) G_{nk}(\boldsymbol{x}, t-\tau; \boldsymbol{\eta}, 0) dV(\boldsymbol{\eta})
 \dots (2.20)$$

so that the displacement discontinuity in equation (2.19) contributes the displacement

$$\int_{-\infty}^{\infty} dt \int_V \int_{\Sigma} \{ \int_{\Sigma} [u_i(\boldsymbol{y}, \tau)] c_{ijkl} v_j (\partial / \partial \eta_l) \delta(\boldsymbol{x}-\boldsymbol{y}) d\Sigma \} G_{nk}(\boldsymbol{x}, t-\tau; \boldsymbol{\eta}, 0) dV(\boldsymbol{\eta})
 \dots (2.21)$$

at position \boldsymbol{x} and time t . The body force equivalent $\boldsymbol{f}_p^{[u]}$ of a

displacement discontinuity on Σ can now be written as

$$f_p^{[u]}(\eta, \tau) = - \iint_{\Sigma} [u_i(\mathbf{y}, \tau)] c_{ijkl} v_j (\partial/\partial \eta_l) \delta(\mathbf{x}-\mathbf{y}) d\Sigma \quad \dots (2.22)$$

The body force equivalent in equation (2.22) are applicable to a general inhomogeneous anisotropic medium and they depend on properties of the medium only at the fault surface itself. These body force equivalents due to a displacement discontinuity can be shown to be equivalent to a double couple without moment. Thus a correspondence has been established between slip on a fault and a double couple distribution. The strength of a double couple source is given by moment of each of the couples constituting it and is known as seismic moment. This is given by the product of rigidity of the material around the fault, average slip on the fault and fault area.

In the absence of body forces the displacement field is give by

$$u_n(\mathbf{x}, t) = \int_{-\infty}^{\infty} d\tau \iint_{\Sigma} \{ [u_i(\mathbf{y}, \tau)] c_{ijkl} v_j (\partial G_{nk}/\partial y_l)(\mathbf{x}, t-\tau; \mathbf{y}, 0) \} d\Sigma \quad \dots (2.23)$$

The equation (2.23) gives displacement field due to displacement discontinuities distributed over a fault plane Σ of finite extent. At distances large compared with dimensions of the fault the contributions from different surface elements $d\Sigma$ are all approximately in phase, and the whole surface Σ can be considered as a double couple located at a point on the fault.

Thus for an effective point source

$$u_n(\mathbf{x}, t) = M_{kl} * G_{nk,1} \quad \dots (2.24)$$

where M_{kl} , the moment tensor, is given by

$$M_{kl} = \iint_{\Sigma} [u_i] v_j c_{ijkl} d\Sigma \quad \dots (2.25)$$

For isotropic body

$$[u_i] v_j c_{ijkl} = \lambda v_k [u_p(\mathbf{y}, \tau)] \delta_{kl} + \mu (v_k [u_k(\mathbf{y}, \tau)] + v_l [u_l(\mathbf{y}, \tau)]) \quad \dots (2.26)$$

If the displacement discontinuity is parallel to Σ at \mathbf{y}

$$[u_i] c_{ijkl} v_j = \mu (v_k [u_l] + v_l [u_k]) \quad \dots (2.27)$$

The expression on the R.H.S. of (2.27) is known as the moment density tensor, m_{kl} . The seismic moment M_{kl} , is given by

$$M_{kl} = \iint_{\Sigma} m_{kl} d\Sigma \quad \dots (2.28)$$

To obtain the displacement field radiated by double couple source, an expression is first found for the displacement field of a concentrated unidirectional force.

2.8 RADIATION FROM A CONCENTRATED FORCE

The scalar wave field $\phi = \phi(\mathbf{x}, t)$ with zero initial conditions {i.e., $\phi(\mathbf{n}, 0) = 0, \dot{\phi}(\mathbf{n}, 0) = 0$ for \mathbf{x} not equal to zero} satisfies the following inhomogeneous scalar wave equation

$$\partial^2 \phi / \partial t^2 = \delta(\mathbf{n}) \delta(t) + c^2 \nabla^2 \phi \quad \dots (2.29)$$

This wavefield is due to a unit source localized at the origin and acts at $t=0$. The solution of equation (2.29) is found to be

$$\phi(\mathbf{x}, t) = 1/4\pi c^2 \delta(t - |\mathbf{x}|/c) / |\mathbf{x}| \quad \dots (2.30)$$

This solution is seen to be a product of rapidly varying delta function and the relatively slowly varying reciprocal distance function. The radiation of waves represented by $\phi(\mathbf{x}, t)$ is isotropic because of spherical symmetry. The rapidly function depends only on time relative to an arrival time $|\mathbf{x}|/c$ at which the motion begins. The wave shape is the same in time as that of the inhomogeneous term in equation (2.29)

If the inhomogeneous term in equation (2.29) is of the type $\delta(\mathbf{x}-\mathbf{y}) \delta(t-\tau)$ the solution is

$$\phi(\mathbf{x}, t) = 1/4\pi c^2 \delta(t-\tau - |\mathbf{x}-\mathbf{y}|/c) / |\mathbf{x}-\mathbf{y}| \quad \dots (2.31)$$

If the inhomogeneous term in equation (2.29) is of the form $\delta(\mathbf{x}-\mathbf{y})f(t)$ the solution is found to be

$$\begin{aligned}\phi(\mathbf{x}, t) &= 1/4\pi c^2 \int_{-\infty}^{\infty} \{f(\tau) \delta(t-\tau-|\mathbf{x}-\mathbf{y}|/c) / |\mathbf{x}-\mathbf{y}|\} d\tau \\ &= 1/4\pi c^2 \{f(t-|\mathbf{x}-\mathbf{y}|/c) / |\mathbf{x}-\mathbf{y}|\} \quad \dots (2.32)\end{aligned}$$

If the source is extended throughout a volume V as well as in time, given by

$$\Phi(\mathbf{x}, t) = \int_{-\infty}^{\infty} d\tau \iiint_V \{\Phi(\mathbf{y}, \tau) \delta(\mathbf{x}-\mathbf{y}) \delta(t-\tau)\} dV(\mathbf{y}) \quad \dots (2.33)$$

the solution $\phi(\mathbf{x}, t)$ is then found as

$$\begin{aligned}\phi(\mathbf{x}, t) &= 1/4\pi\alpha^2\rho \int_{-\infty}^{\infty} d\tau \iiint_V \{\Phi(\mathbf{y}, \tau) \delta(t-\tau-|\mathbf{x}-\mathbf{y}|/\alpha) / |\mathbf{x}-\mathbf{y}|\} dV(\mathbf{y}) \\ &= 1/4\pi\alpha^2\rho \iiint_V \{\Phi(\mathbf{y}, t-|\mathbf{x}-\mathbf{y}|/\alpha) / |\mathbf{x}-\mathbf{y}|\} dV(\mathbf{y}) \quad \dots (2.34)\end{aligned}$$

where now $\phi(\mathbf{n}, t)$ satisfies

$$\partial^2\phi/\partial t^2 = \Phi(\mathbf{x}, t)/\rho + \alpha^2\nabla^2\phi \quad \dots (2.35)$$

where α is P-wave velocity

Substitution from equation (2.10) in equation (2.4) yields the following equation (in vector notation)

$$\rho \partial^2\mathbf{u}/\partial t^2 = \mathbf{f} + (\lambda+2\mu)\nabla(\nabla \cdot \mathbf{u}) - \mu(\nabla \times \nabla \times \mathbf{u}) \quad \dots (2.36)$$

There exists potentials ϕ and $\bar{\Psi}$ such that

$$\mathbf{u} = \nabla \phi + \nabla \times \bar{\Psi} \quad \dots (2.37)$$

$$\nabla \cdot \bar{\Psi} = 0 \quad \dots (2.38)$$

$$\partial^2 \phi / \partial t^2 = \Phi / \rho + \alpha^2 \nabla^2 \phi \quad \dots (2.39)$$

$$\partial^2 \bar{\Psi} / \partial t^2 = \bar{\Psi} / \rho + \beta^2 \nabla^2 \bar{\Psi} \quad \dots (2.40)$$

where Φ and $\bar{\Psi}$ the body force potentials are defined by

$$\mathbf{f} = \nabla \Phi + \nabla \times \bar{\Psi} \quad \dots (2.41)$$

$$\text{and } \alpha^2 = (\lambda + 2\mu) / \rho \quad \text{and } \beta^2 = \mu / \rho \quad \dots (2.42)$$

Equation (2.39) is same as equation (2.35)

Let the body force \mathbf{f} in equation (2.36) be represented as

$$\mathbf{f}(\mathbf{x}, t) = F_0(t) \delta(\mathbf{x}) \mathbf{i} \quad \dots (2.43)$$

which represents as concentrated force $F_0(t)$ applied at the origin in x direction. The body force potentials are given by

$$\phi(\mathbf{x}, t) = -[F_0(t) / 4\pi] (\partial / \partial x_1) (1 / |\mathbf{x}|) \quad \dots (2.44)$$

$$\bar{\Psi}(\mathbf{x}, t) = [F_0(t) / 4\pi] [0, (\partial / \partial x_3) (1 / |\mathbf{x}|), -(\partial / \partial x_2) (1 / |\mathbf{x}|)] \quad \dots (2.45)$$

The solution of equations (2.39) and (2.40) with ϕ and $\bar{\Psi}$ defined by equation (2.44) and (2.45) are given by

$$\phi(\mathbf{x}, t) = -1/4\pi\rho [(\partial / \partial x_1) (1 / |\mathbf{x}|)] \int_0^{\infty/\alpha} \tau F_0(t - \tau) d\tau \quad \dots (2.46)$$

$$\bar{\Psi}(\mathbf{x}, t) = 1/4\pi\rho [0, (\partial / \partial x_3) (1 / |\mathbf{x}|), -(\partial / \partial x_2) (1 / |\mathbf{x}|)] \int_0^{\infty/\beta} \tau F_0(t - \tau) d\tau \quad \dots (2.47)$$

Substituting from equations (2.46) and (2.47) in (2.37) gives the Green's function for displacement due to body force $F_0(t)$ applied in the x_1 direction at the origin. Using $r = |\mathbf{x}|$ it gives

$$\begin{aligned}
u_i(\mathbf{x}, t) = & 1/4\pi\rho [(\partial^2/\partial x_i \partial x_i) (1/r)] \int_{r/\alpha}^{r/\beta} \tau F_0(t-\tau) d\tau \\
& + 1/4\pi\rho\alpha^2 r [(\partial r/\partial x_i) (\partial r/\partial x_i)] F_0(t-r/\alpha) \\
& + 1/4\pi\rho\beta^2 r [\partial_{i1} - (\partial r/\partial x_i) (\partial r/\partial x_j)] F_0(t-r/\beta) \dots (2.48)
\end{aligned}$$

On changing 1 to j throughout the equation (2.48) the R.H.S. will yield displacement setup by a concentrated force in the x_j direction. Using direction cosines γ_i for the vector \mathbf{x} so that $\gamma_i = x_i/r = \partial r/\partial x_i$ and writing

$$(\partial^2/\partial x_i \partial x_j) (1/r) = (3\gamma_i \gamma_j - \delta_{ij})/r^3 \dots (2.49)$$

the i^{th} displacement of displacement field at the observation point can be written in the form

$$\begin{aligned}
u_i(\mathbf{x}, t) = & 1/4\pi\rho [(3\gamma_i \gamma_j - \delta_{ij})/r^3] \int_{r/\alpha}^{r/\beta} \tau F_0(t-\tau) d\tau \\
& + 1/4\pi\rho\alpha^2 [\gamma_i \gamma_j (1/r)] F_0(t-r/\alpha) \\
& - 1/4\pi\rho\beta^2 [(\gamma_i \gamma_j - \delta_{ij}) (1/r)] F_0(t-r/\beta) \dots (2.50)
\end{aligned}$$

The terms including r^{-1} in the equation (2.50) are called far field terms and the term containing r^{-3} is called near field term. Whereas there are separate far field terms for P and S waves, the near field term has contributions both from P and S waves. The relation (2.50) can also be expressed as

$$u_i(\mathbf{x}, t) = F_0 * G_{ij} \dots (2.51)$$

where G_{ij} represents the Green's function for a concentrated force. For seismological purposes the appropriate form of Green's function is $G_{nk,1}$ which associated with a double-force system, forming a dipole or a couple. Whereas G_{ij} is described as second order tensor, $G_{nk,1}$ is a third order tensor.

2.9 RADIATION FROM A POINT DOUBLE COUPLE SOURCE

Using the equation (2.50) the n^{th} component of displacement due to a body force distribution $\mathbf{f}(\mathbf{x}, t) = \mathbf{F}(t) \delta(\mathbf{x}-\mathbf{y})$, i.e., the force $\mathbf{F}(t)$ applied at \mathbf{y} can be written as

$$\begin{aligned}
 u_n(\mathbf{x}, t) = F_0 * G_{nk} = & (1/4\pi\rho) [(3\gamma_n\gamma_k - \delta_{nk})/r^3] \int_{r/\alpha}^{r/\beta} \tau F_k(t-\tau) d\tau \\
 & + (1/4\pi\rho\alpha^2) [\gamma_n\gamma_k (1/r)] F_k(t-r/\alpha) \\
 & - (1/4\pi\rho\beta^2) [(\gamma_n\gamma_k - \delta_{nk}) (1/r)] F_k(t-r/\beta) \quad \dots (2.52)
 \end{aligned}$$

in which $r = |\mathbf{x} - \mathbf{y}|$ is the source receiver distance and direction cosines $\gamma_n = (x_n - y_n)/r$ are referred to source at \mathbf{y} .

In order to obtain the displacement field for a point double couple two forces are considered, each of magnitude $\mathbf{F}(t)$, one acting the $+x_k$ at \mathbf{y} and the other acting in the $-x_k$ direction at $\mathbf{y} + \Delta\mathbf{l}_1$ (where $\Delta\mathbf{l}_1$ is a small distance in the y_1 direction). The displacement fields due to these forces are evaluated using equation (2.52) and added algebraically. The

resulting expression is the displacement field (at \mathbf{x}) due to a couple with moment $|\Delta l_1| |\mathbf{F}|$. The product $\Delta l_1 F_k(t)$ in which $\Delta l_1 \rightarrow 0$ and $F_k \rightarrow \infty$ such that the product remains finite is termed the moment tensor component $M_{k1}(t)$. This is expressed as

$$M_{k1} * G_{nk,1} = \lim_{\substack{\Delta l_1 \rightarrow 0 \\ F_k \rightarrow \infty}} \Delta l_1 F_k * (\partial / \partial Y_1) G_{nk} \quad \dots (2.53)$$

The final expression for the displacement field due to a point couple is

$$\begin{aligned} M_{k1} * G_{nk,1} = & [(15\gamma_n \gamma_k \gamma_1 - 3\gamma_n \delta_{k1} - 3\gamma_k \delta_{n1} - 3\gamma_1 \delta_{nk}) / 4\pi\rho] (1/r^4) \int_{r/\alpha}^{r/\beta} \tau M_{k1}(t-\tau) d\tau \\ & + [(6\gamma_n \gamma_k \gamma_1 - \gamma_n \delta_{k1} - \gamma_k \delta_{n1} - \gamma_1 \delta_{nk}) / 4\pi\rho\alpha^2] (1/r) M_{k1}(t-r/\alpha) \\ & - [(6\gamma_n \gamma_k \gamma_1 - \gamma_n \delta_{k1} - \gamma_k \delta_{n1} - 2\gamma_1 \delta_{nk}) / 4\pi\rho\beta^2] (1/r^2) M_{k1}(t-r/\beta) \\ & + [(\gamma_n \gamma_k \gamma_1) / 4\pi\rho\alpha^3] (1/r) \dot{M}_{k1}(t-r/\alpha) \\ & - [(\gamma_n \gamma_k - \delta_{nk}) / 4\pi\rho\beta^3] \gamma_1 (1/r) \dot{M}_{k1}(t-r/\beta) \quad \dots (2.54) \end{aligned}$$

For the case of displacement discontinuity $[\mathbf{u}]$ which is parallel to the fault surface

$$M_{k1} = \mu ([u_k] v_1 + [u_1] v_k) A \quad \dots (2.55)$$

for a fault with area A , normal in the direction v_i and $[\mathbf{u}]$ is evaluated at a general point on the fault \mathbf{y} . Let the average value of displacement discontinuity over the fault be expressed as \mathbf{u} . The expression for displacement is then

$$\mu (\mathbf{u}_k v_1 + \mathbf{u}_1 v_k) A * G_{nk,1}$$

$$\begin{aligned}
&= M_o [(30 \gamma_n \gamma_k \gamma_1 v_1 - 6 v_n \gamma_k - 6 \delta_{nk} v_1 \gamma_1) / 4 \pi \rho] (1/r^3) \int_{r/\alpha}^{r/\beta} \tau f(t-\tau) d\tau \\
&+ M_o [(12 \gamma_n \gamma_k \gamma_1 v_1 - 2 \gamma_k v_n - 2 \delta_{nk} \gamma_1 v_1) / 4 \pi \rho \alpha^2] (1/r^2) f(t-r/\alpha) \\
&- M_o [(12 \gamma_n \gamma_k \gamma_1 v_1 - 3 \gamma_k v_1 - 3 \delta_{nk} \gamma_1 v_1) / 4 \pi \rho \beta^2] (1/r^2) f(t-r/\beta) \\
&+ M_o [(2 \gamma_n \gamma_k \gamma_1 v_1) / 4 \pi \rho \alpha^3] (1/r) \dot{f}(t-r/\alpha) \\
&- M_o [(2 \gamma_n \gamma_k \gamma_1 v_1 - v_n \gamma_k - \delta_{nk} \gamma_1 v_1) / 4 \pi \rho \beta^3] (1/r) \dot{f}(t-r/\beta) \dots (2.56)
\end{aligned}$$

In the above expression $M_o (= \mu u A)$ is the moment of the couple expressed in terms of average slip and fault area. The function $f(t)$ represents time dependence of the slip in the direction \mathbf{x} at a point on the fault. This expression represents displacement field due to a point double couple source which is the body source equivalent of a point shear dislocation. In equation (2.56) the terms in brackets involving direction cosines of $\mathbf{x}-\mathbf{y}$, fault normal \mathbf{v} and direction of slip vector express the radiation pattern of the displacement field radiated by a point source.

2.10 FAR FIELD RADIATION FROM A POINT DOUBLE COUPLE SOURCE

For the purpose of generation of synthetic accelerograms in the near field of a large earthquake, the dimensions of the source cannot be ignored. The fault area is divided into a number of sub-faults or elementary faults which can be approximated as point sources with areas which are small compared with their

distance to the observation point. In such a case only the far field terms in the expression (2.56) need be used for computing the ground motion. Hence the expression for computing the displacement field at a point can be written as

$$u_n(\mathbf{x}, t) = M_0/4\pi\rho\alpha^3 (2\gamma_n\gamma_k\gamma_l v_l/r) \dot{f}(t-r/\alpha) \\ - M_0/4\pi\rho\beta^3 (2\gamma_n\gamma_k\gamma_l v_l - \gamma_n v_k - \delta_{nk}\gamma_l v_l)/r \dot{f}(t-r/\beta) \dots (2.57)$$

where M_0 represents the seismic moment for slip on an elementary fault. The displacement in the far field is clearly proportional to the time derivative of the source time function.

The far field for a point source is simply "all positions that are more than a few wavelengths away from the source". For a finite source with a characteristic dimension L (say, length of fault), the far field is "all positions that are few fault lengths away". For an elementary fault with length 1km, a point 10km away can be considered to be in the far field.

2.11 RADIATION PATTERN IN TERMS OF FAULT PARAMETERS

The radiation pattern terms in equation (2.57) should be expressed in terms of parameters of the fault having arbitrary orientation. These parameters are the dip and the strike of the fault. The direction of slip is expressed in the form of slip

angle or rake. The fault has two surfaces, called hanging wall and foot wall. Slip \mathbf{u} the direction in which hanging wall moves relative to foot wall. Rake λ is the angle between strike direction and slip. This is illustrated in Fig 2.2, in which X_1 -axis is taken positive towards north, X_2 -axis positive towards east and X_3 -axis positive downwards. The origin of the cartesian coordinate system is taken to coincide with the epicentre E of the earthquake with focus F lying on the fault. The strike of the fault is denoted by ϕ_s and dip by δ . Rake λ is measured on the fault plane in the counterclockwise direction.

For a strike slip fault, $\delta = \pi/2$ and $\lambda = 0$ or π corresponding to left lateral or right lateral strike slip fault respectively. For a dip-slip fault $\delta = \pi/2$ and $\lambda = \pi/2$ or $3\pi/2$. If δ is less than $\pi/4$ and λ is within the range $(0, \pi)$ the fault is termed thrust fault. For $\delta > \pi/4$, it is termed reverse fault if $0 < \lambda < \pi$ and normal fault if $\pi < \lambda < 2\pi$.

The radiation pattern is a function of $\phi_s, \delta, \lambda, i_o, \phi$ and is obtained separately for P-, SV- and SH waves are given below

$$\mathbf{u}^P(\mathbf{x}, t) = (M_o R^P / 4\pi\rho\alpha^3 r) \dot{f}(t-r/\alpha) \mathbf{e}_p \quad \dots (2.58)$$

$$\mathbf{u}^{SV}(\mathbf{x}, t) = (M_o R^{SV} / 4\pi\rho\beta^3 r) \dot{f}(t-r/\beta) \mathbf{e}_s \quad \dots (2.59)$$

$$\mathbf{u}^{SH}(\mathbf{x}, t) = (M_o R^{SH} / 4\pi\rho\beta^3 r) \dot{f}(t-r/\beta) \mathbf{e}_t \quad \dots (2.60)$$

where $\mathbf{e}_p, \mathbf{e}_s, \mathbf{e}_t$ are unit vectors in the direction of particle

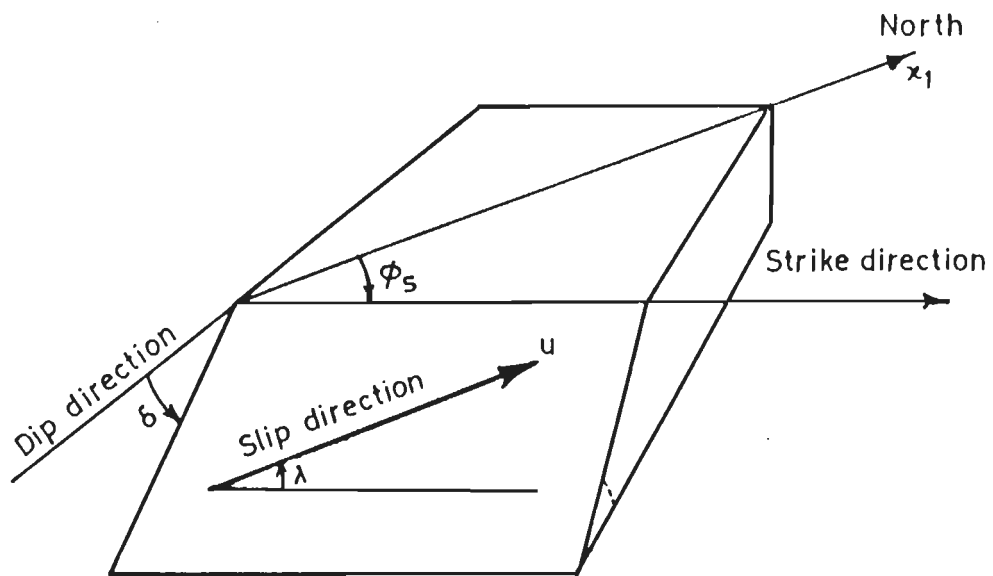


Fig 2.2 Definition of the fault orientation parameters (strike ϕ_s , dip δ), and slip direction.

motion in the P-, SV- and SH wave respectively. Let \mathbf{s} be the unit vector in the direction of the slip vector. The expressions for $\mathbf{s}, \mathbf{v}, \mathbf{e}_p, \mathbf{e}_s, \mathbf{e}_t, R^P, R^{SV}$ and R^{SH} are given below in terms of various angles and unit vectors $\mathbf{e}_x, \mathbf{e}_y$ and \mathbf{e}_z in x_1, x_2 and x_3 directions respectively.

$$\mathbf{s} = (\cos\lambda \cos\phi_s + \cos\delta \sin\lambda \sin\phi_s)\mathbf{e}_x + (\cos\lambda \sin\phi_s - \cos\delta \sin\lambda \cos\phi_s)\mathbf{e}_y - (\sin\delta \sin\lambda)\mathbf{e}_z \quad \dots (2.61)$$

$$\mathbf{v} = (-\sin\delta \sin\phi_s)\mathbf{e}_x + (\sin\delta \cos\phi_s)\mathbf{e}_y - (\cos\delta)\mathbf{e}_z \quad \dots (2.62)$$

$$\mathbf{e}_p = (\sin i_o \cos\phi)\mathbf{e}_x + (\sin i_o \sin\phi)\mathbf{e}_y + (\cos i_o)\mathbf{e}_z \quad \dots (2.63)$$

$$\mathbf{e}_s = (\cos i_o \cos\phi)\mathbf{e}_x + (\cos i_o \sin\phi)\mathbf{e}_y - (\sin i_o)\mathbf{e}_z \quad \dots (2.64)$$

$$\mathbf{e}_t = (-\sin\phi)\mathbf{e}_x + (\cos\phi)\mathbf{e}_y \quad \dots (2.65)$$

$$\begin{aligned} R^P = & \cos\lambda \sin\delta \sin^2 i_o \sin 2(\phi - \phi_s) \\ & + \sin\lambda \cos 2\delta \sin 2i_o \sin(\phi - \phi_s) \\ & + \sin\lambda \sin 2\delta [\cos^2 i_o - \sin^2 i_o \sin^2(\phi - \phi_s)] \\ & - \cos\lambda \cos\delta \sin 2i_o \cos(\phi - \phi_s) \quad \dots (2.66) \end{aligned}$$

$$\begin{aligned} R^{SV} = & +\frac{1}{2} (\cos\lambda \sin\delta \sin 2i_o) \sin 2(\phi - \phi_s) \\ & + \sin\lambda \cos 2\delta \cos 2i_o \sin(\phi - \phi_s) \\ & - \frac{1}{2} \sin\lambda \sin 2\delta \sin 2i_o (1 + \sin^2(\phi - \phi_s)) \\ & - \cos\lambda \cos\delta \cos 2i_o \cos(\phi - \phi_s) \quad \dots (2.67) \end{aligned}$$

$$\begin{aligned}
R^{sh} = & \cos\lambda \sin\delta \sin i_0 \cos 2(\phi - \phi_s) \\
& + \sin\lambda \cos 2\delta \cos i_0 \cos 2(\phi - \phi_s) \\
& - \frac{1}{2} \sin\lambda \sin 2\delta \sin i_0 \sin 2(\phi - \phi_s) \\
& + \cos\lambda \cos\delta \cos i_0 \sin(\phi - \phi_s) \quad \dots (2.68)
\end{aligned}$$

The expressions for R^p, R^{sv} and R^{sh} can also be expressed in matrix form as follows

$$\begin{bmatrix} R^p \\ R^{sv} \\ R^{sh} \end{bmatrix} = \begin{bmatrix} P_1 & P_2 & P_3 & P_4 \\ S_1 & S_2 & S_3 & S_4 \\ T_1 & T_2 & T_3 & T_4 \end{bmatrix} \begin{bmatrix} \cos\lambda \sin\delta \\ \sin\lambda \cos 2\delta \\ \sin\lambda \sin 2\delta \\ \cos\lambda \cos\delta \end{bmatrix} \dots (2.69)$$

where P_1, P_2 , etc. are coefficients of corresponding terms in the column vector on the R.H.S. and can be obtained from equations (2.66) to (2.68), e.g., $P_1 = \sin^2 i_0 \sin 2(\phi - \phi_s)$, $S_2 = \cos 2i_0 \sin(\phi - \phi_s)$, $T_3 = -(1/2) \sin i_0 \sin 2(\phi - \phi_s)$, etc.

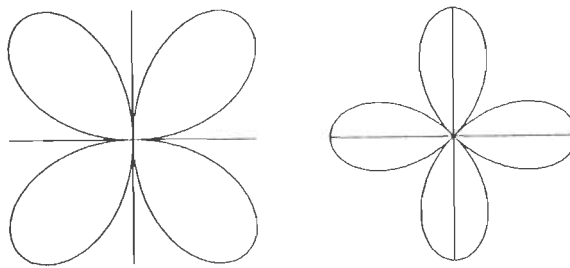
The radiation pattern terms are thus seen to be made up of contributions from four elementary faults. If $\lambda=0, \delta=\pi/2$ (vertical strike slip fault), only the first column of the matrix in (2.69) contributes to the radiation pattern, since all but the first element of the column vector on R.H.S. of the (2.69) are zero. Four cases arise : (a) for $\lambda=0, \delta=\pi/2$ (vertical strike slip fault) only first column contributes; (b) for $\lambda=3\pi/2, \delta=\pi/2$ (vertical

dip slip fault) only the second column contributes; (c) for $\lambda=\pi/2$, $\delta=\pi/4$ (reverse slip on a 45° dipping fault plane) only the fourth column contributes; and (d) for $\lambda=0$, $\delta=0$ (slip on a horizontal plane) only the fourth column contributes. For arbitrary λ and δ , all the 12 elements of the matrix contribute. When $i=\pi/2$, it corresponds to surface focus. For a point strike slip fault with surface focus, the radiation pattern is given by $\text{Sin}2(\phi-\phi_a)$ which gives the familiar four lobe radiation pattern for P waves. For the four elementary faults the radiation pattern for P-, SV- and SH- are shown in Fig 2.3 for surface focus (i.e., $i_0=0$). Due to this reason there will be no radiation of P and SH for cases (b) and (d) and no radiation of SV for cases (a) and (c).

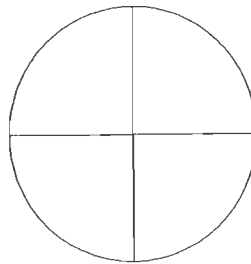
The expressions given by (2.58) to (2.60) are valid in an infinite elastic medium. However strong ground motion records are obtained by accelerographs placed on earth's surface. The free surface of the earth modifies the amplitudes of waves incident from below. This can be understood as follows.

2.12 FREE SURFACE EFFECT

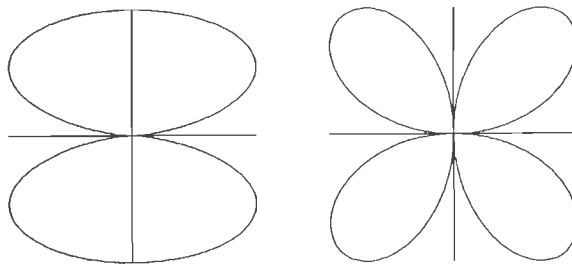
In Fig 2.4 a receiver R is placed below the free surface which receives direct P, reflected PP and reflected PS waves from a buried focus F. The record of ground motion made by this



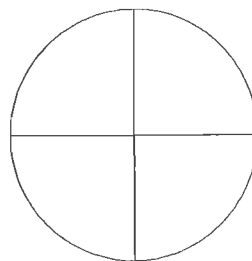
(a) Vertical strike slip fault



(b) Vertical dip slip fault



(c) Reverse slip on a 45° dipping plane



(d) Slip on a horizontal fault

Fig 2.3 Radiation pattern of P, SV and SH wave for four elementary faults for an earthquake with focus on the surface.

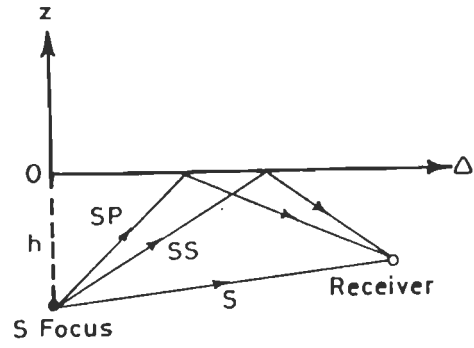
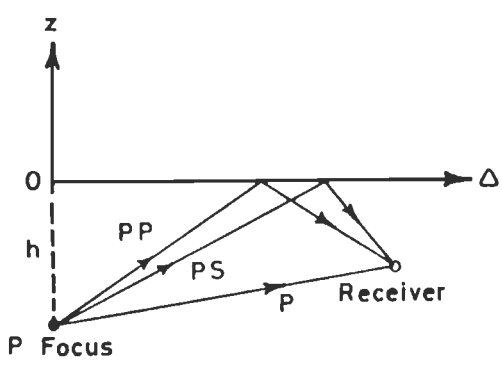


Fig 2.4 Direct and reflected rays emanating from a buried source and received at a buried receiver.

receiver shows three distinct events. When the depth of the receiver below the surface is decreased the three events are observed at shorter time intervals. When the receiver lies at the free surface the three events coalesce giving a single event, which then expresses the effect which the presence of free surface has on the wave incident from below. In a similar way incident SV waves are also affected by the presence of free surface. The amplitude of SH waves is doubled as a consequence of the presence of the free surface.

The formula for computing free surface effect on incident P-waves are given below in terms of horizontal u_H and vertical u_3 components of P-wave displacement

$$u_H^P = A[\sin i + R_{PP}\sin i + R_{PS}\cos j] \quad \dots(2.70)$$

$$u_3^P = A[-\cos i + R_{PP}\cos i - R_{PS}\sin j] \quad \dots(2.71)$$

and those for incident SV waves are

$$u_H^{SV} = B[\cos j + R_{SP}\sin i + R_{SS}\cos j] \quad \dots(2.72)$$

$$u_3^{SV} = B[\sin j + R_{S/P}\cos i - R_{SS}\sin j] \quad \dots(2.73)$$

where A, B are the amplitude of P and SV waves in an infinite medium as given by (2.58) and (2.59) respectively.

In the above formulae the horizontal component of the

displacement is in the plane of incidence containing the receiving station, ray path and the focus. The angle i is the angle of incidence for the P waves and j for the SV waves at the free surface. These angles are related by Snell's law

$$(\sin i)/\alpha = (\sin j) /\beta \quad \dots(2.74)$$

where α and β are P and S wave velocities in the half space.

R_{pp}, R_{ps} are reflection coefficients for incident P waves and R_{ss}, R_{sp} those for incident SV waves when waves are incident on the surface of half space from below. These are given below:

$$R_{pp} = \frac{-(1/\beta^2 - 2p^2)^2 + 4p^2[(\cos i)/\alpha][(\cos j)/\beta]}{+(1/\beta^2 - 2p^2)^2 + 4p^2[(\cos i)/\alpha][(\cos j)/\beta]} \quad \dots(2.75)$$

$$R_{ps} = \frac{4(\alpha/\beta)p(\cos i/\alpha)(1/\beta^2 - 2p^2)}{(1/\beta^2 - 2p^2)^2 + 4p^2(\cos i/\alpha)(\cos j/\beta)} \quad \dots(2.76)$$

$$R_{sp} = \frac{-4(\beta/\alpha)p(\cos j/\beta)(1/\beta^2 - 2p^2)}{(1/\beta^2 - 2p^2)^2 + 4p^2(\cos i/\alpha)(\cos j/\beta)} \quad \dots(2.77)$$

$$R_{ss} = \frac{(1/\beta^2 - 2p^2)^2 - 4p^2(\cos i/\alpha)(\cos j/\beta)}{(1/\beta^2 - 2p^2)^2 + 4p^2(\cos i/\alpha)(\cos j/\beta)} \quad \dots(2.78)$$

The formula (2.72) and (2.73) for incident SV waves are valid only for $j \leq j_c$ where $j_c = \sin^{-1}(\beta/\alpha)$ is the critical angle for

248220



incident SV waves. When $j \geq j_c$, the reflected wave becomes inhomogeneous travelling along the free surface and decaying in the vertical direction. The reflection coefficient R_{SP} becomes complex. The reflected S wave does not decay with depth. However R_{SS} is complex and its magnitude becomes unity for all angles $j \geq j_c$. In formula (2.75) and (2.76), R_{PS} and R_{SS} are evaluated as complex numbers treating $\cos i$ as imaginary quantity given by $i\sqrt{p^2\alpha^2-1}$ where $p = \sin j/\beta$ is the ray parameter. The horizontal and vertical components of SV- displacement at the free surface are also given by (2.77) and (2.78) with the difference that R_{SP} and R_{SS} must now be treated as complex quantities. The variation of u_H and u_3 for P and SV waves with angle of incidence is shown in Fig. 2.5.

For incident SH waves the displacement given by equation (2.81) are simply doubled to take into account the free surface effect. The P,SV and SH wave displacements on free surface are now given by

$$\mathbf{u}^P = u_H^P \cos\phi \mathbf{e}_1 + u_H^P \sin\phi \mathbf{e}_2 + u_3^P \mathbf{e}_3 \quad \dots(2.79)$$

$$\mathbf{u}^{SV} = u_H^{SV} \cos\phi \mathbf{e}_1 + u_H^{SV} \sin\phi \mathbf{e}_2 + u_3^{SV} \mathbf{e}_3 \quad \dots(2.80)$$

$$\mathbf{u}^{SH} = -C \sin \phi + C \cos \phi \quad \dots(2.81)$$

where C is the amplitude of the SH wave in an infinite medium as

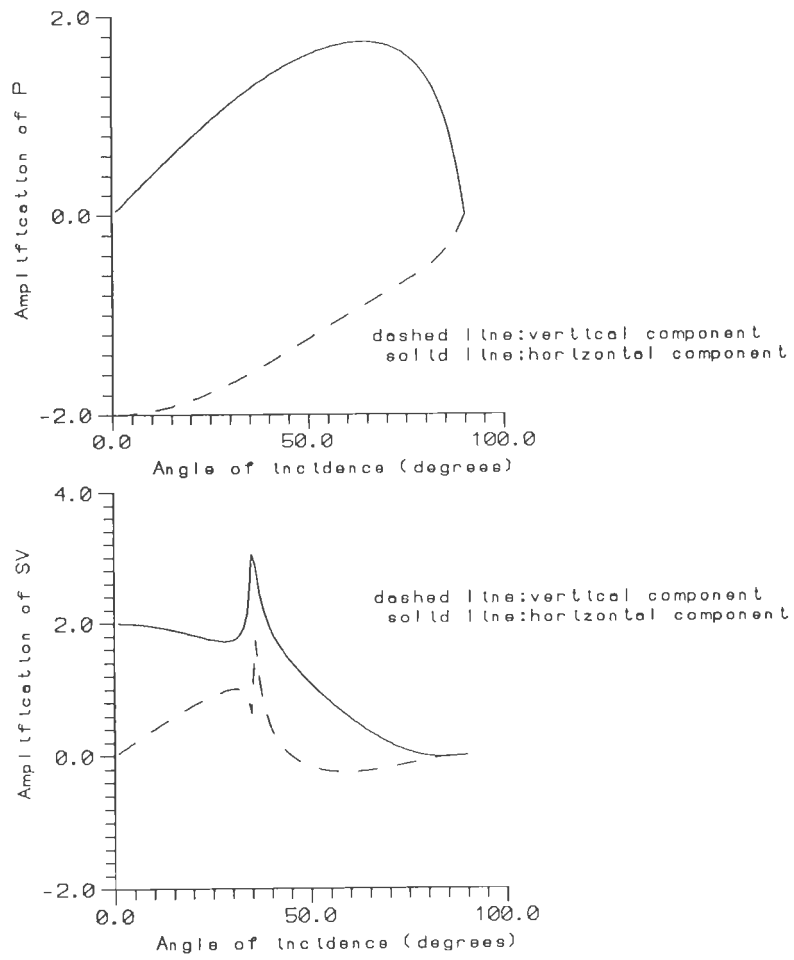


Fig 2.5 Amplification of P and SV wave amplitude at the free surface as a function of angle of incidence.

given by (2.60).

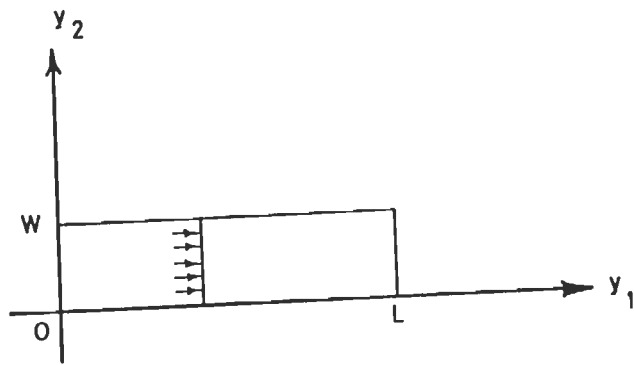
The formula given by equations (2.79) to (2.81) yield P, SV and SH wave displacements on the surface of a half space due to a point shear dislocation with radiation pattern of the source and free surface effect having been taken into account. For a moving source the effect of rupture propagation has to be taken into account. A rectangular fault of length L and width W is considered as shown in Fig 2.6. The rupture initiates along the side AB of the fault and propagates perpendicular to AB at the speed of rupture propagation v_r .

2.13 RADIATION FROM A FINITE MOVING SOURCE

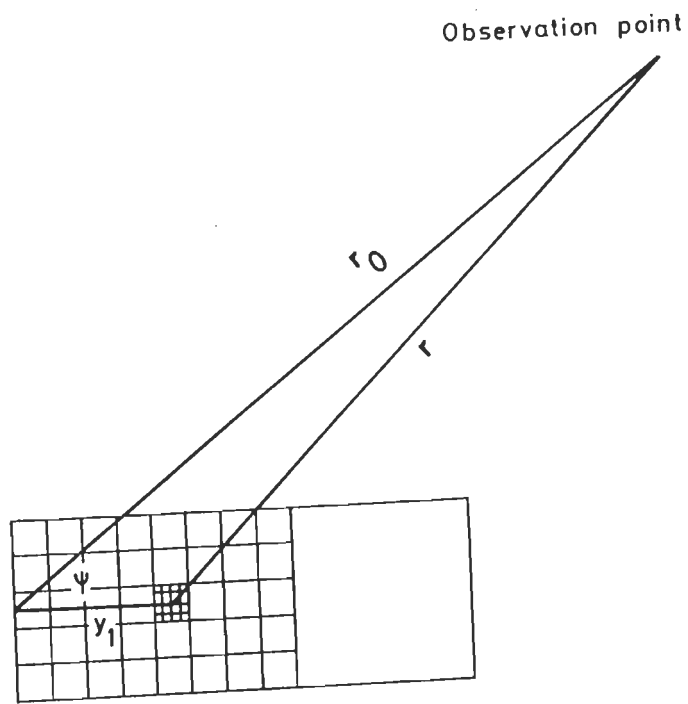
In the far field the displacement field due to radiation from a source distributed over Σ is given by

$$u_n(\mathbf{x}, t) = \iint_{\Sigma} (\mu R^P / 4\pi\rho\alpha^3 r) \dot{[u]}(\mathbf{y}, t-r/\alpha) d\Sigma \\ + \iint_{\Sigma} (\mu R^{SV} / 4\pi\rho\beta^3 r) \dot{[u]}(\mathbf{y}, t-r/\beta) d\Sigma \quad \dots (2.82)$$

If the observation point is far away as compared with the linear dimensions of Σ , it can be assumed that the distance r and the radiation pattern terms R^P and R^{SV} are approximately constant and independent of \mathbf{y} . So these terms can be taken



(a)



(b)

Fig 2.6 Unilateral faulting on a rectangular fault. (a) The fault plane. (b) ψ is the angle between the direction to the receiver and the direction of rupture propagation.

outside the integral. If Σ is plane and direction of displacement of discontinuity is same everywhere on Σ , one can write

$$[\mathbf{u}(\mathbf{y}, t)] = \mathbf{s} \cdot \Delta u(\mathbf{y}, t) \quad \dots (2.83)$$

and

$$\begin{aligned} u(\mathbf{x}, t) = & (\mu R^p / 4\pi\rho\alpha^3 r) \iint_{\Sigma} \dot{\Delta u}(\mathbf{y}, t-r/\alpha) d\Sigma \\ & + (\mu R^{sv} / 4\pi\rho\beta^3 r) \iint_{\Sigma} \dot{\Delta u}(\mathbf{y}, t-r/\beta) d\Sigma \\ & + (\mu R^{sh} / 4\pi\rho\alpha^3 r) \iint_{\Sigma} \dot{\Delta u}(\mathbf{y}, t-r/\beta) d\Sigma \quad \dots (2.84) \end{aligned}$$

The integrals in equation (2.84) can be written in simple form

$$I(\mathbf{x}, t) = \iint_{\Sigma} \dot{\Delta u}(\mathbf{y}, t-r/c) d\Sigma \quad \dots (2.85)$$

where $c(=\alpha, \beta)$ is the velocity of wave propagation.

Taking the origin of coordinates at a reference point on the fault the distance r between surface element $d\Sigma$ and the receiver point x can be written as

$$r \approx r_0 - (\mathbf{y} \cdot \mathbf{e}_r) \quad \dots (2.86)$$

where r_0 is the distance of the receiver from the origin, \mathbf{e}_r unit vector pointing to the receiver and \mathbf{y} is the location vector of $d\Sigma$ measured from the origin. The approximation in expression (2.86) is justified only for

$$y_{\max} \ll \lambda r_o / 2 \quad \dots (2.87)$$

where y_{\max} is the maximum of $|y|$ on Σ and λ is wavelength. Under this condition equation (2.85) can be written as

$$I(\mathbf{x}, t) = \iint_{\Sigma} \Delta u \{ \mathbf{y}, t - [r_o - (\mathbf{y} \cdot \mathbf{e}_r)] / c \} d\Sigma \quad \dots (2.88)$$

A coordinate system (y_1, y_2) parallel to length (i.e., in the strike direction) and width of the fault plane is set up, and the source time function is specified by

$$f(\mathbf{y}, t) = \begin{cases} f(t - y_1 / v_r) & 0 < y_1 < L \\ & 0 < y_2 < W \\ 0 & y_1 < 0, y_2 > 0 \\ & 0 < y_2 < W \\ 0 & y_1 < 0, y_2 > 0 \end{cases} \quad \dots (2.89)$$

On substituting from (2.89) in (2.88) the following relation is obtained

$$I(\mathbf{x}, t) = \int_0^W \int_0^L \dot{f} \{ t - (r_o/c) - (y_1/v_r) + (y_1 \mathbf{e}_1 + y_2 \mathbf{e}_2) / c \} dy_1 dy_2 \quad \dots (2.90)$$

Assuming that W and $y_2 \mathbf{e}_2$ are small the equation (2.90) can be rewritten as

$$I(\mathbf{x}, t) = W \int_0^L \dot{f} \{ t - (r_o/c) - y_1 [(1/v) - (\cos \psi / c)] + [(y_1 \mathbf{e}_1 + y_2 \mathbf{e}_2) / c] \} dy_1 dy_2 \quad \dots (2.91)$$

On carrying out the integration the following result is obtained

$$I(\mathbf{x}, t) = LW/\tau_c \{f[t - (r_o/c)] - f[t - (r_o/c) - \tau_c]\} \quad \dots (2.92)$$

$$\text{where } \tau_c = (L/c) [(c/v_r) - \cos \psi] \quad (c = \alpha, \beta) \quad \dots (2.93)$$

The final result giving far field displacements due to a finite moving source is given by

$$\begin{aligned} u(\mathbf{x}, t) = & (M_o R^P / 4\pi\rho\alpha^3 r\tau_\alpha) \{f[t - (r_o/\alpha)] - f[t - (r_o/\alpha) - \tau_\alpha]\} \\ & + (M_o R^{SV} / 4\pi\rho\alpha^3 r\tau_\beta) \{f[t - (r_o/\beta)] - f[t - (r_o/\beta) - \tau_\beta]\} \\ & + (M_o R^{SH} / 4\pi\rho\alpha^3 r\tau_\beta) \{f[t - (r_o/\beta)] - f[t - (r_o/\beta) - \tau_\beta]\} \dots (2.94) \end{aligned}$$

The wavefield given by equation (2.94) has to be corrected for free surface effect using relations (2.70- 2.73). The computation of synthetic accelerograms has been carried out using the above relationships.

CHAPTER-3

COMPUTATION OF SYNTHETIC ACCELEROGRAMS FOR UTTARKASHI EARTHQUAKE

3.1 INTRODUCTION

The Uttarkashi earthquake of October 19, 1991 (21:23:14.3 GMT) was recorded at 13 strong motion accelerograph stations in the Garhwal Himalaya. These recording stations are shown in Fig 1.2. Of the 13 stations seven stations were chosen for the purpose of simulation of strong ground motion and are shown in Fig 3.1. Other details of these selected stations are given in Table 3.1. Fig 3.2 shows the accelerograms recorded at the Uttarkashi station.

3.2 SOURCE MODEL

For the purpose of simulation using the formulae given in Chapter 2, a source model has to be specified. This includes spatio-temporal parameters of earthquake focus, fault geometry (dip and strike of the fault), slip distribution over the fault plane and source time function. For the sake of simplicity source is supposed to be buried in a homogeneous half space. This will prove to be amply justified when the fault geometry is specified.

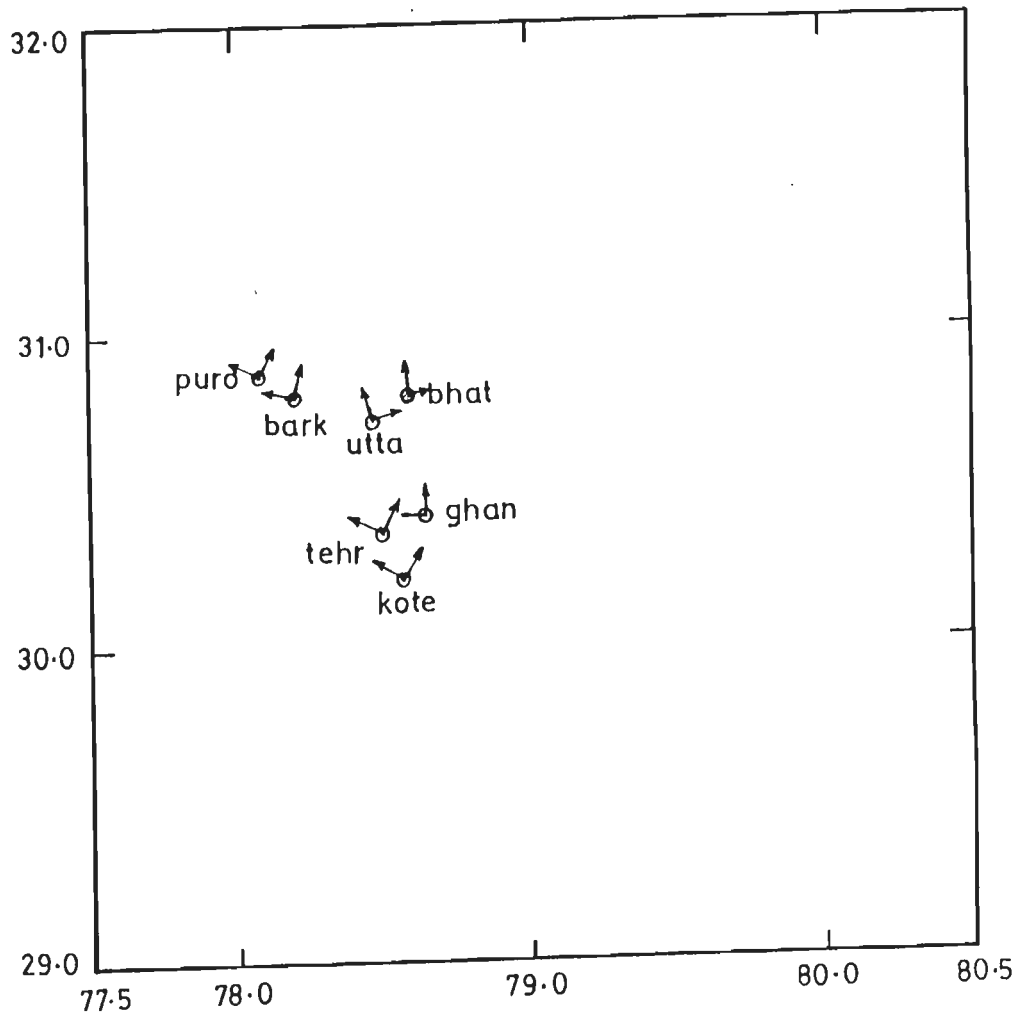


Fig 3.1 Locations of seven selected stations with directions of L and T components. bark: Barkot, bhat: Bhatwari, ghan: Ghansyali, kote: Koteshwar, puro: Purola, tehr: Tehri, utta: Uttarkashi

Table 3.1

DETAILS OF THE SELECTED STATIONS

| S. No. | Station | Station Coordinates | Epicentral distance Δ (km) | Components |
|--------|------------|---------------------|-----------------------------------|------------------|
| 1 | BARKOT | 30.80N 78.22E | 61.7670 | L N10E T N80W |
| 2 | BHATWARI | 30.80N 78.60E | 19.51398 | L N85E T N5W |
| 3 | GHANSYALI | 30.41N 78.65E | 42.54789 | L N00E T N90W |
| 4 | KOTESHWAR | 30.23N 78.57E | 65.07112 | L N30W T N60E |
| 5 | PUROLA | 30.87N 78.04E | 77.96727 | L N65W T N25E |
| 6 | TEHRI | 30.36N 78.50E | 55.02995 | L N63W T N27E |
| 7 | UTTARKASHI | 30.73N 78.45E | 36.52394 | L N15W T N75E |

Δ : Epicentral Distance L : Longitudinal T : Transverse

3.2.1 SPATIO-TEMPORAL PARAMETERS

The following location parameters of the Uttarkashi earthquake have been chosen

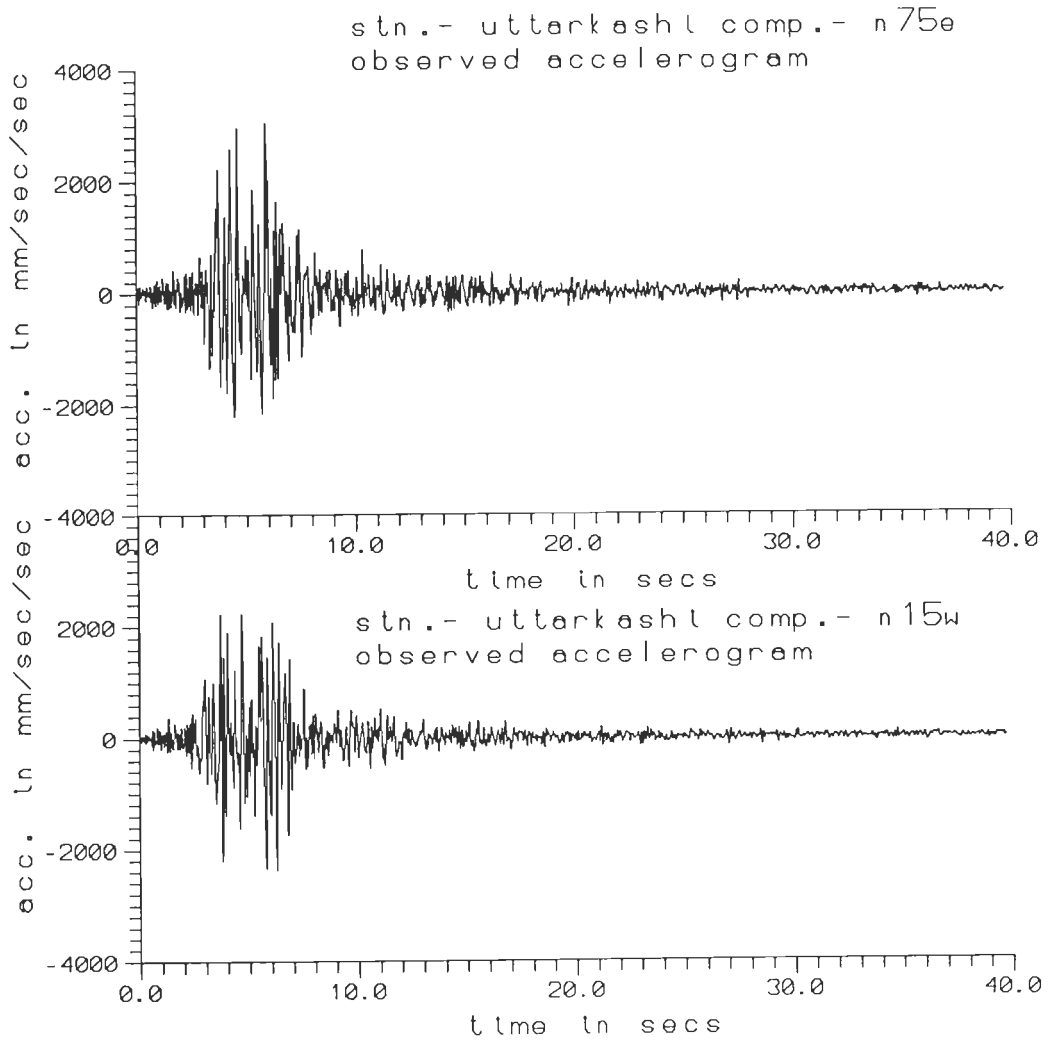


Fig 3.2 Accelerograms of Uttarkashi earthquake recorded at Uttarkashi.

Epicenter: 30.78N , 78.774E

Focal Depth: 10 km

These parameters were reported by USGS (PDE monthly, October 1991)

3.2.2 FOCAL MECHANISM SOLUTION

Table 1.2 gives the focal mechanism solution reported by various agencies. Of these the one based on P wave first motion is stated to be poorly constrained (Khattari et al, 1994). The Centroid Moment Tensor focal mechanism solution by Harvard University (PDE, Monthly, Oct. 1991) has been chosen in this study as the initial model. The source parameters are

$$M_0 = 1.8 \times 10^{26} \text{ dyne cm}$$

$$M_s = 7.0$$

$$m_b = 6.5$$

$$M_w = 6.8$$

NP1 : Strike 317° , dip 14° , slip 115°

NP2 : Strike 112° , dip 78° , slip 84°

The focal mechanism solution is shown in Fig.3.3. The fault plane chosen for modelling strong ground motion is the one having parameters corresponding to NP1 given above. Fig 3.4a shows the fault in vertical section parallel to strike of the

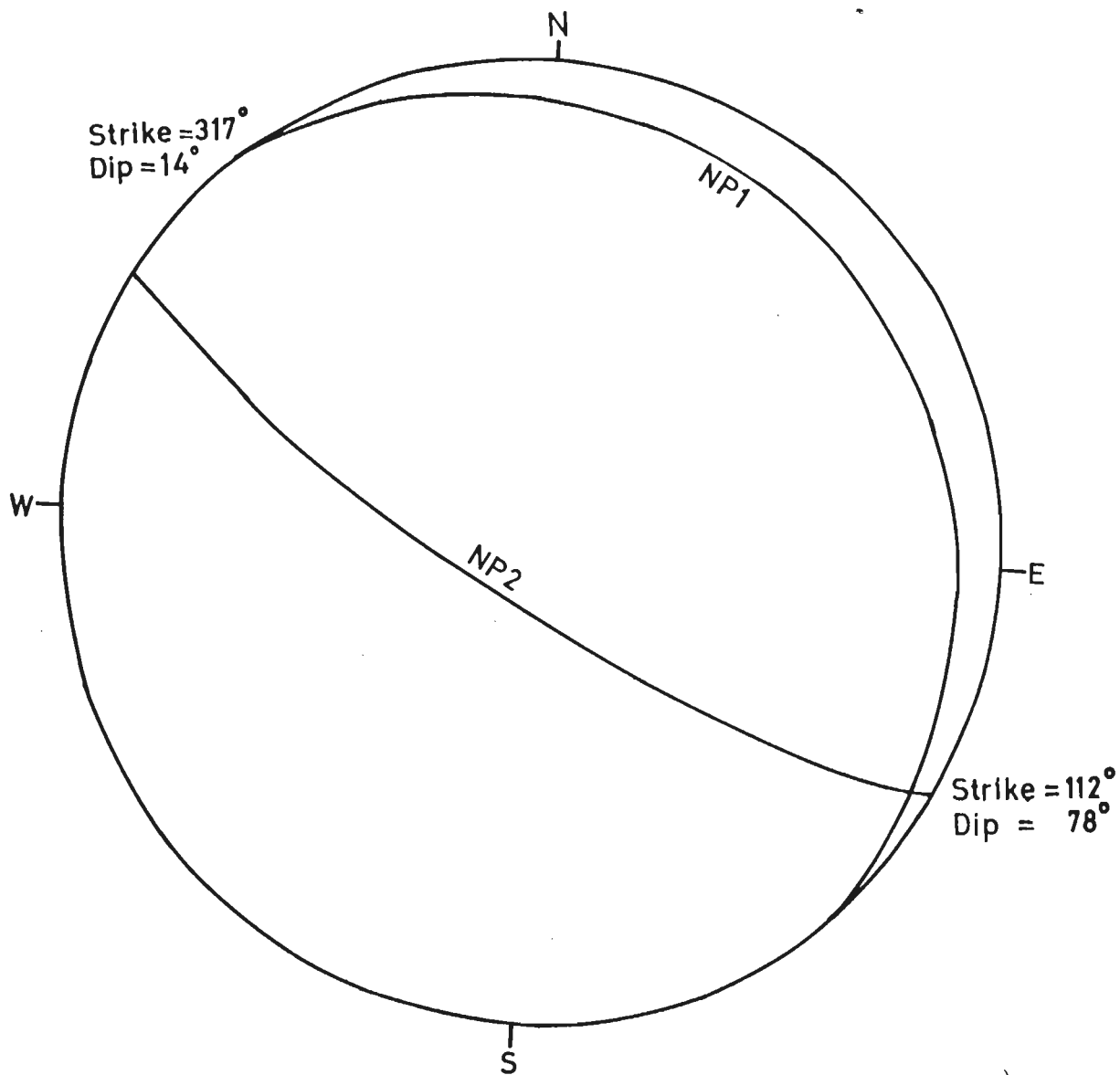


Fig 3.3 Fault plane solution, NP1: Strike 317° dip 14° , NP2: Strike 112° dip 78° , of Uttarkashi earthquake of October 19, 1991, as used in this study

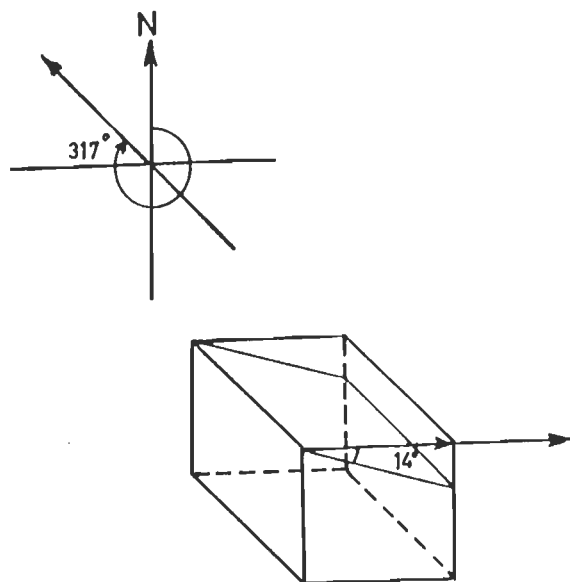
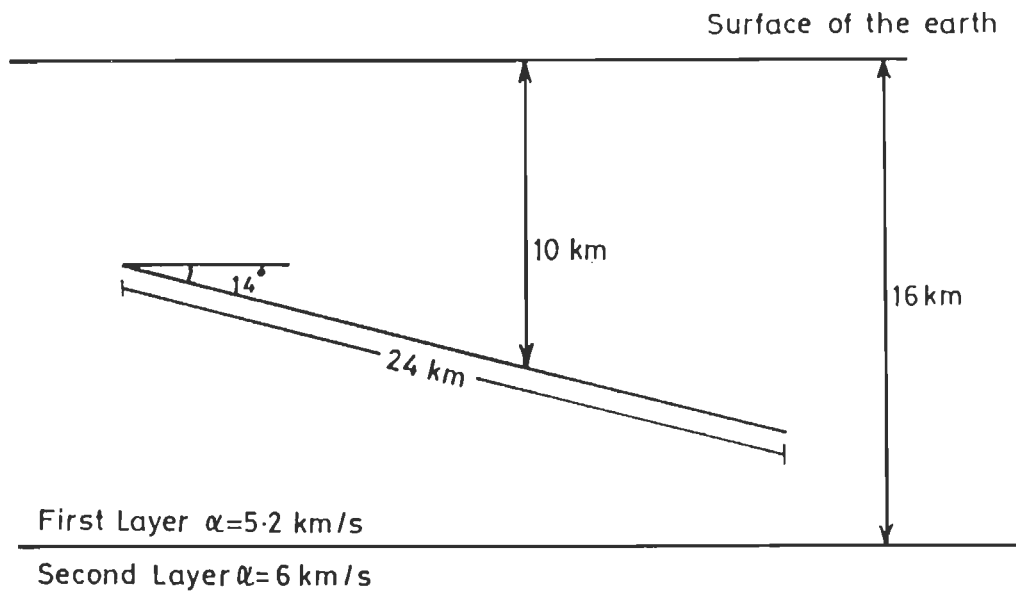


Fig 3.4 (a) Vertical section perpendicular to strike of the fault showing that the fault lies in the first layer.
 (b) Strike of the fault plane and dip in a three dimensional view.

fault along with the two layer P velocity model obtained in local earthquake surveys (Khattri, 1992). According to this model the P velocity in the top layer is 5.2 km/s and that in the second layer, 6.0 km/s . The top layer is 16 km thick. The fault plane lies entirely in the top layer. The first P and S wave arrivals are direct arrivals from all the seven stations chosen for the present work. Fig. 3.4b shows a three dimensional view of the fault plane.

3.2.3 VELOCITY MODEL

The fault plane chosen for modelling strong ground motion is assumed to be buried in a half space with P wave velocity of 5.2 km/s and S wave velocity of 3.0 km/s . The density of half space is chosen to be 2.7 g/cm³. These velocities correspond to a material with Poisson's ratio of 0.25 which signifies that half space is made up of well consolidated rocks.

3.2.4 THE SOURCE TIME FUNCTION

For the purposes of present study a ramp function with rounded shoulders is chosen as the source time function. The formula for the same is as given below (Ben-Menahem and Singh, 1981)

$$f(t) = \begin{cases} 0 & , t \leq 0 \\ (t/T_0) (1 - \sin \omega_0 t / \omega_0 t) & , 0 \leq t \leq T_0 \\ 1 & , t \geq T_0 \end{cases} \dots (3.1)$$

where T_0 is the rise time and $\omega_0=2\pi/T_0$. This function is continuous everywhere and is easily differentiable. The above form is chosen to model slip as a function of time at a point on the fault. The velocity and acceleration pulses emanating from the source are given below

$$v(t) = (1/T_0)(1 - \cos\omega_0 t), \quad 0 \leq t \leq T_0 \quad \dots(3.2)$$

$$a(t) = (\omega_0/T_0) \sin\omega_0 t \quad , \quad 0 \leq t \leq T_0 \quad \dots(3.3)$$

The three waveforms are shown in Fig 3.5 for $T_0= 0.25$ sec and sampling interval of 0.02 sec, the same as for recorded accelerograms . In Fig 3.6 the amplitude spectra of these waveforms are also shown. This type of source time function has been used by Ben-Menahem and Singh (1981) for generating theoretical seismograms.

3.2.5 SOURCE SIZE

For generating synthetic accelerograms in the near field geometry, the size of the source i.e. the fault plane, has to be carefully specified. In the present case the initial data regarding geometry of the causative fault was provided by the CMT Harvard focal mechanism solution as described earlier. For fixing the size of the fault following method was followed.

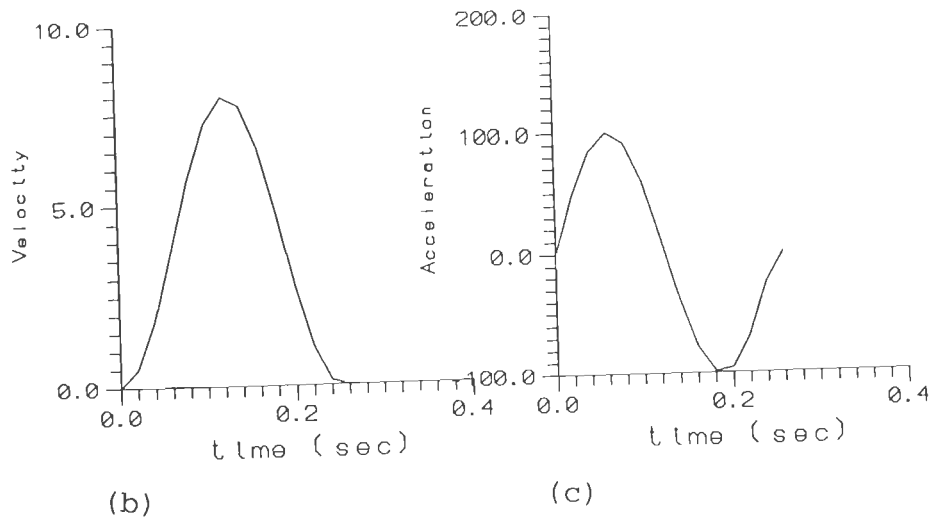
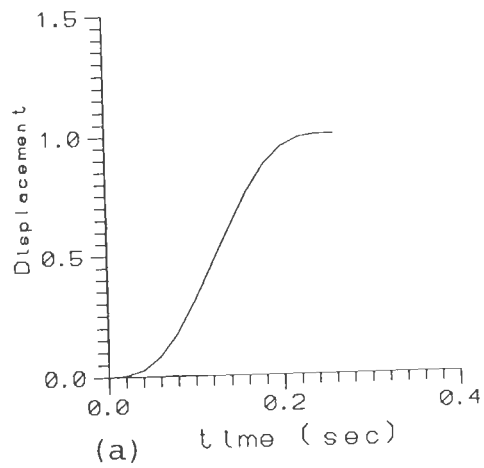


Fig 3.5 Source time function (a) slip displacement (b) slip velocity (c) slip acceleration.

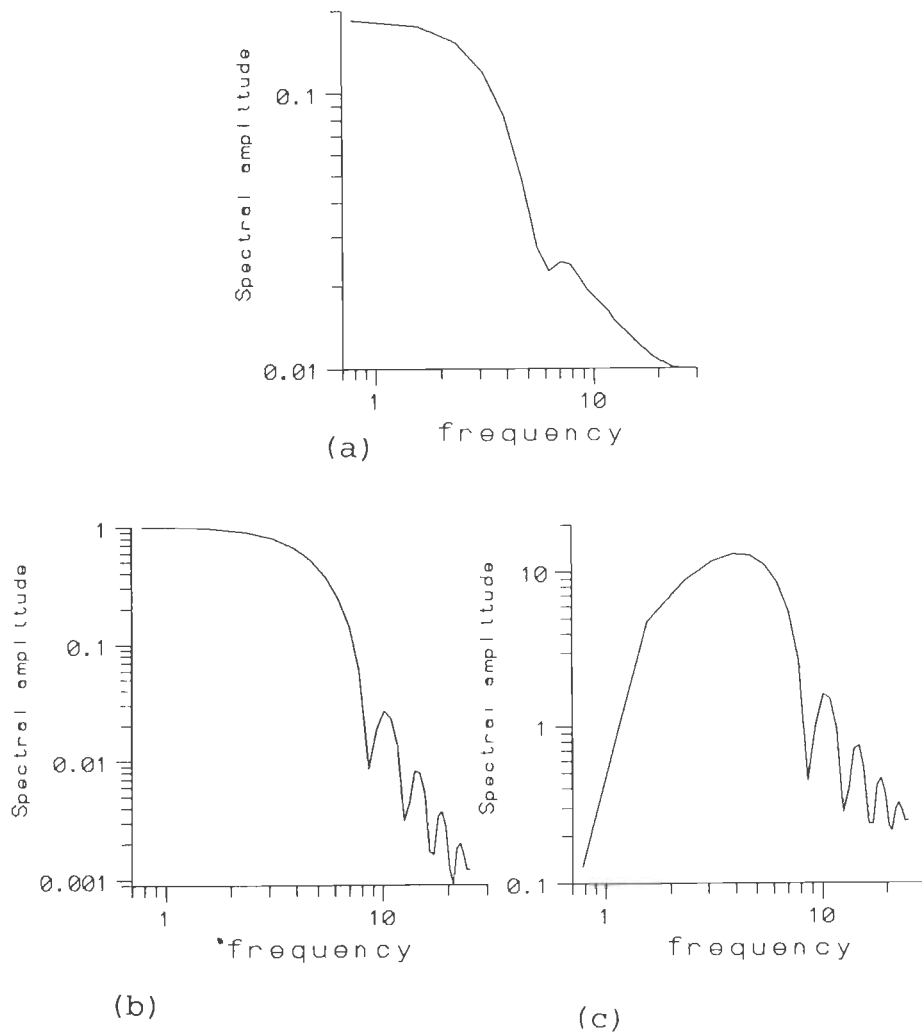


Fig 3.6 Spectrum of source time function (a) slip displacement spectrum (b) slip velocity spectrum (c) slip acceleration spectrum

First of all an estimate of the length of the fault was obtained. For this the following relation given in Kasahara (1981) was used :

$$\log L_m = 3.2 + 0.5 M \quad \dots(3.4)$$

where L_m is in cm and denotes the upper limit of the fault length for a given magnitude M . M is the surface wave magnitude. Using the following m_b - M (body wave - surface wave magnitude) relationship given by Richter (1958)

$$M = 1.59 m_b - 3.97 \quad \dots(3.5)$$

the above relation can be rewritten as

$$\log L_m = 1.215 + 0.795 m_b \quad \dots(3.6)$$

The body wave magnitude for the Uttarkashi earthquake has been given as 6.5 which gave an estimate as 24.13 km. Accordingly a value of 24 km was chosen as the length of the fault.

Aftershocks studies of the Uttarkashi earthquake were conducted by Kayal et. al. (1995), and Rastogi (1995). Of the 124 aftershocks which were located from more than 600 recorded events over a 33 day period from November 3 to December 5, 1991 there

were 77 shallower aftershocks (depth less than 5 km) and 47 deeper aftershocks (depth 5-26 km). Shallower aftershocks define two elliptical volumes, $E_1 = 15\text{km} \times 5\text{km}$ and $E_2 = 20\text{km} \times 10\text{km}$ (Fig 3.7). Most of the deeper aftershocks occurred within 15km depth and are distributed more or less in a N-S direction. These aftershocks define an elliptical volume E_3 , roughly 25km long and 15km wide. The main shock which occurred at a depth range of 10-12 km fall within this zone E_3 (Fig 3.8). The fault plane has been considered to have roughly the same area as that of elliptical zone E_3 , since the fault is found to be dipping at a low angle (14°). Accordingly the causative fault is taken to be 24km long and 16 km wide. In this way the size of the causative fault has been obtained.

3.2.6 SLIP DISTRIBUTION OVER THE FAULT PLANE

For the purpose of generating synthetic accelerograms, the whole fault has been considered to be made of a number of subfaults each of size $1\text{km} \times 1\text{km}$. The slip amount in each subfault has been estimated. The direction of slip vector has been kept constant in each subfault.

The amount of slip in each subfault has been obtained on the basis of distribution of aftershocks described by Kayal et. al. (1995).

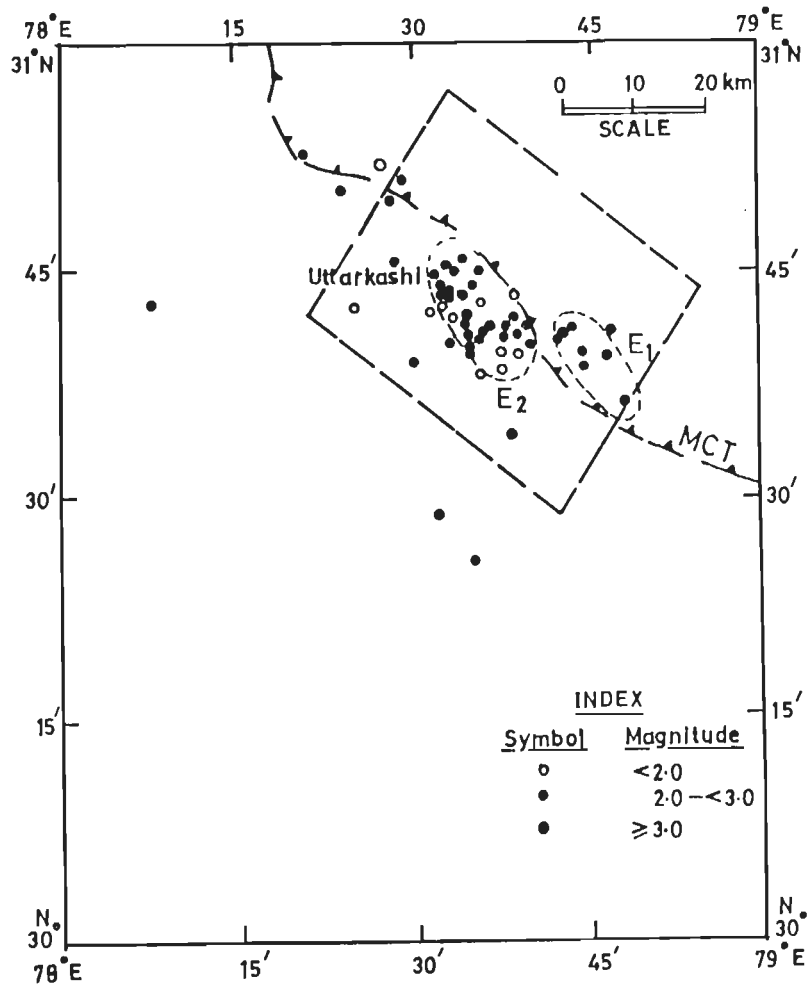


Fig 3.7 Epicentral map of the shallower aftershocks (depth < 5 km). Two elliptical volumes of the aftershocks E1 and E2 are shown. Rectangle with broken lines shows the aftershock area. (Modified after Kayal et al., 1995).

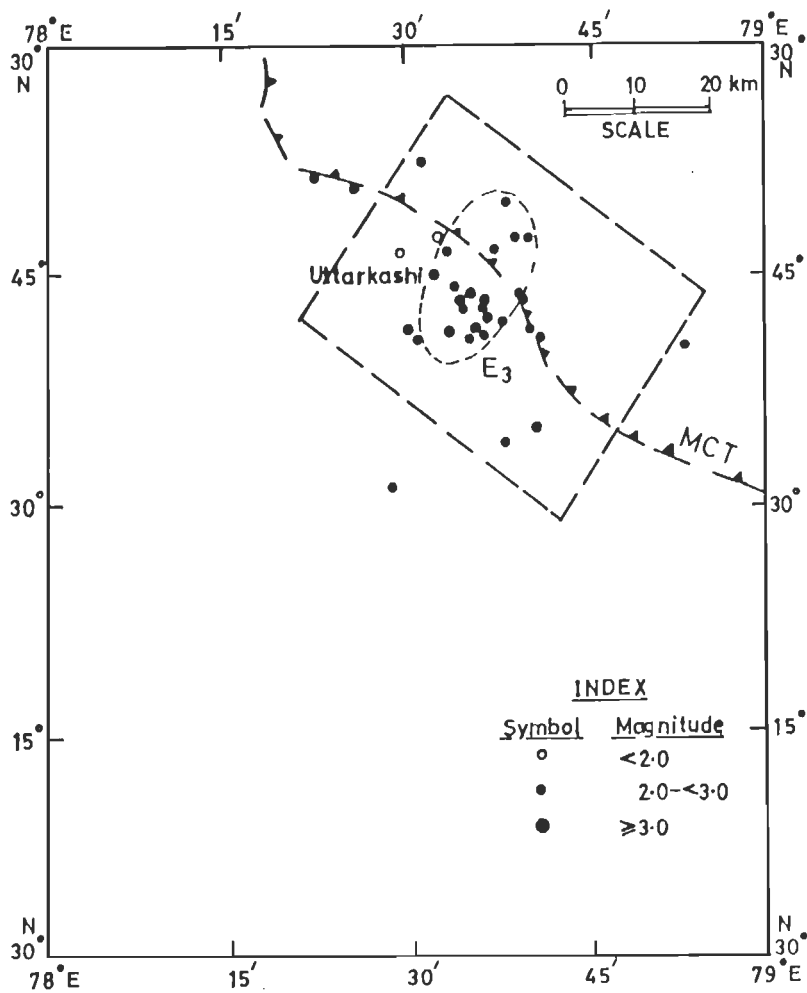


Fig 3.8 Epicentral map of the deeper aftershocks (depth :5-26 km). An elliptical volume of the aftershocks E3 is shown. Other symbols are same as in Fig 3.7 (Modified after Kayal et al., 1995).

3.3 CHOICE OF GLOBAL COORDINATE SYSTEM

The coordinates of epicentre and station location are available in terms of their latitudes and longitudes. These were converted into Cartesian coordinates x_1 and x_2 with epicentre as origin, x_1 positive towards north and x_2 positive towards east. The third coordinate x_3 was taken positive downward. All the stations were considered to be situated on the same elevation as the epicentre (above sea level) and the difference between the station elevations were ignored. Following formulae given by Lee and Stewart (1981) were used to obtain coordinates of stations on x_1 - x_2 plane

$$x_1 = 60 A (\lambda - \lambda_0) \quad \dots (3.7)$$

$$x_2 = 60 B (\phi - \phi_0) \quad \dots (3.8)$$

where λ and ϕ are the longitude and latitude of the station and λ_0 and ϕ_0 are the longitude and latitude of the epicenter in the equations (3.7) and (3.8) respectively. The values for A and B in these equations are obtained as given below:

$$A \approx 1.8553654 + 0.0062792 \sin^2\Phi + 0.0000319\sin^4\Phi \quad \dots (3.9)$$

$$B \approx 1.8428071 + 0.0187098 \sin^2\Phi + 0.0001583\sin^4\Phi \quad \dots (3.10)$$

where $\Phi = \frac{1}{2}(\phi + \phi_0)$

The stations selected in the present study are shown in Fig 3.1.

3.4 CHOICE OF LOCAL COORDINATE SYSTEM

A local (i.e. fault based) coordinate system (y_1, y_2, y_3) was chosen in the following manner . The focus which lies on the footwall side of the fault , is chosen as the origin. A line on the fault plane parallel to strike of the fault is chosen as the y_1 -axis with y_2 -axis in the up dip direction and perpendicular to the y_1 -axis. The y_3 -axis is chosen perpendicular to the fault plane and penetrating the hanging wall. Fig. 3.9 shows the global and local coordinate systems on a fault with ϕ_s as strike angle and δ as the angle of dip. The tangent to the seismic ray makes an angle i_0 at the focus. The line joining the origin to the recording station makes an angle of ϕ with the x_1 -axis.

Let $(y_1, y_2, 0)$ be the location of a point on the fault plane. The following relations convert these local coordinates $(y_1, y_2, 0)$ to global coordinates (x_1^o, x_2^o, x_3^o)

$$x_1^o = y_1 \cos\phi_s - y_2 \sin\phi_s \cos\delta \quad \dots(3.11)$$

$$x_2^o = y_1 \sin\phi_s - y_2 \cos\phi_s \cos\delta \quad \dots(3.12)$$

$$x_3^o = y_1 \sin\delta + h \quad \dots(3.13)$$

where ϕ_s is the strike , δ is the dip and h is the depth of

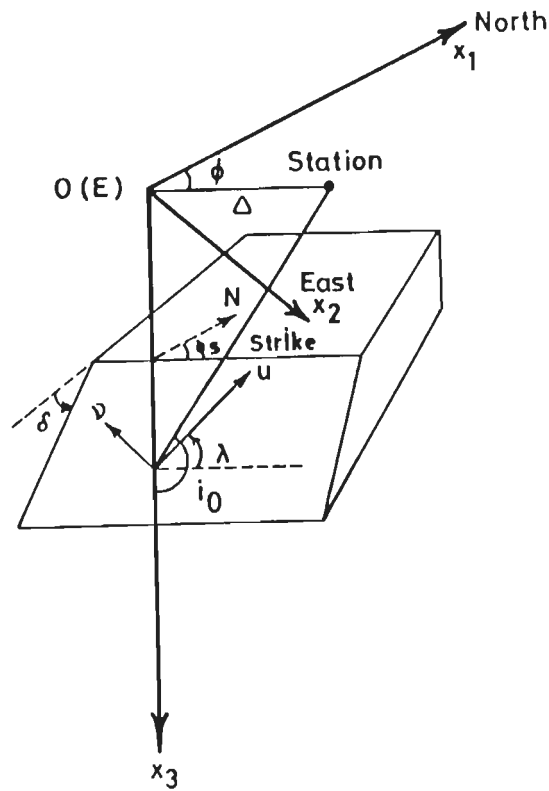


Fig 3.9 Global and local coordinate systems ϕ_s : strike, δ :dip, λ :slip angle, i_0 :take off angle , ϕ :azimuth of recording station, Δ : epicentral distance , E: epicentre v : fault normal

focus.

3.5 ROTATION OF THE AXES

The horizontal components of the generated synthetic accelerograms are in the north and east directions which are also the directions of x_1 - and x_2 -axes respectively of the global coordinate system. The horizontal components of the recorded accelerograms are not in these directions. These have been termed longitudinal (L) and transverse (T) components the directions of which vary from station to station as given in Table 3.1. For the purpose of comparison, the synthetic accelerograms were rotated so that the rotated components lie in the L and T directions for the given recording station. The following relations have been used for rotation from x_1 and x_2 directions to L and T directions :

$$u_L = u_{x_1} \cos \phi_r - u_{x_2} \sin \phi_r \quad \dots(3.14)$$

$$u_T = u_{x_1} \sin \phi_r + u_{x_2} \cos \phi_r \quad \dots(3.15)$$

where ϕ_r is the angle which the L component makes with the north, u_{x_1} and u_{x_2} are horizontal components of the synthetic accelerograms and u_L and u_T are those of the recorded data as denoted in Table 3.1 by L and T respectively.

3.6 COMPUTATIONAL PROCEDURE

For the purpose of generating synthetic synthetic accelerograms greater consideration was given to the choice of following parameters: rise time (T_0), rupture velocity (v_r), slip angle (λ) and focal depth (h). Initially synthetic accelerograms were generated to match those recorded at Uttarkashi using the unilateral rupture model. It was soon revealed that the pulse shapes as well as the times of their arrival varied rapidly for small changes in the values of rise time, rupture velocity, slip angle and the depth of focus.

Initially the focal depth was taken to be 10km, rise time 0.5 sec and rupture velocity 2.5 km/s. The results obtained were far from satisfactory. There was little improvement when bilateral rupture model was used. In both these models a uniform slip (average slip=90cm) was used in all subfaults.

It was also found that observed S-P interval on strong motion accelerograms did not equal the theoretical S-P time. This may have been due to the fact that the accelerographs were not triggered by the first P wave arrival. A difference of 2.74 s was observed in the observed and theoretical S-P times. Had the first P wave triggered the accelerograph the hypocentral distance would

have been 18.44 km from Uttarkashi with the P and S wave velocity values adopted in the study. Otherwise the actually observed hypocentral distance of 37.87 km (epicentral distance of 36.52 km) would have been possible with P wave velocity of 10.63km/s and S wave velocity of 6.14 km/s. These velocity values are obviously unrealistic. Hence it can be safely asserted that the first motions observed on accelerograms are not first P waves but some later phase. The observed and synthetic P and S arrival times at other stations are given in Table 3.2.

Table 3.2

TIME OF ARRIVALS OF P AND S WAVES IN OBSERVED AND SYNTHETIC ACCELEROGRAMS

| S. NO. | Station | Hypocentral Distance | observed | | synthetic | |
|--------|-----------|----------------------|----------|-------|-----------|-------|
| | | | t_p | t_s | t_p | t_s |
| 1 | BARKOT | 62.57 | 0.0 | 3.82 | 12.03 | 20.86 |
| 2 | BHATWARI | 21.92 | 0.0 | 2.58 | 4.22 | 7.31 |
| 3 | GHANSYALI | 43.70 | 0.0 | 3.7 | 8.41 | 14.57 |
| 4 | KOTESHWAR | 65.83 | 0.0 | 6.68 | 12.66 | 21.95 |
| 5 | PUROLA | 78.61 | 0.0 | 4.24 | 15.12 | 26.20 |
| 6 | TEHRI | 55.93 | 0.0 | 5.8 | 10.76 | 18.64 |

On account of the above fact that the accelerographs have been triggered late, only S wave proportions of observed and synthetic accelerograms have been compared. To locate the exact arrival of the S wave on observed accelerograms, particle accelerations record on L and T components at each station were plotted giving particle trajectories. Fig 3.10 shows such a particle trajectory for the Uttarkashi station. The particle motion shows a distinct change (from longitudinal to transverse) upon the arrival of S wave. The time at which this change takes place gives the instant the S wave arrives.

3.7 RUPTURE PROPAGATION MODEL

The rupture propagation model used in the present study consists of rupture starting from a single point (i.e. ,the hypocenter) and then spreading all over the fault in the form of circular rupture fronts. This is illustrated in Fig 3.11 in case of Uttarkashi station for both P and S waves. The equal time contours (isochrones) are drawn at an interval of 1s. The contours join all those points on the fault plane from which the total travel time of P (or S) waves is the same. This total travel time consists of time of rupture propagation from hypocenter to a point on the fault at the velocity of rupture propagation v_r and then the time taken at the P(or S) wave velocity from that point on the fault to the recording station.

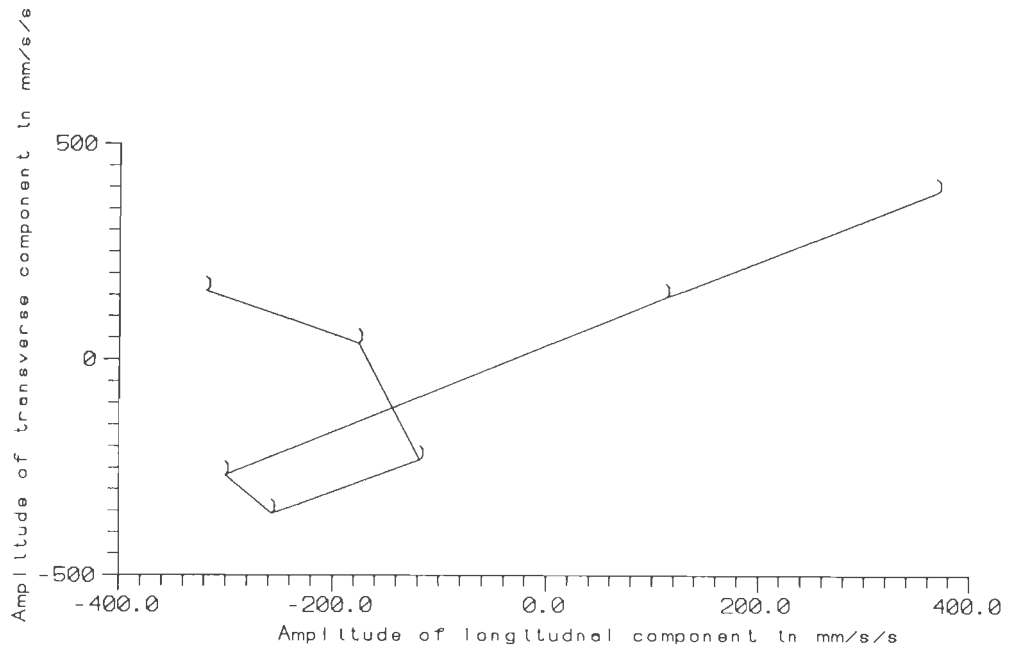
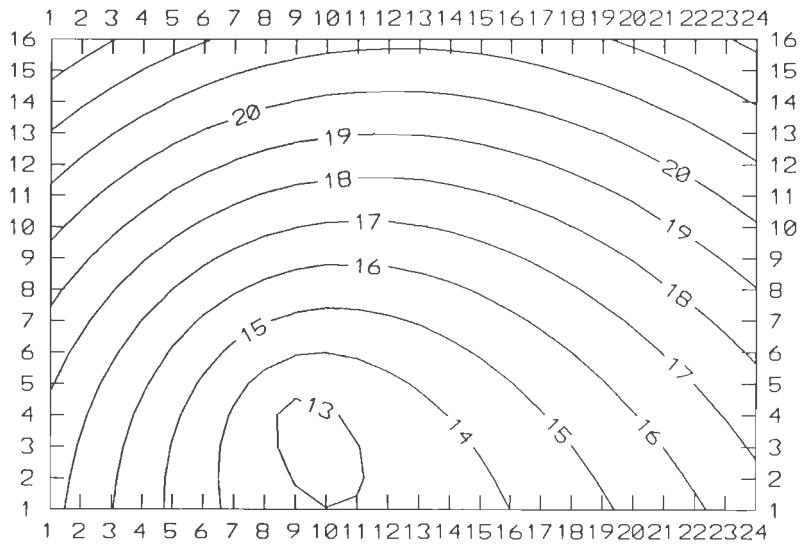
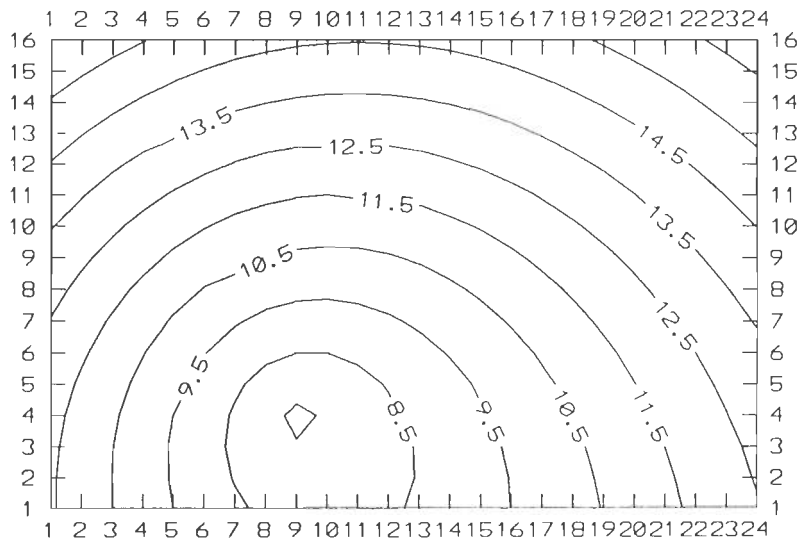


Fig 3.10 Particle motion diagram at Uttarkashi station at the time of arrival of S wave



(b)



(a)

Fig 3.11 Contours on the fault plane showing the travel time (in seconds) of (a) P and (b) S waves to the recording station at Uttarkashi.

All subfaults through which a contour passes contribute to waveform on the synthetic accelerogram at the same time instant. The amplitude of the pulse shape contributed by each subfault on a given contour differ by virtue of different geometric attenuation, radiation pattern contribution and free surface effect. These differences are slight but are found to be important.

CHAPTER 4

RESULTS AND DISCUSSIONS

4.1 INTRODUCTION

The strong motion accelerograms have been synthesized at seven selected sites which recorded the Uttarkashi earthquake of October 19, 1991. The locations of these sites along with the epicentre of the earthquake have been shown in Fig 3.1. The source parameters of the earthquake arrived at in this study on the basis of comparison of synthetic accelerograms with the observed ones are given in Table 4.1. These source parameters and the slip distribution (Fig. 4.1) were arrived at after numerous numerical experiments. The synthetic accelerograms show the longitudinal and transverse components only. The 0.0 s on the observed accelerograms show the arrival of P wave which has triggered the accelerograph. The 0.0 s on the synthetic accelerograms is the time of initiation of rupture on the fault plane. The observation that the first P arrival has not triggered the accelerographs has been mentioned and discussed in detail in Chapter 3. The accelerograms have been compared following the arrival of S waves and has been limited for that portion of the observed and synthetic accelerograms which show large amplitudes only.

TABLE 4.1

SOURCE PARAMETERS OF UTTARKASHI OF OCTOBER 19, 1991

| Sl. No. | Parameter | Value |
|---------|--|----------------------|
| 1 | Length of the Fault | 24 km |
| 2 | Width of the Fault | 16 km |
| 3 | Dip of the Fault | 14° |
| 4 | Strike of the Fault | N317° |
| 5 | Rise Time | 0.25 s |
| 6 | Rupture Velocity | 2.25 km/s |
| 7 | Slip Angle | 117° |
| 8 | Rupture Model | Circular Rupture |
| 9 | Average Slip | 87 cm |
| 10 | Maximum Slip | 175 cm |
| 11 | Location of Point of Initiation on the Fault Plane | As shown in Fig. 4.9 |

A simple method of generating synthetic accelerograms has been used in the present study. It uses simple geometric ray theory following the approach presented in Chapter 2. The causative fault is buried in an elastic half space. The effects of near surface unconsolidated materials on the synthetically generated ground motions have not been considered. Another effect that has been ignored and which could be important at stations in Himalayan region is that of topography. This has been done to simplify the computational procedure. The fault plane has been

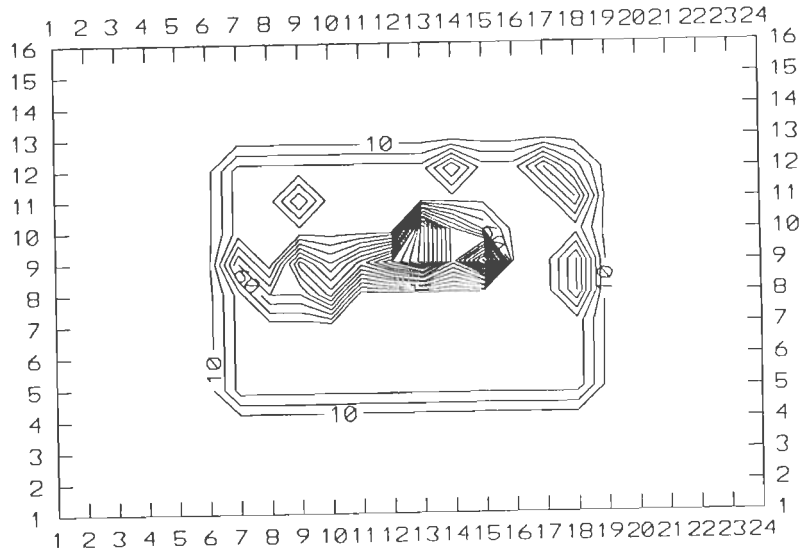


Fig 4.1 Distribution of slip amplitude on the fault plane. Contour values are in cm

divided into a number of sub-faults of equal size ($1 \text{ km} \times 1 \text{ km}$). Whereas the slip amplitude varies from one subfault to the other, the slip angle remains the same on all sub-faults. A ramp function with rounded shoulders as given by equation 3.1, has been used as the source time function for modelling the slip (i.e., displacement pulse) at a point on the fault. This form of the source time function is simple which has been analytically differentiated to obtain slip velocity and slip acceleration as given by Eqs. 3.2 and 3.3 respectively and shown in Fig.3.5. The use of the source time function for slip acceleration has made it possible to compute the direct computation of synthetic accelerograms.

The method of computation used in this study requires small number of input parameters. These are location of recording site, focal depth, length and width of the fault, velocities of P and S waves, rupture velocity and density of the half space, strike and dip of the fault plane and slip angle, size of each sub fault, rise time, sampling interval, model of rupture propagation (unilateral, bilateral or circular rupture from a point on the fault plane), and distribution of slip over the fault. It is possible to generate displacement, velocity or acceleration time history. The computational procedure takes into account radiation pattern and free surface effect completely and for each subfault separately.

4.2 RESULTS

Some of the source parameters of the Uttarkashi earthquake of October 19, 1991, arrived at on the basis of the present work, are given in the Table 4.1. Figure 4.2 to 4.8, show for each of the seven selected stations, the observed and synthetic accelerograms and the synthetic accelerograms superimposed over the observed ones. For each station separate figures have been given for each of the horizontal components. The comparison has been shown for the strong ground motions beginning with the arrival of S wave and is confined to that part of the recorded accelerograms which show large amplitudes.

Following features of the results obtained in this study are noteworthy.

4.2.1 COMPARISON OF OBSERVED AND SYNTHETIC ACCELEROGRAMS

The durations of observed and synthetic accelerograms use for comparison are given in following table.

Table 4.2

DETAILS OF THE SUPERIMPOSED ACCELEROGRAMS

| S. No. | Station | Fig No. | Duration of Superimposed Accelerograms | Observed (s) | Synthetic (s) |
|--------|------------|--------------|--|--------------|---------------|
| | | | | from-to | from-to |
| 1 | BARKOT | 4.2B 4.2D | 7 s | 3.82-10.82 | 20.86-27.86 |
| 2 | BHATWARI | 4.3B 4.3D | 8 S | 2.58-10.58 | 7.31-15.31 |
| 3 | GHANSYALI | 4.4B 4.4D | 10 S | 3.70-13.70 | 14.57-24.57 |
| 4 | KOTESHWAR | 4.5B 4.5D | 10 S | 6.68-16.68 | 21.96-31.96 |
| 5 | PUROLA | 4.6B 4.6D | 5 S | 4.24- 9.24 | 26.20-31.20 |
| 6 | TEHRI | 4.7B 4.7D | 7 S | 5.80-12.80 | 18.64-25.64 |
| 7 | UTTARKASHI | 4.8B 4.8D | 5.5 S | 2.60- 8.10 | 12.62-18.12 |

A close examination of Figs 4.2 to 4.8 reveals the following:

(a) The observed and synthetic accelerograms match fairly closely at all the seven stations. The match is observed to be

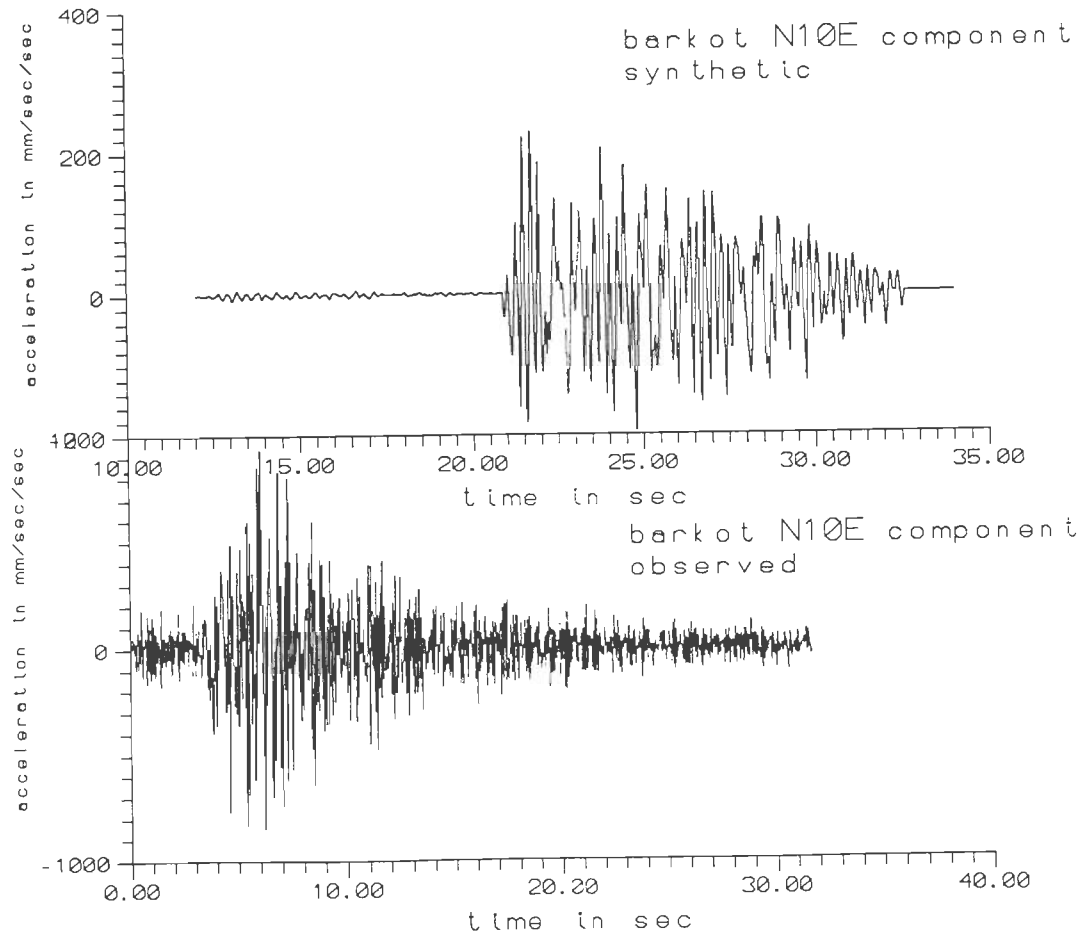


Fig 4.2(a) Observed and Synthetic accelerograms for the N10E component at Barkot

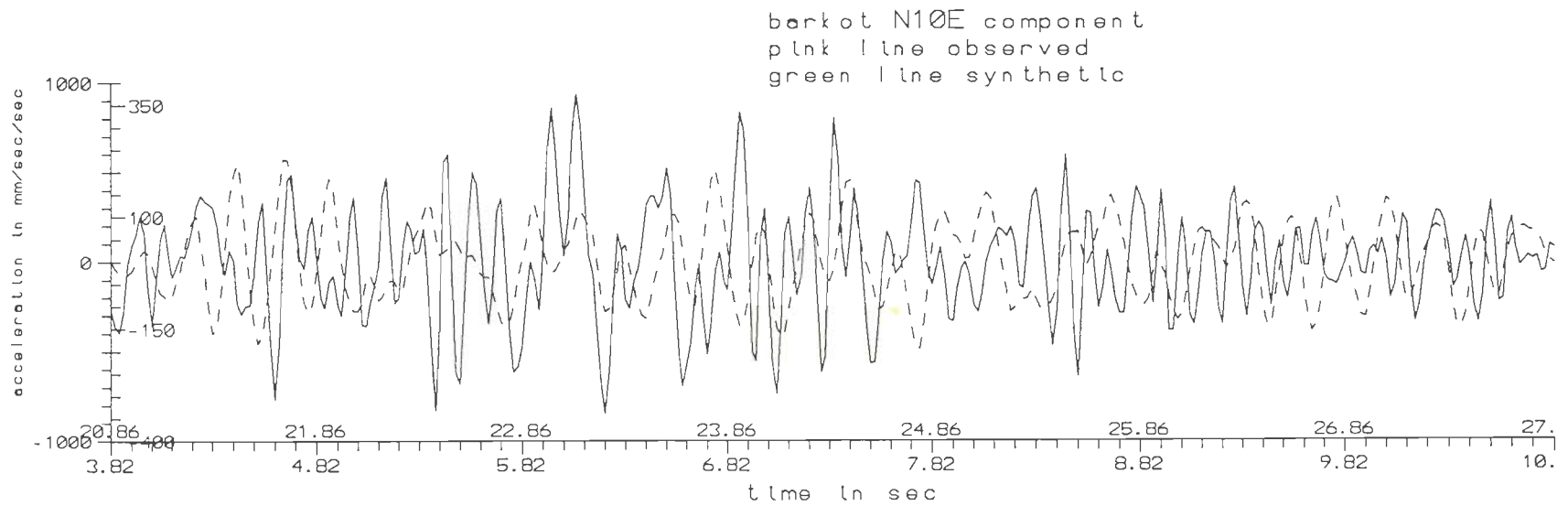


Fig 4.2(b) Synthetic accelerogram superimposed over the observed ones for the N10E component at Barkot.

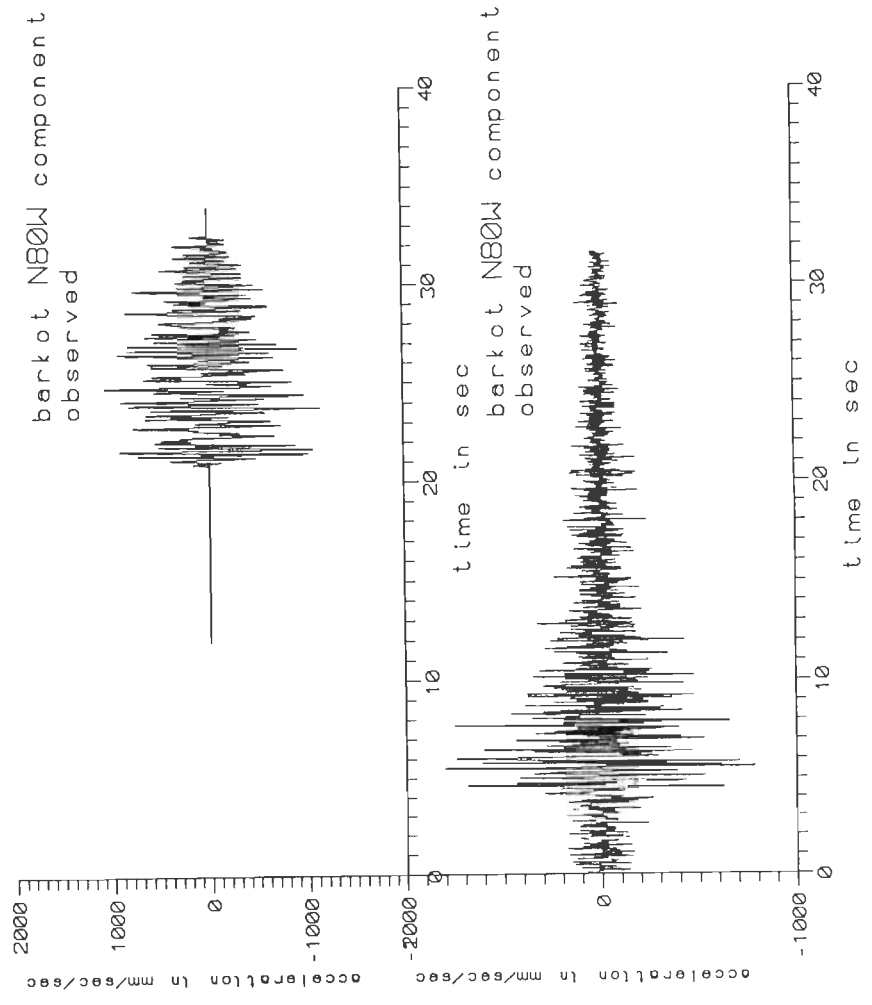


Fig 4.2(c) Observed and Synthetic accelerograms for the N80W component at Barkot.

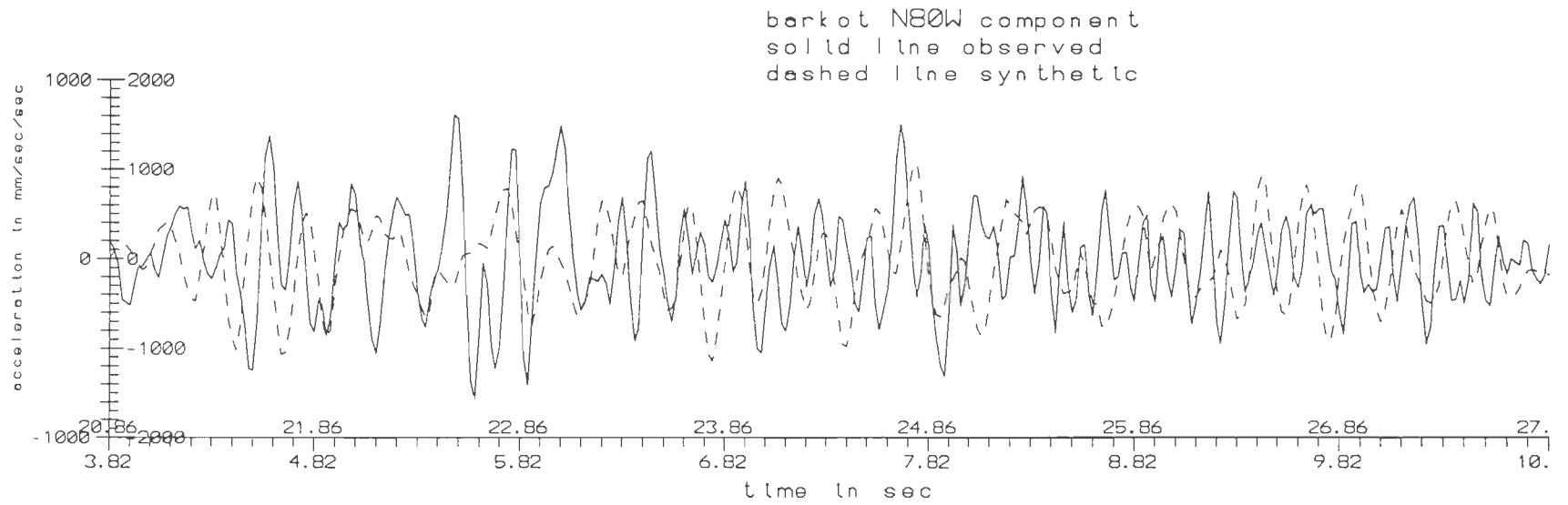


Fig 4.2(d) Synthetic accelerogram superimposed over the observed ones for the N80W component at Barkot.

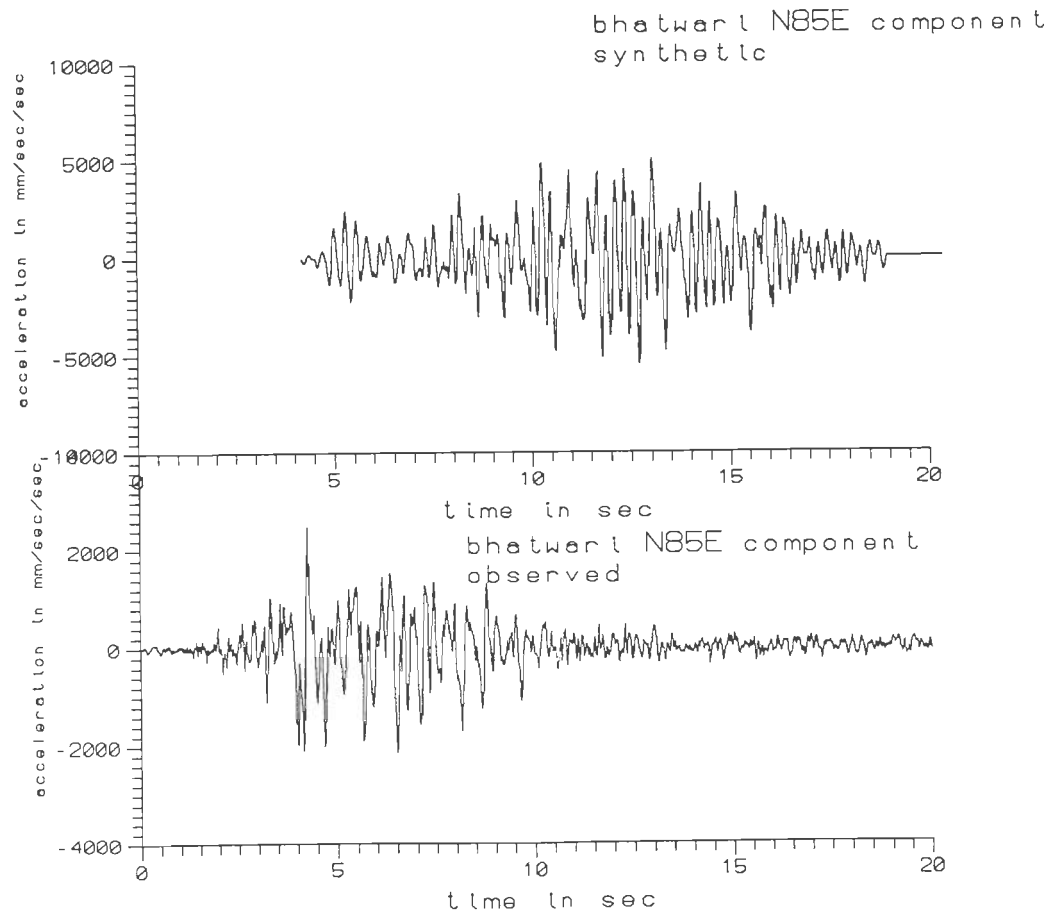


Fig 4.3(a) Observed and Synthetic accelerograms for the N85E component at Bhatwari

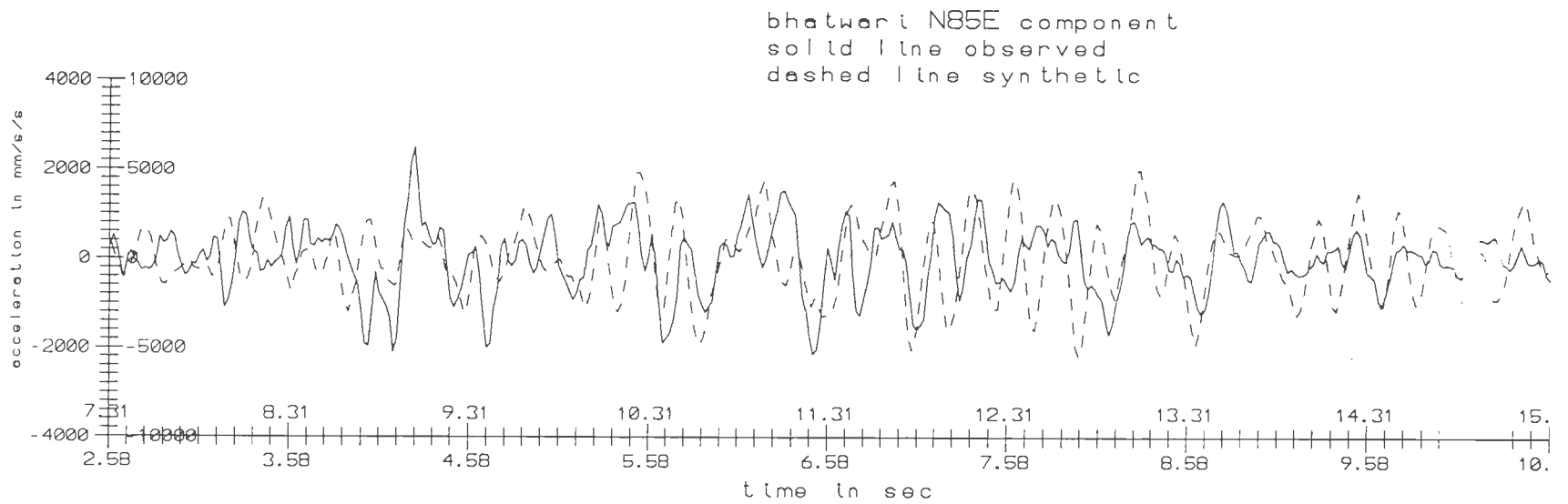


Fig 4.3(b) Synthetic accelerogram superimposed over the observed ones for the N85E component at Bhatwari.

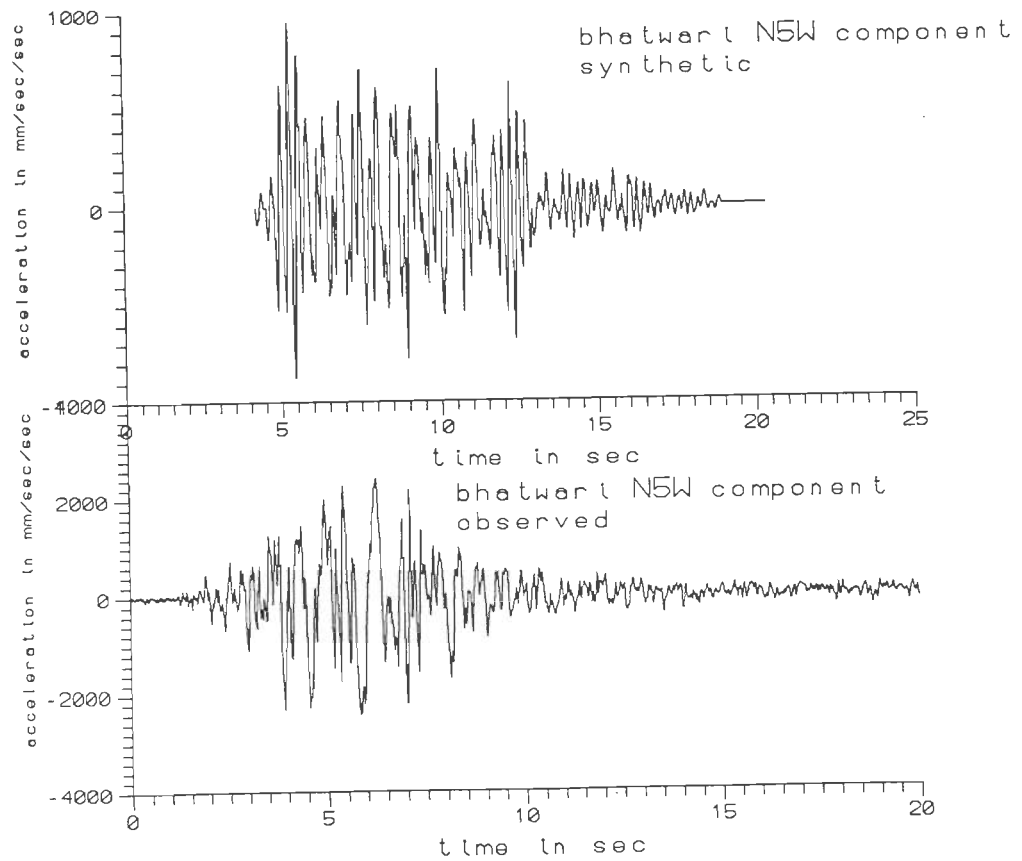


Fig 4.3(c) Observed and Synthetic accelerograms for the N5W component at Bhatwari.

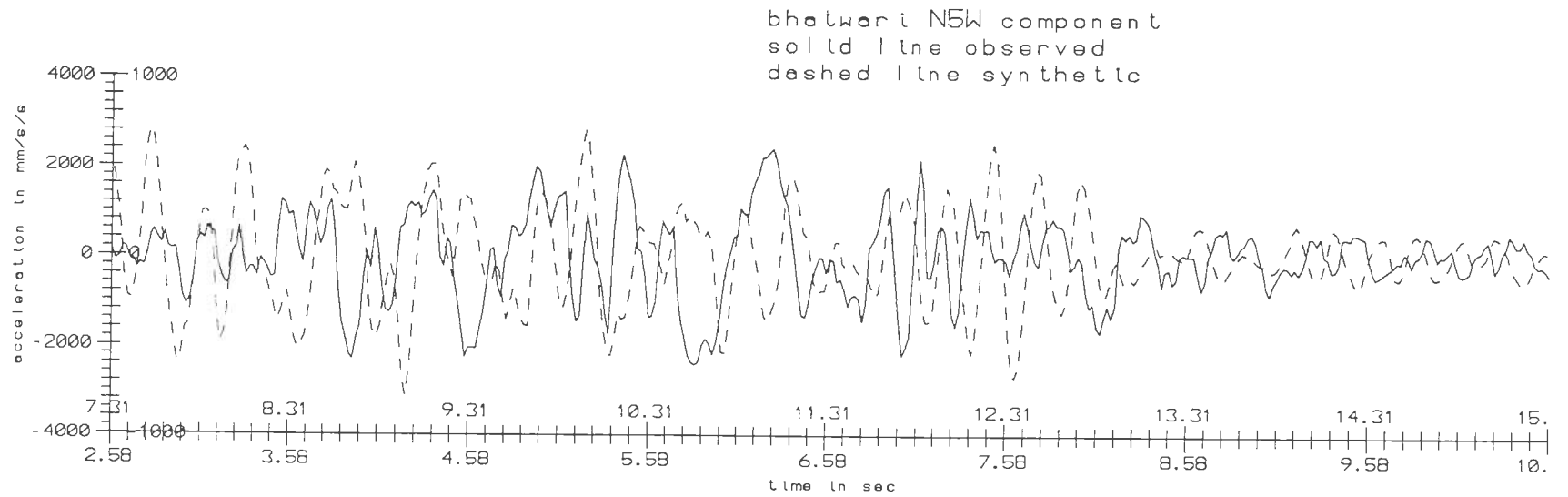


Fig 4.3(d) Synthetic accelerogram superimposed over the observed ones for the N5W component at Bhatwari.

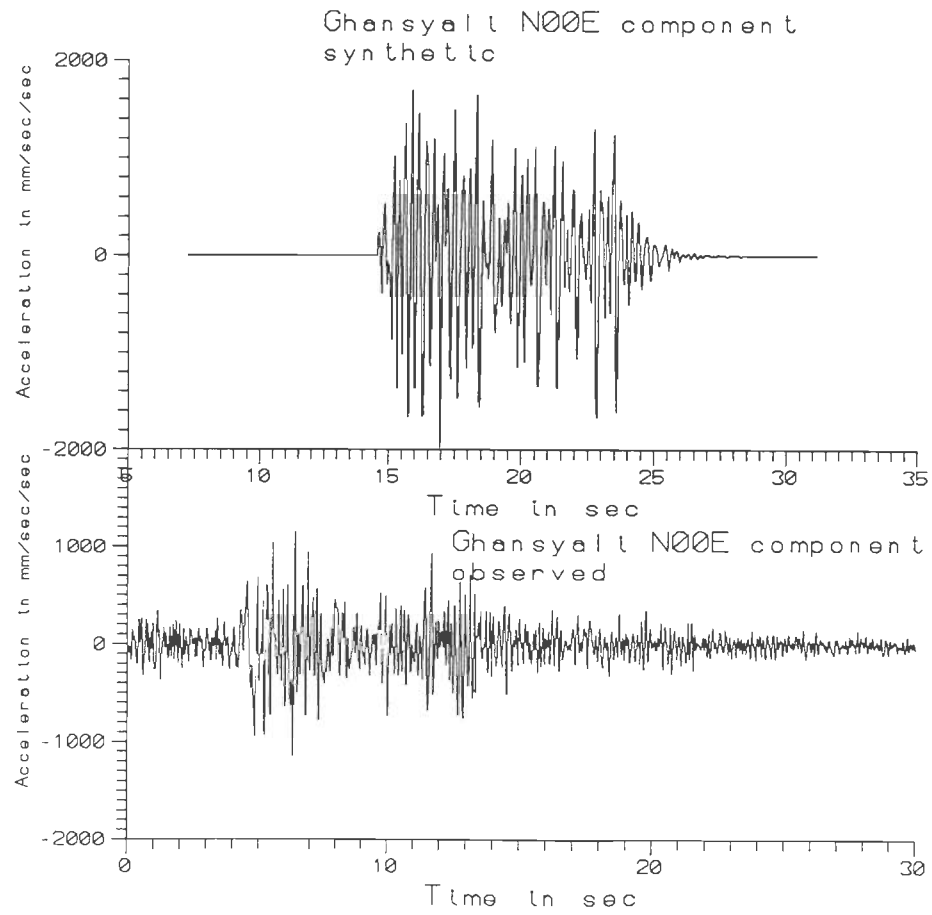


Fig 4.4(a) Observed and Synthetic accelerograms for the N00E component at Ghansyali.

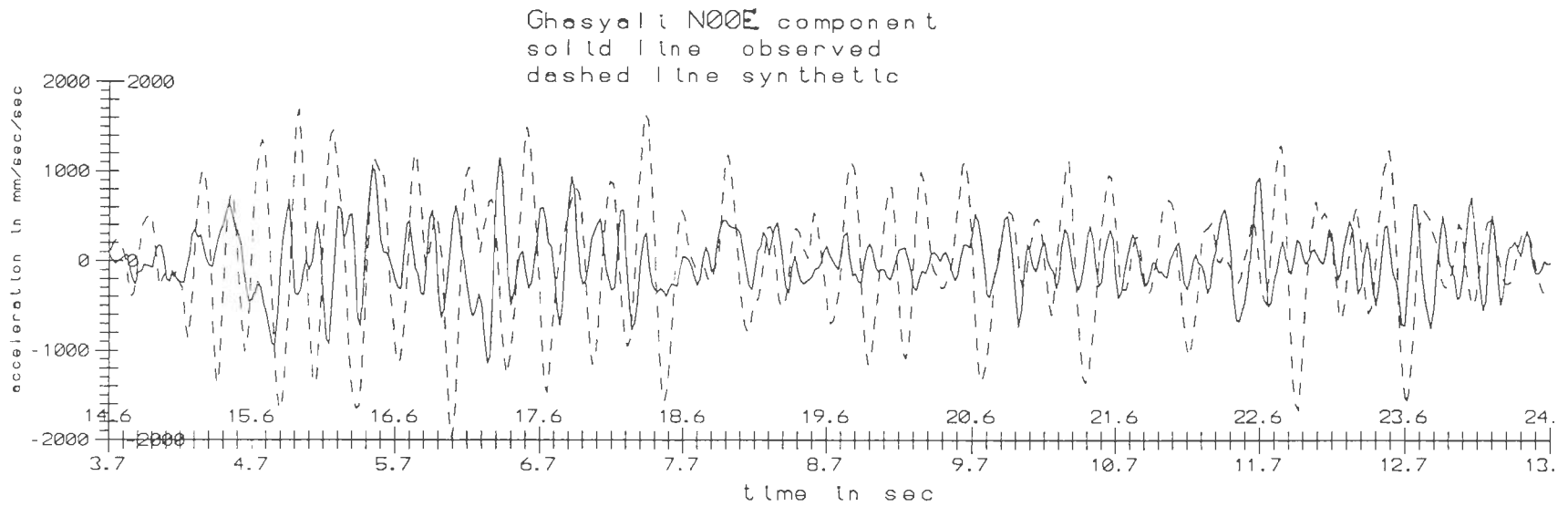


Fig 4.4(b) Synthetic accelerogram superimposed over the observed ones for the N00E component at Ghansyali.

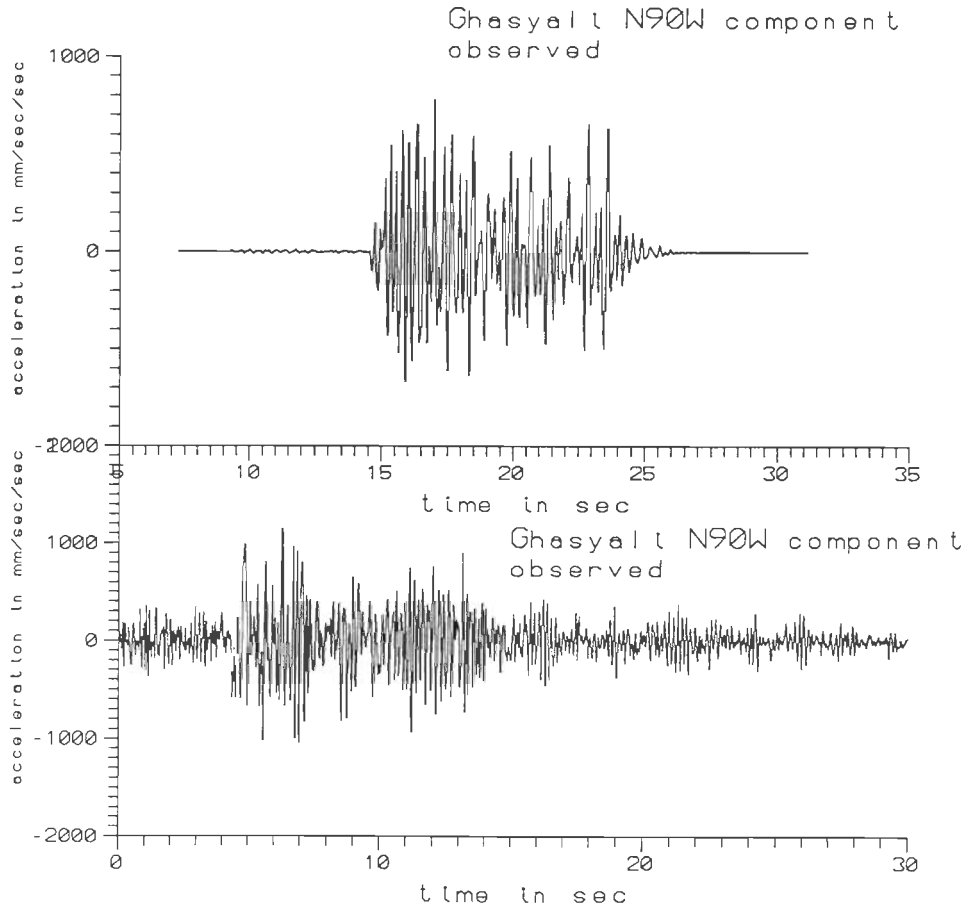


Fig 4.4(c) Observed and Synthetic accelerograms for the N90W component at Ghansyali.

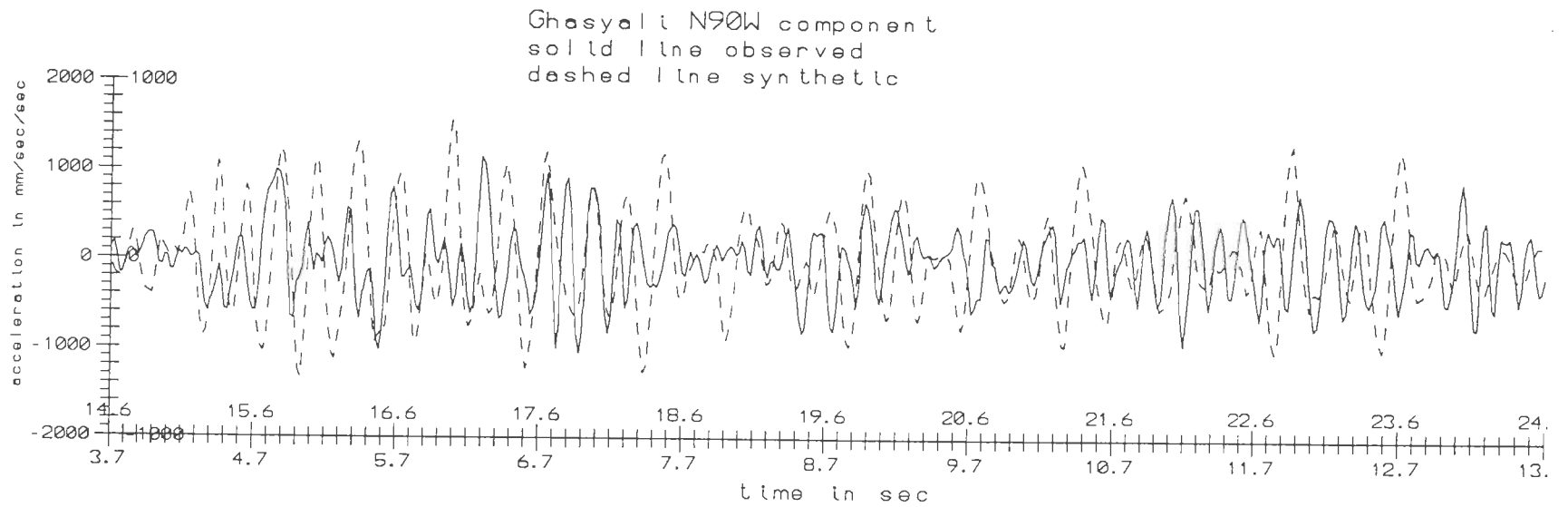


Fig 4.4(d) Synthetic accelerogram superimposed over the observed ones for the N90W component at Ghansyali.

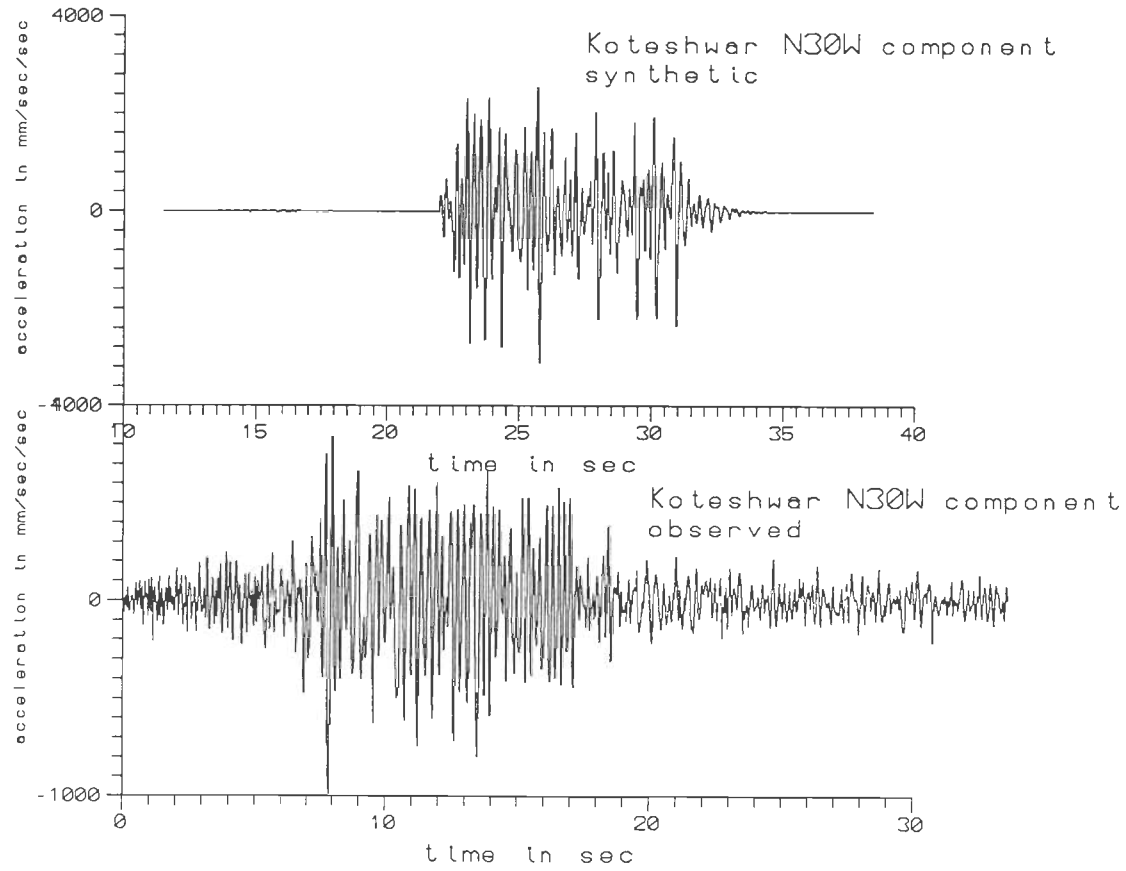


Fig 4.5(a) Observed and Synthetic accelerograms for the N30W component at Koteswar.

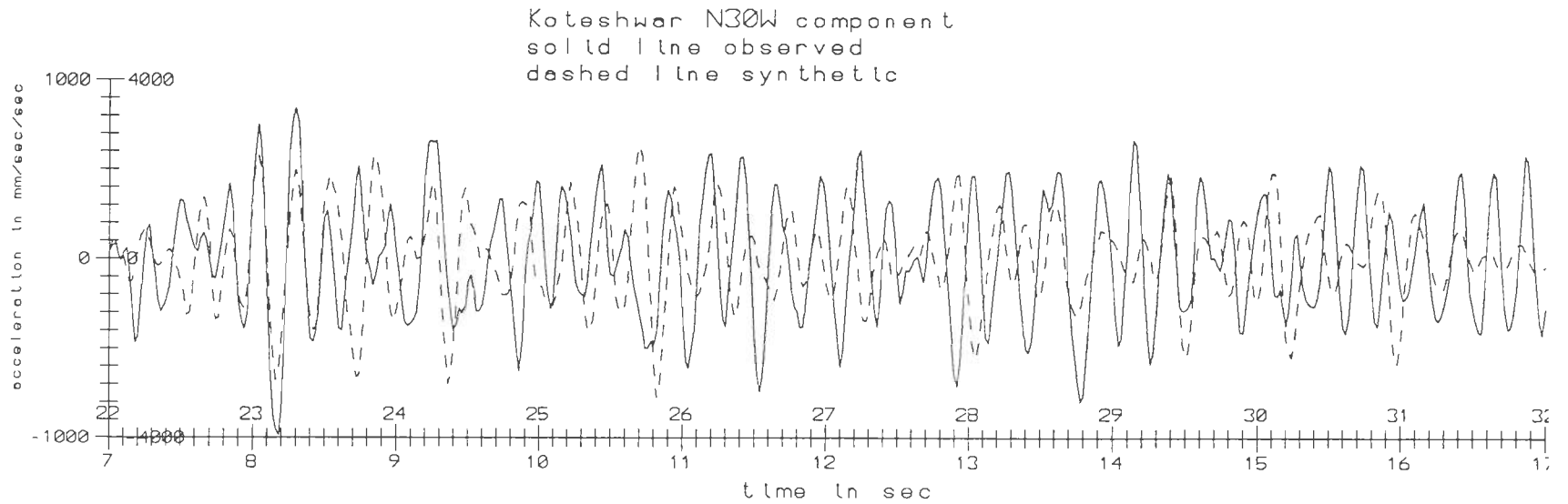


Fig 4.5(b) Synthetic accelerogram superimposed over the observed ones for the N30W component at Koteshwar.

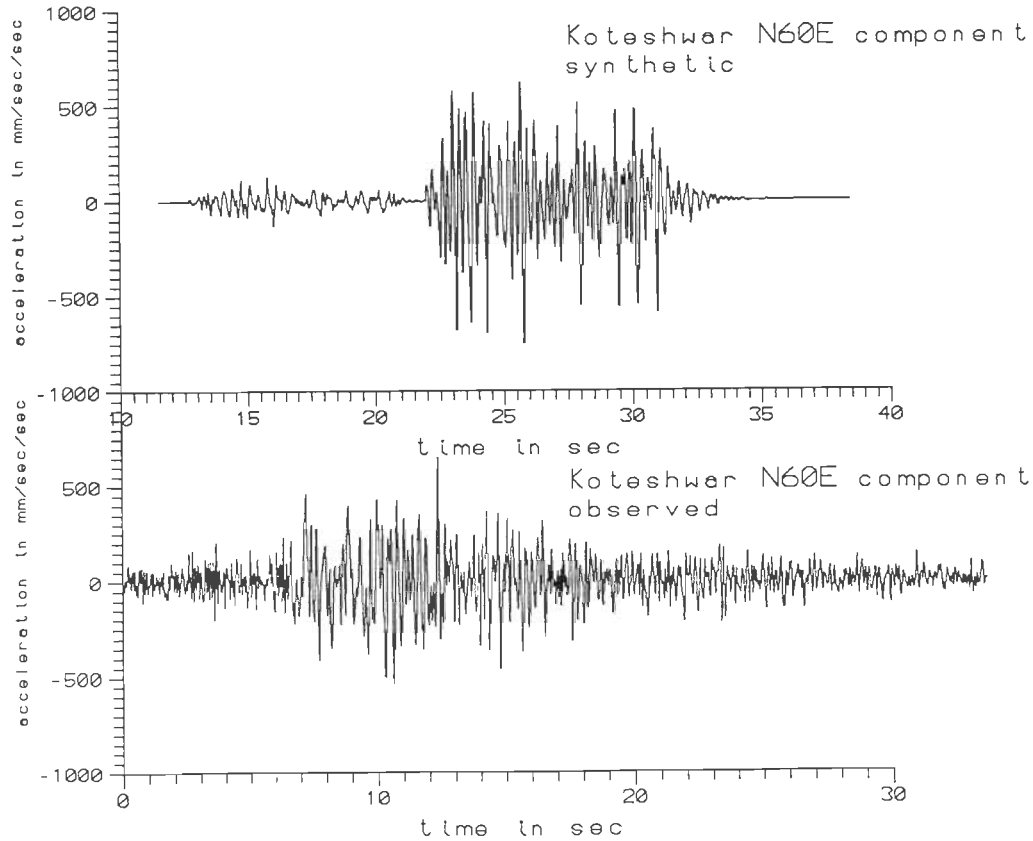


Fig 4.5(c) Observed and Synthetic accelerograms for the N60E component at Koteshwar.

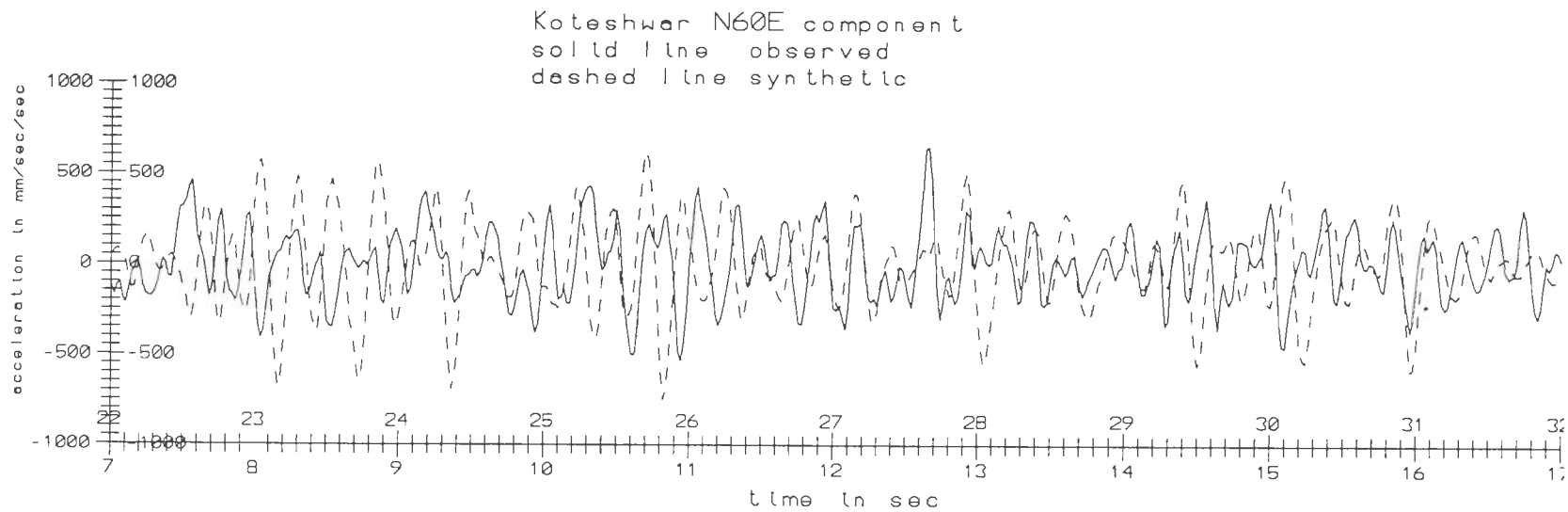


Fig 4.5(d) Synthetic accelerogram superimposed over the observed ones for the N60E component at Koteshwar.

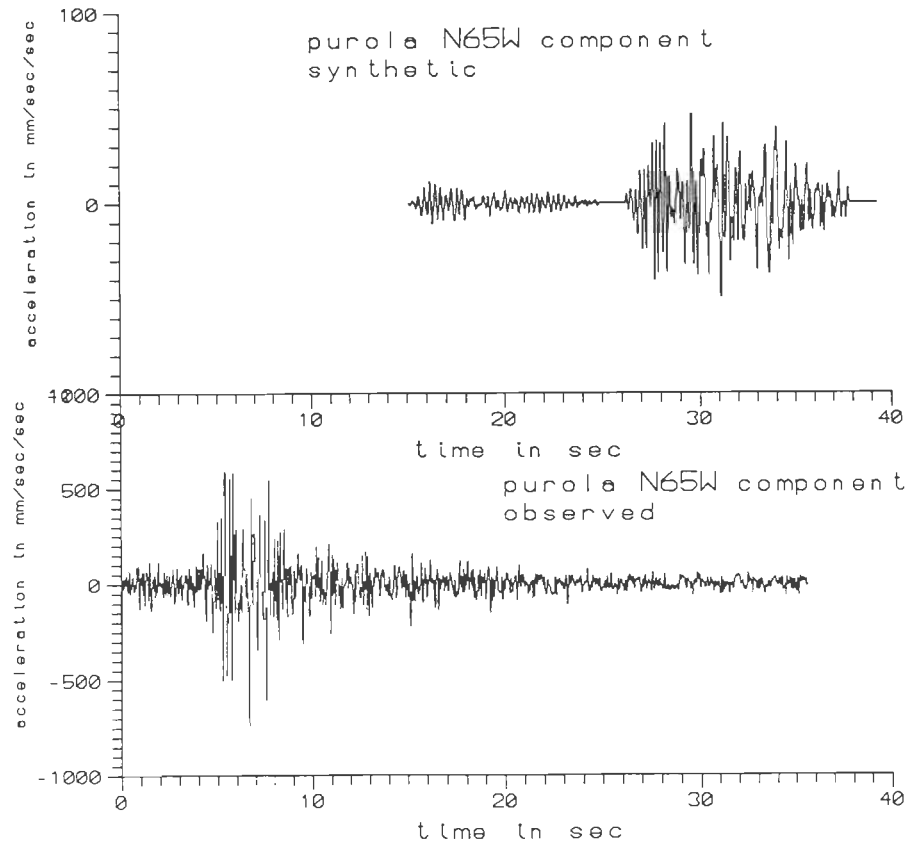


Fig 4.6(a) Observed and Synthetic accelerograms for the N65W component at Purola.

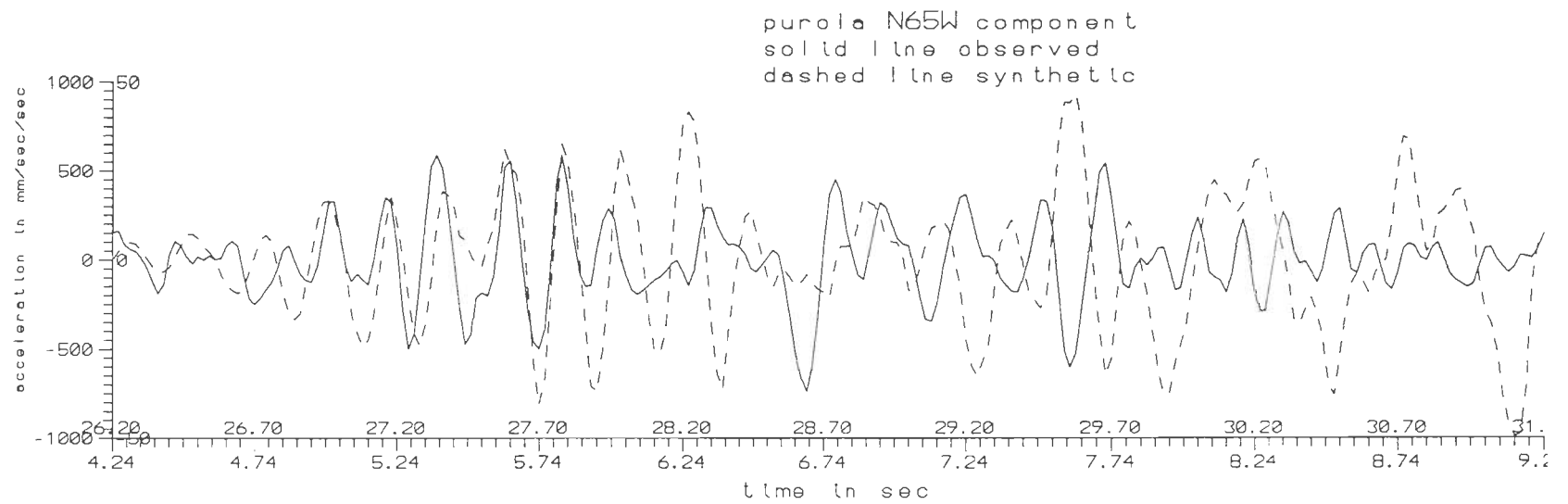


Fig 4.6(b) Synthetic accelerogram superimposed over the observed ones for the N65W component at Purola.

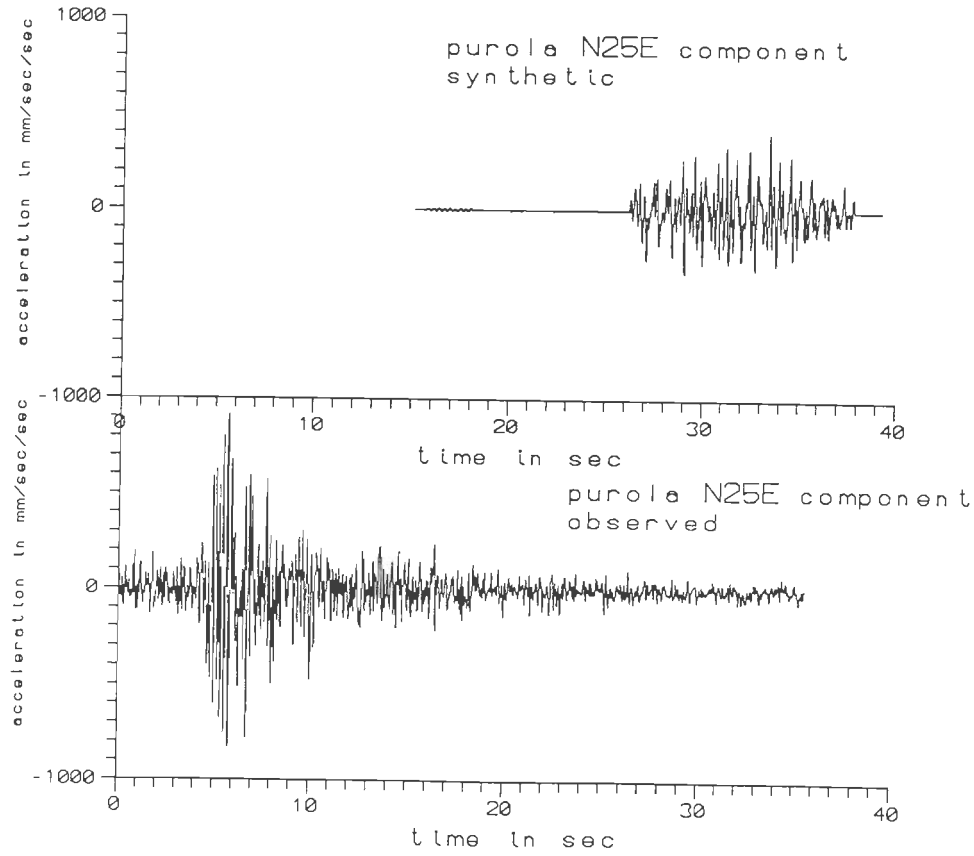


Fig 4.6(c) Observed and Synthetic accelerograms for the N25E component at Purola.

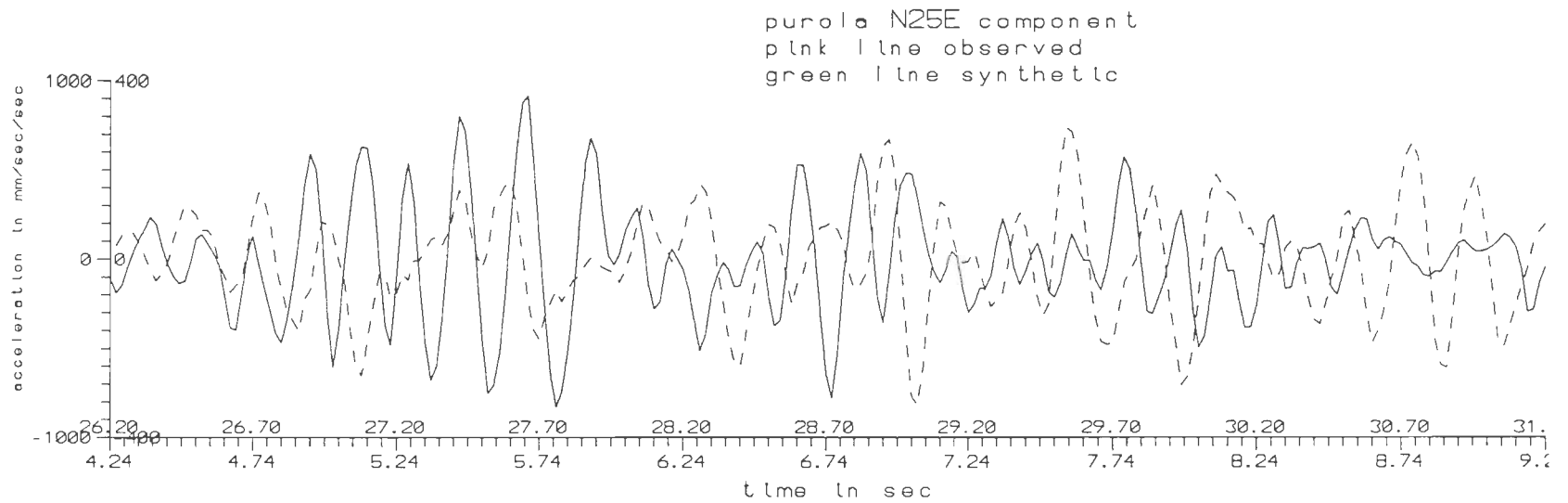


Fig 4.6(d) Synthetic accelerogram superimposed over the observed ones for the N25E component at Purola.

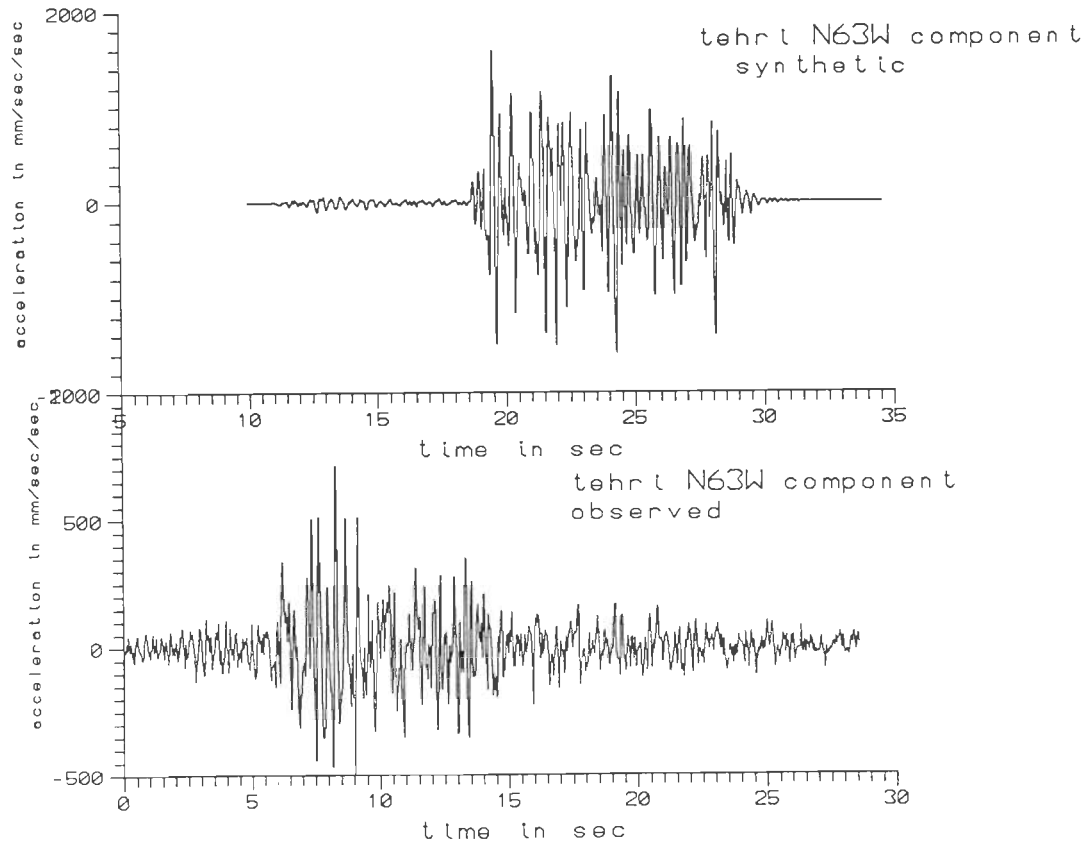


Fig 4.7(a) Observed and Synthetic accelerograms for the N63W component at Tehri.

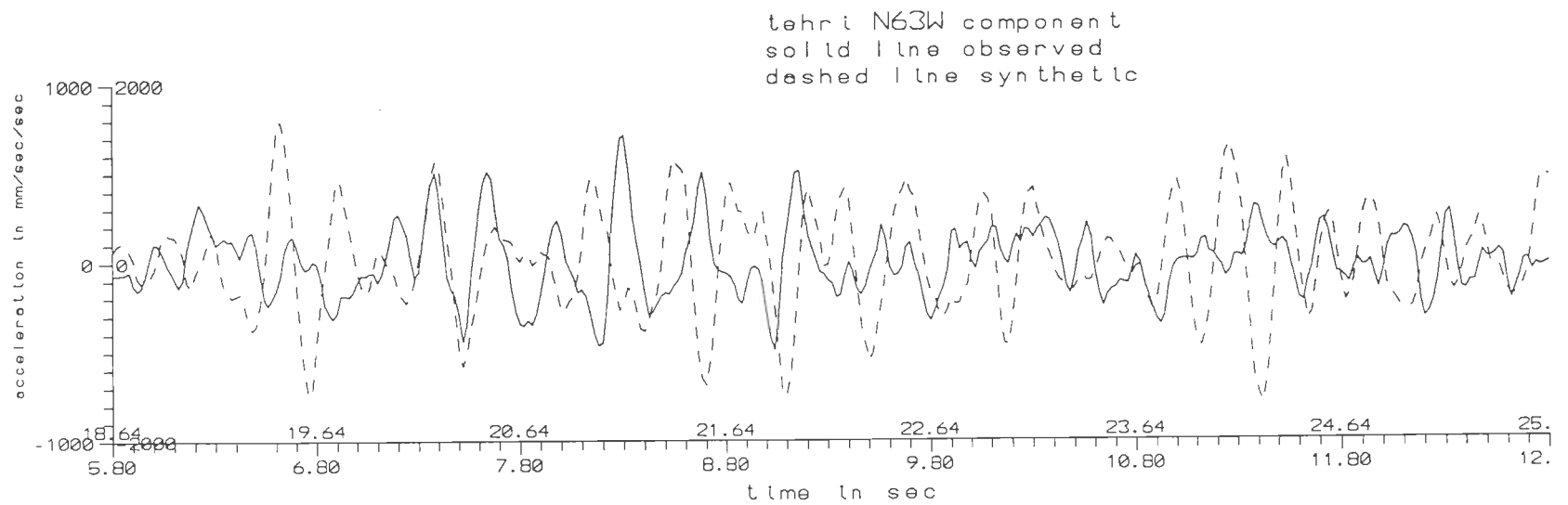


Fig 4.7(b) Synthetic accelerogram superimposed over the observed ones for the N63W component at Tehri.

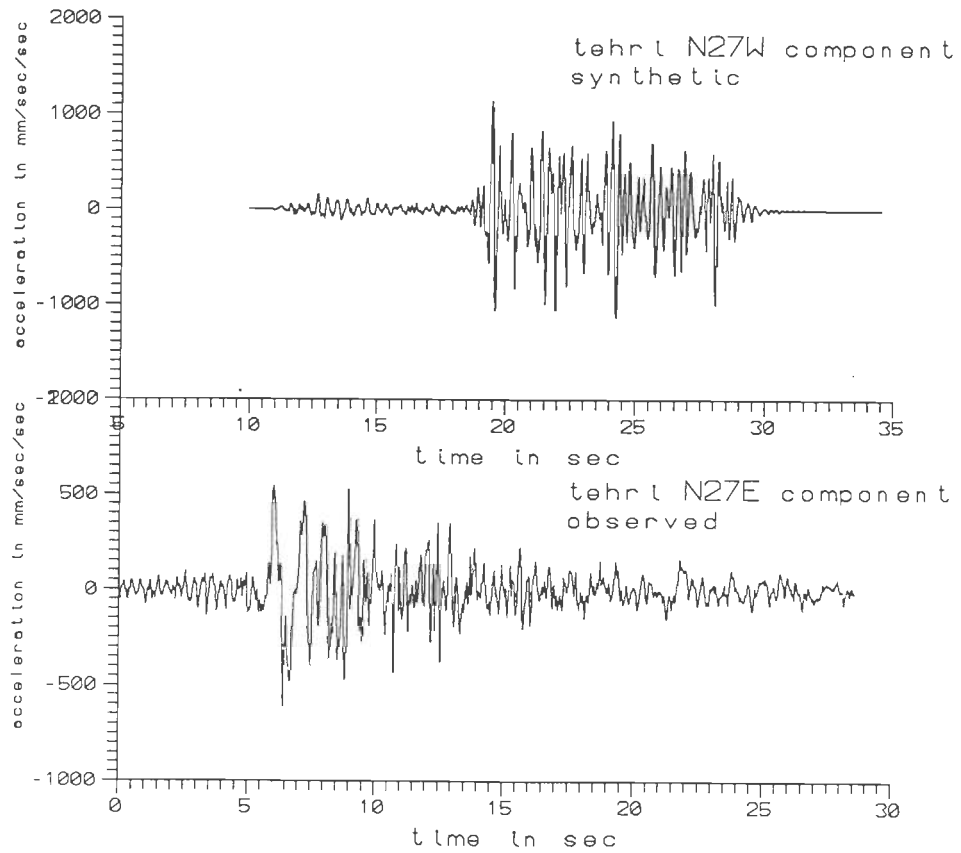


Fig 4.7(c) Observed and Synthetic accelerograms for the N27E component at Tehri.

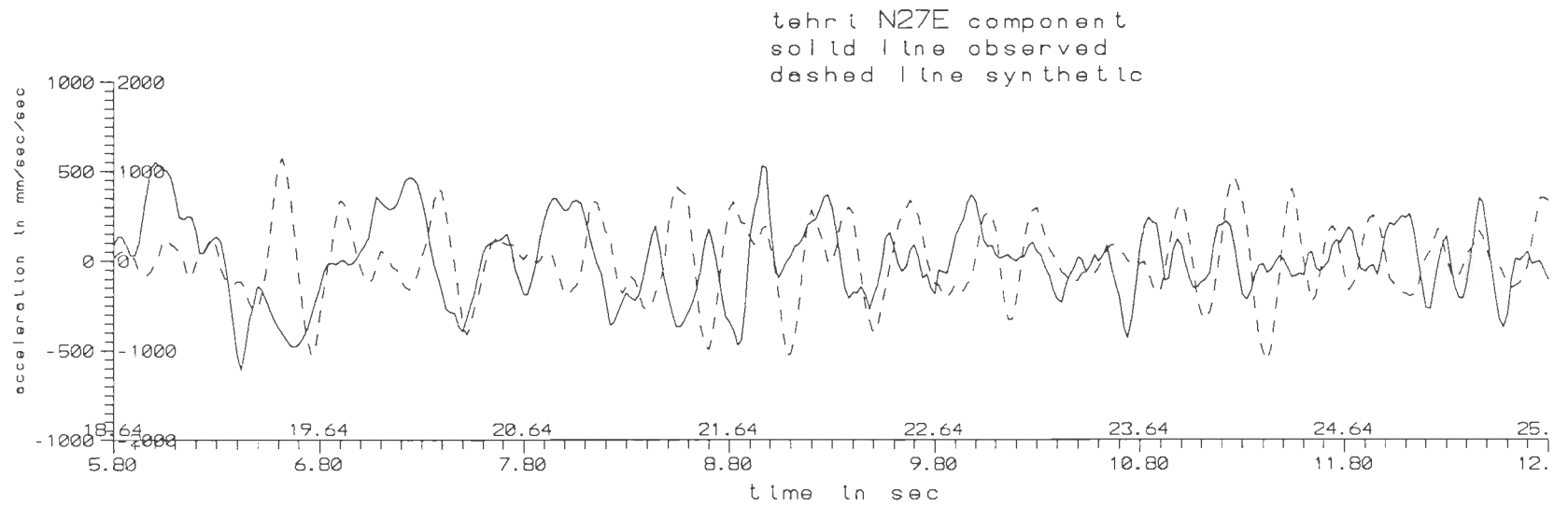


Fig 4.7(d) Synthetic accelerogram superimposed over the observed ones for the N27E component at Tehri.

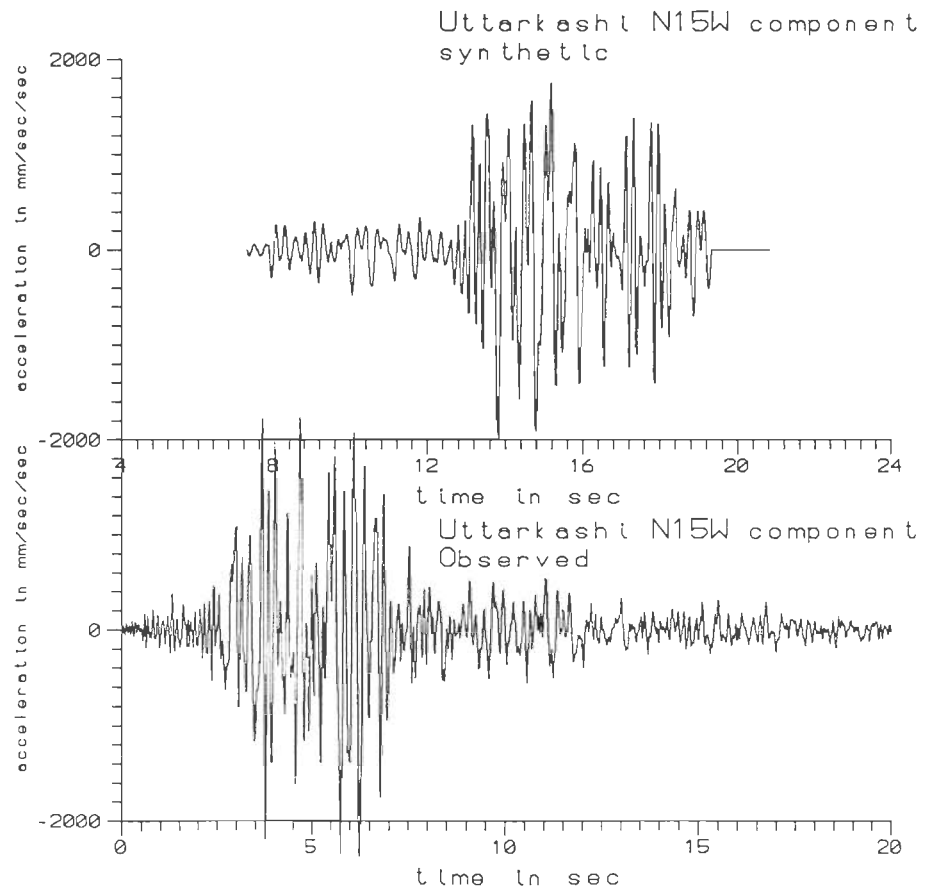


Fig 4.8(a) Observed and Synthetic accelerograms for the N15W component at Uttarkashi.

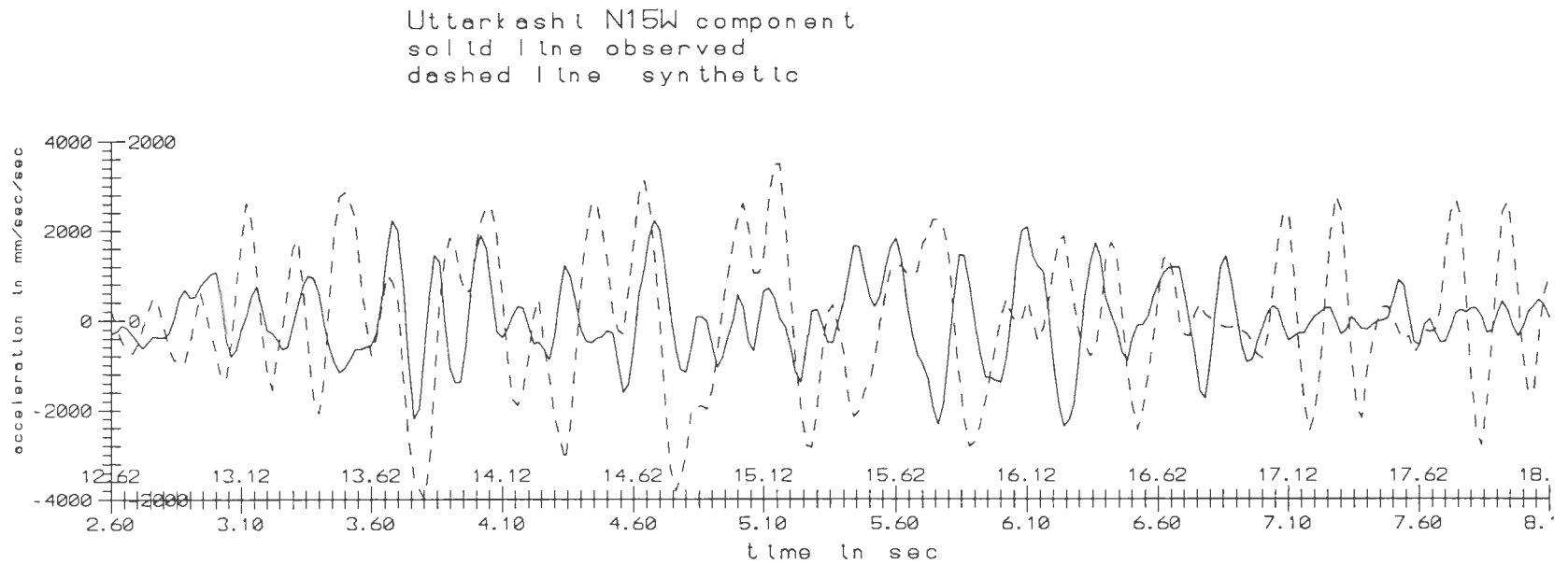


Fig 4.8(b) Synthetic accelerogram superimposed over the observed ones for the N15W component at Uttarkashi.

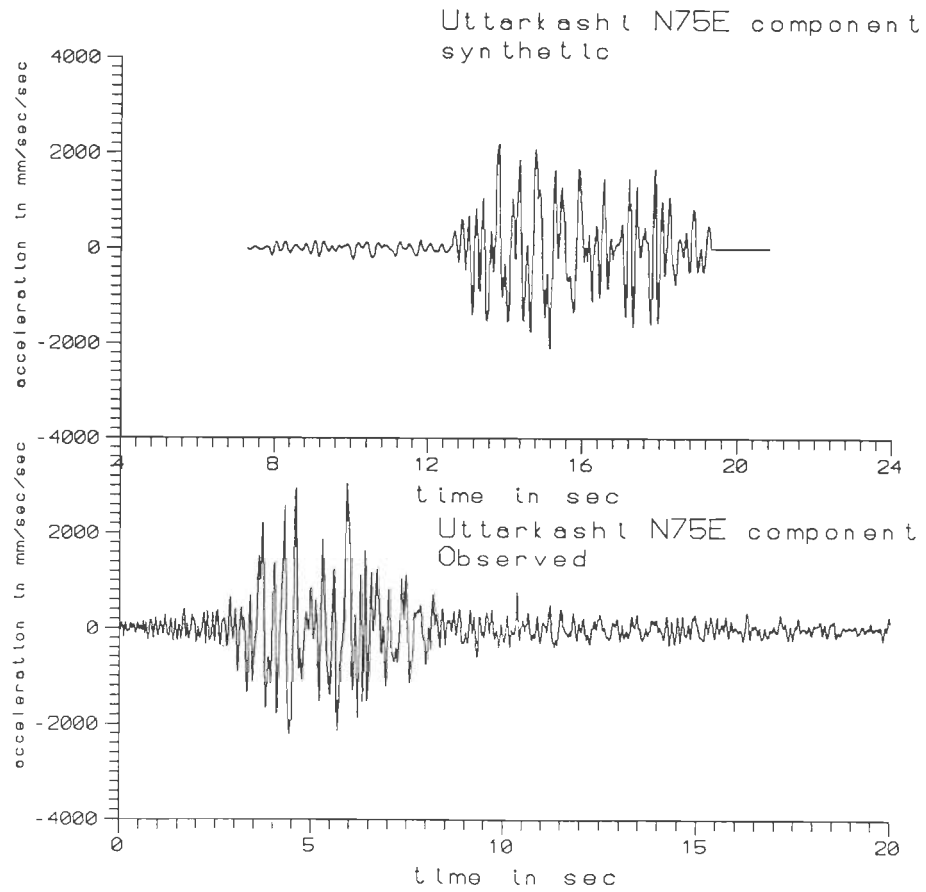


Fig 4.8(c) Observed and Synthetic accelerograms for the N75E component at Uttarkashi.

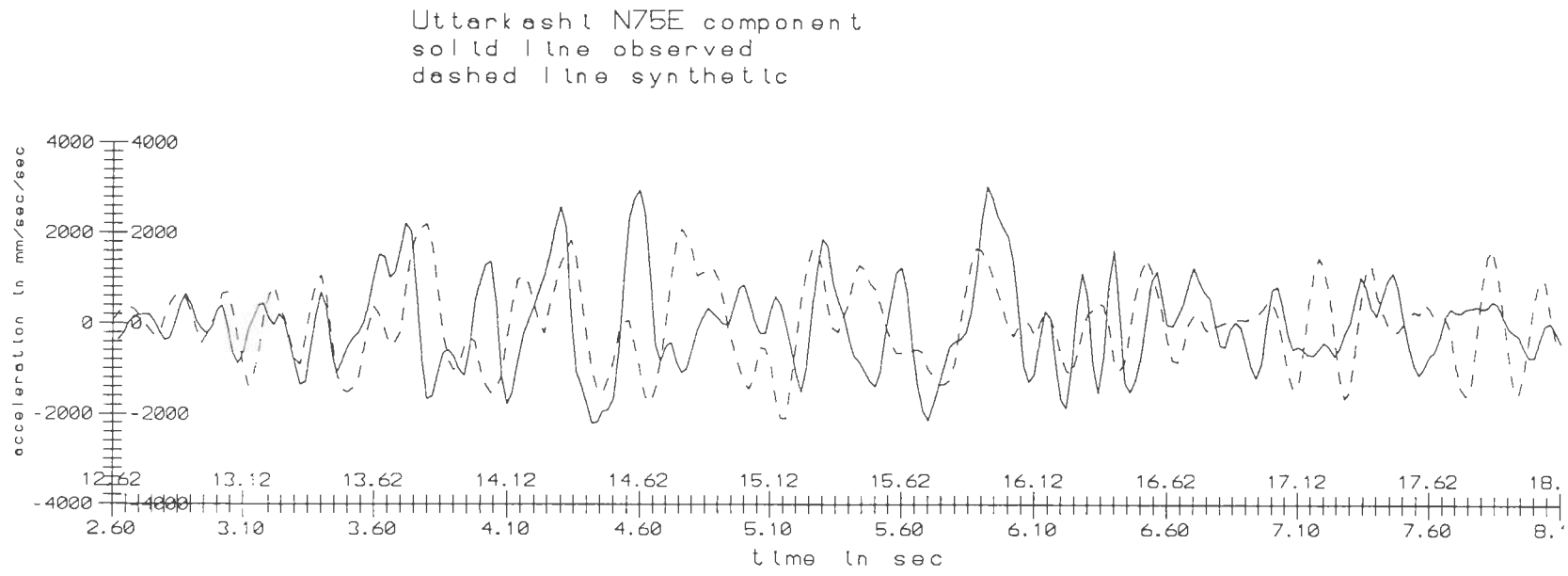


Fig 4.8(d) Synthetic accelerogram superimposed over the observed ones for the N75E component at Uttarkashi.

the best at Koteshwar (Fig 4.5B,4.5D), Ghansyali (Fig 4.4B,4.4D) and in Uttarkashi (Fig 4.8B,4.8D)

(b) A good number of peaks lie close to each other. The shapes of the acceleration pulses are very nearly same although their amplitudes show some deviation.

4.2.2 SOURCE PARAMETERS

(a) The source parameters of the Uttarkashi earthquake of October 19,1991 obtained in the presented study are very close to those reported by Khattri et al.(1994) for the Uttarkashi earthquake (Table 4.3)

Table 4.3
COMPARISON OF SOURCE PARAMETRS

| Sl. No. | work carried out by | Source Parameters | | | | |
|---------|----------------------|-------------------|--------------|----------------------------------|-----------|------------------|
| | | Fault size | Average Slip | Seismic Moment | Rise Time | Moment Magnitude |
| 1 | Khattri et al.(1994) | 30 km ×20 km | 82 cm | 1.46×10^{26} dyne-cm | 0.3 s | 6.74 |
| 2 | Present work | 24 km ×16 km | 87 cm | 1.0×10^{26} dyne-cm | 0.25s | 6.63 |

(b) The value of the seismic moment obtained in the present study is different from those of earlier studies which may be attributed to the variation in the slip amplitude over the fault plane

4.2.3 SLIP DISTRIBUTION

The distribution of amount of slip on the fault plane (Fig 4.1) show two regions having large concentration of high amplitude. The centres of these regions lie at times 2.44s and 3.78s after the initiation of the rupture.

4.2.4 LOCATION OF THE POINT OF RUPTURE INITIATION

The point of rupture initiation (i.e., the focus) lies at a depth of 10 km from the surface of the earth and is situated at a point on the fault plane lying at a distance of 9 km in the strike direction and 4 km in the updip direction from the lower northeastern corner of the fault as shown in (Fig 4.9)

4.3 DISCUSSION

One of the objectives of the present work was to determine the extent to which the source parameters determined from the analysis of teleseismic data compare with those obtained

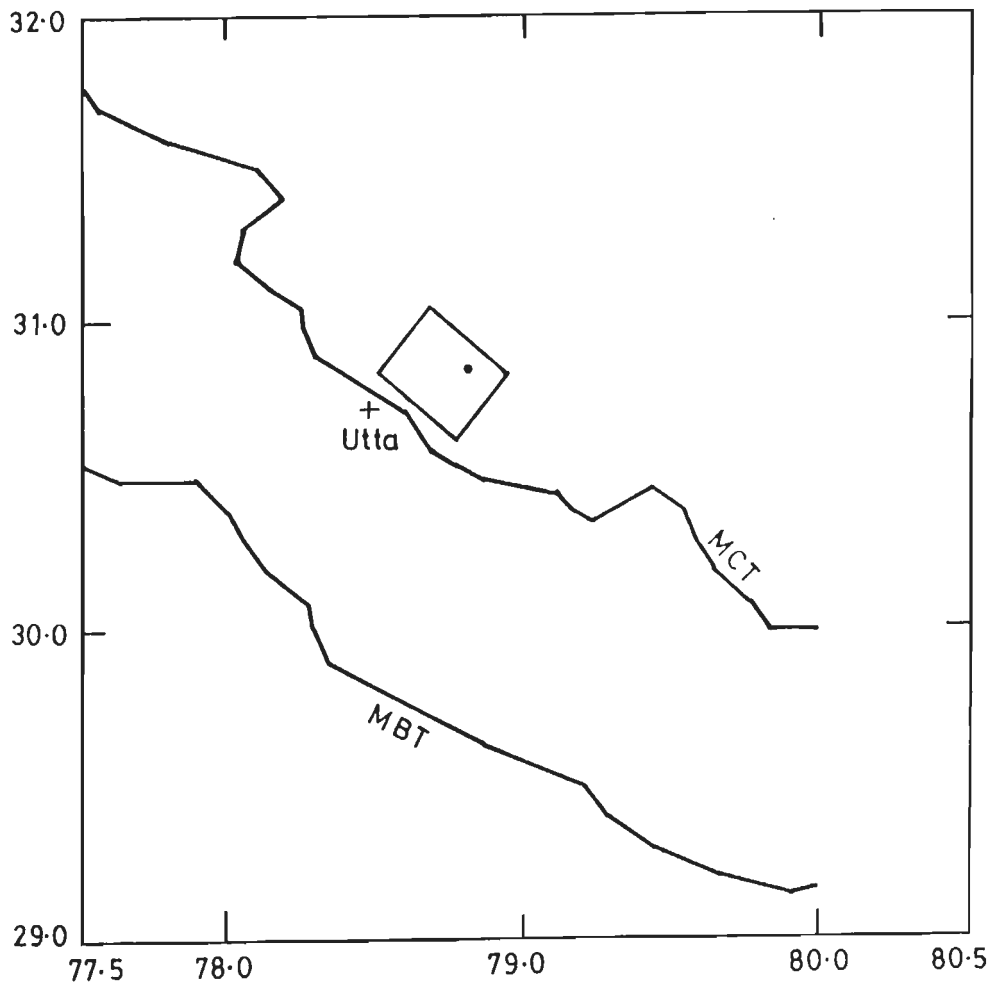


Fig 4.9 Rectangle shows the trace of fault plane in relation to the tectonic features (MCT and MBT) which has been used for generating synthetic accelerograms , utta: Uttarkashi

from the analysis of strong motion data by waveform modelling. An examination of the relevant source parameters in Table 4.1 reveals that the fault plane geometry (i.e., dip and strike) remains unchanged whereas the slip angle is slightly different. The estimate of the seismic moment (1.00×10^{26} dyne-cm) also compares favourably well with that obtained from the teleseismic data. The corresponding moment magnitude (6.63) is also very close to the reported value (6.8). It can be surmised that the gross source parameters have remained the same. It is the other source parameters like rise time, rupture velocity and slip distribution which are better predicted through the analysis of strong motion data.

The different stages of the computation of synthetic accelerograms by waveform modelling has brought the following point into attention : location of the point of rupture initiation (i.e., the focus), rupture velocity, rise time and distribution of slip amplitude on the fault plane are the most critical parameters to be carefully considered in the generation of synthetic accelerograms and comparison of generated waveforms with the observed ones.

The slip distribution over the fault indicates that the area of the fault which contributes to the large amplitudes of recorded accelerations is a small fraction of the total area. On

this portion of the fault the slip amplitudes are high. These regions of the fault have been termed asperities. Most of the seismic wave energy takes place from such asperities. The complexity of observed accelerograms depends on the size and number of such asperities. There is no simple method or mathematical relation available to find the slip distribution over the fault plane and locations of the asperities. In the present work the study of aftershock data has been used to find the slip distribution model. A different technique will have to be evolved to determine slip distribution when aftershock data are meagre or not available.

A contour map of the final slip distribution over the fault is shown in Fig. 4.1. It shows two asperities at 2.44s and 3.78 s. The two asperities are nearly contiguous. The larger asperity at 3.78s lies to the west of the hypocenter and contributes larger amplitudes in the recorded accelerograms. The largest value of the slip is 175 cm and the average slip is 87 cm. The total area of the fault plane is 384 km² of which the smaller asperity covers 16 km² and the larger asperity covers 22 km² which makes of a total of 38 km². The rest of the 346 km² does not contribute much to the radiated energy.

The two asperities on the fault plane occupy those

regions in which the slip amplitude is more than 50 cm. The rupture front takes about 4 sec to cover these asperities which is also found to be the duration of those portions of the recorded accelerograms where amplitudes are high, especially at those stations which are nearer to the epicenter like Uttarkashi and Bhatwari.

The rise time of 0.25s found in the present work results in a good quality match of the waveforms. This value comes close to the value of 0.3s found by Khattri et al. (1994) for this earthquake.

CHAPTER 5

CONCLUSIONS

In the present work synthetic accelerograms have been generated for the Uttarkashi earthquake of October 19, 1991 by waveform modelling. A simple geometric ray theory and Green's function approach was used for this purpose. The generated accelerograms were compared with the observed ones at seven selected stations where accelerograms were recorded. The following conclusions are drawn on the basis of the present study.

- (i) The Uttarkashi earthquake is caused by a low angle thrust fault consistent with the prevalent view about the tectonics of the Garhwal Himalaya.

- (ii) The gross features of the source like earthquake size, source geometry and slip angle as determined from teleseismic data remain largely unchanged when strong motion data is analyzed and interpreted. However, other parameters like rise time, rupture velocity and source size can be better determined on the basis of waveform modelling of the strong motion data.

- (iii) In the present study synthetic accelerograms have been

generated using the geometric ray theory and far field Green's function approach in a homogeneous half space. This has resulted in a good match between the observed and synthetic waveforms which highlights the usefulness of the present approach for waveform modelling of strong motion data for determining source parameters. The results obtained in the present work compare favourably well with those found by other workers.

- (iv) A moderate sized earthquake like the Uttarkashi earthquake of October 19, 1991 is generated by large slip amplitudes over a rather small region of the fault plane.

SUGGESTIONS FOR FUTURE WORK

For obtaining better match between the observed and synthetic waveforms, presence of near surface inhomogeneous layers, effect of topography near the recording station and a somewhat more complex source models should also be taken into account.

REFERENCES

- Abrahamson, N. A. and B. A. Bolt, (1986), Array Analysis and Synthesis Mapping of Strong Seismic Motion, Ch. 2. In Seismic Strong Motion Synthetics, B.A.Bolt (Ed.), Academic Press, INC. (London), pp.55-88.
- Abrahamson, N. A., P. G. Somerville and C. A. Cornell, (1990), Goodness of Fit for Numerical Strong Motion Simulations and Uncertainty in Numerical Strong Motion Predictions, Proc. 4th US National Conference on Earthquake Engineering, Palm springs, Vol. 1, pp.317-326.
- Aki, Keiiti and Paul G. Richards, (1980), Quantitative Seismology: Theory and Methods, W. H. Freeman and Company, San Francisco, vols 1&2.
- Aki, Keiiti, (1968), Seismic Displacement Near a Fault, Jour. Geophys. Res. Vol. 73, pp. 5359-5376.
- Barker, J. S., P. G. Somerville and J. P. McLaren, (1988), Modeling of Ground Motion Attenuation in Eastern North America, Electric Power Research Institute Report NP-5577,414p.
- Barker, J. S., P. G. Somerville and J. P. McLaren, (1989), Modeling Ground Motion Attenuation in Eastern North America, Tectonophysics, Vol.167, pp.139-149.
- Ben-Menahem, Ari, and Sarva Jit Singh, (1981), Seismic Waves and Sources, Springer-Verlag New York Inc. pp. 1108.
- Boore, D. M., and W. B. Joyener, (1978), The Influence of Rupture Incoherence on Seismic Directivity Bull. of Seism. Soc. America, Vol. 68, pp. 283-300.
- Bouchon, M., (1979), Predictability of Ground Displacement and Velocity Near an Earthquake Fault : An eample : the Parkfield Earthquake 1966 , Jour. Geophys. Res., Vol. 84, pp. 6149-6156.
- Burridge, R., and G. S. Halliday, (1971), Dynamic Shear Cracks with Friction as Models for Shallow Focus Earthquakes Geophys. J. R. Astron. Soc. ,Vol. 25, pp. 261- 283.

- Burridge, R. and L. Knopoff, (1964), Body Force Equivalents for Seismic Dislocations, Bull. of Seism. Soc. America, Vol. 54, pp. 1875-1888.
- Chadha, R.K., (1995), The Uttarkashi Earthquake of October 20, 1991 in Northern India : A Seismotectonic Model based on Field Observations. In Gupta, H.K. and G.D. Gupta (Ed.), Uttarkashi Earthquake (20th October, 1991), Memoir 30 of the Geological Society of India, Bangalore (India), pp.75-82.
- Chandra, B., Ashok Kumar and M.K. Bansal (1995) A study of Strong Motion Data obtained during Uttarkashi Earthquake of Oct. 20, 1991 from INSMIN network in Gupta, H.K. and G.D. Gupta(Ed.) (1995) Uttarkashi Earthquake (20th October, 1991) Memoir 30 of the Geological Society of India, Bangalore (India), pp.149-158.
- Chandrasekaran, A. R., and J. D. Das, (1992a) Strong Motion Arrays in India and Characteristics of Recent Recorded Events , Memoir Geol. Soc. India Vol. 23, pp. 81-122.
- Chandrasekaran, A. R., and J. D. Das, (1992b) Analysis of Strong Motion Accelerograms of Uttarkashi Earthquake of October 20, 1991, Paper No. 315, Bulletin of the Indian Society of Earthquake Technology, Vol. 29, No. 1, March, pp. 35-55.
- Das, S. and K. Aki, (1977a), A Numerical Study of Two-dimensional Spontaneous Rupture Propagation , Geophys. Jour. R. A. Soc., Vol. 50, pp. 643-668.
- Das, S., and K. Aki, (1977b), Fault Plane With Barriers : A Versatile Earthquake Model, Geophys. Jour. R. A. Soc., Vol. 82, pp. 5658-5670.
- Fuchs, K, and G. Mueller, (1971), Computation of Synthetic Seismograms with the Reflectivity Method and Comparison with Observation , Geophys. J. R. Astron. Soc., Vol. 23, pp. 417-433.
- Gansser, A (1964). Geology of The Himalaya, Inter Science, New York, pp. 298.
- Gupta, H.K. and G.D. Gupta(Ed.) (1995) Uttarkashi Earthquake (20th October, 1991) Memoir 30 of the Geological Society of India, Bangalore (India), pp.233.

- Hadley, D. M., and D. V. Helmberger, (1980), Simulation of Strong Ground Motion, Bull. of Seism. Soc. America, Vol. 70, pp. 617-630.
- Hartzell, S. H., (1978), Earthquake Aftershocks as Green's Function, Geophys. Res. Letter, Vol. 5, pp. 1-4
- Haskell, N. A., (1966) Total Energy and Energy Spectral Density of Elastic Wave Radiation from Propagating Faults, Bull. of Seism. Soc. America, Vol. 59, pp. 865-908.
- Haskell, N. A., (1969) Elastic Displacements in the Near Field of a Propagating Fault, Bull. of Seism. Soc. America, Vol. 59, pp. 865-908.
- Heaton, T. H., and D. V. Helmberger, (1977), A Study of the Strong Motion of the Borrego Mountain, California Earthquake, Bull. of Seism. Soc. America, Vol. 67, pp. 315-330.
- Heaton, T. H., and D. V. Helmberger, (1978), Predictability of Strong Ground Motion in the Imperial Valley: Modeling the M 4.9 November 4, 1976 Brawley Earthquake, Bull. of Seism. Soc. America, Vol. 68, pp. 31-48.
- Helmberger, D. V., (1968), The Crust-mantle Transition in the Bering Sea, Bull. of Seism. Soc. America, Vol. 58, pp. 179-214.
- Helmberger, D.V. and D.G. Harkrider (1978) Modeling Earthquakes with Generalized Ray Theory. In Modern Problems in Elastic Wave Propagation, (Eds.) J. Miklovitch and J.D. Achenbach, Wiley, New York, pp. 499-518.
- Herrmann, R. B., (1977), Final Rep., Contact DACW 39-76-C-0058. Waterways Exp. Stn., Vicksburg, Mississippi.
- Ida, Y, and K. Aki, (1972), Cohesive Force Across the Tip of a Longitudinal-Shear Crack and Griffith's Specific Surface Energy, Jour. Geophys. Res., Vol. 77, pp. 3796-3805.

- Jain, A.K. and Ramesh Chander, (1995), Geodynamic Models for the Uttarkashi earthquake of October 20, 1991 in Gupta, H.K. and G.D. Gupta (Ed.) (1995) Uttarkashi Earthquake (20th October, 1991) Memoir 30 of the Geological Society of India, Bangalore (India), pp.225-233.
- Jain, S.K. and Satrajit Das, (1995), A study of Uttarkashi Accelerograms and its implications for India Seismic Code in Gupta, H.K. and G.D. Gupta (Ed.) (1995) Uttarkashi Earthquake (20th October, 1991) Memoir 30 of the Geological Society of India, Bangalore (India), pp.159-171.
- Kasahara, K, (1981), Earthquake Mechanics, Cambridge University Press, pp.248
- Kayal, J. R., Bimon Ghosh, P. Chakrobarati and Reena De, 1995, Aftershock Study of the Uttarkashi Earthquake of October 20, 1991 by a Temporary Microearthquake Network, Memoir Geological Survey of India, No.30, 1995, pp.25-41.
- Khattari, K. N. (1992a) Local Seismic Investigations in the Garhwal-Kumaon Himalaya, Memoir Geol. Soc. India Vol. 23, pp. 45-66.
- Khattari, K. N. (1992b) Seismological Investigations in North eastern region of India, Memoir Geol. Soc. India Vol. pp. 275-302.
- Khattari, K. N., Y. Zeng, J. G. Anderson and J. Brune (1994) Inversion of Strong Motion Waveforms of Source Slip Function of 1991 Uttarkashi Earthquake, Himalaya, Journal of Himalayan Geology, vol. 5(2), pp. 163-191.
- Kostrov, B. V., (1966), Unsteady propagation of Longitudinal Shear Cracks Jour. Appl. Math. Mech. (Engl. Transl.), Vol. 30, pp. 1241-1248.
- Lee and Stewart (1981) Principles and Applications of Microearthquake Networks, Academic Press
- Madariaga, R., (1976), Dynamics of an expanding circular fault Bull. of Seism. Soc. America, Vol. 66, pp. 639-666.

- Makaris, D. I., G. N. Stavrakakis and J. C. Drakopoulos, (1992), Expected Ground Motion at a Site Based on Hypothetical Fault Models, Earthquake Engineering, Tenth World Conference , Vol. 2, Balkema, Rotterdam, pp. 703-708.
- Maruyama, T., (1963), On the Force Equivalents of Dynamical Elastic Dislocations With Reference to the Earthquake Mechanism, Bull. Earthquake Res. Inst. , Tokyo Univ., Vol. 41, pp. 467-486.
- Mendoza, C. and S. Hartzell, (1988), Inversion For Slip Distribution Using Teleseismic P-Waveforms , North Palm Springs, Borah Peak and Michoacan Earthquakes, Bull. of Seism. Soc. America, Vol. 78, pp. 1092-1111.
- Mikumo, T. and T. Miyatake, (1978), Dynamical Rupture Process on a Three Dimensional Fault with Non-uniform Frictions and Near Field Seismic Waves, Geophys. J. R. Astron. Soc., Vol. 54, pp. 417-438.
- Mikumo, T. and T. Miyatake, (1987), Numerical Modelling of Realistic Fault Rupture Process, pp. 109-146. in Bolt, B.A., (Ed.) "Seismic Strong Motion Synthetics" Academic Press Inc., pp. 328.
- Narula, P.L., S.K. Shome, S. Kumar and Prabhas Pande, (1995), Damage patterns and Delineation of Isoseismals of Uttarkashi Earthquake of 20th October, 1991 in Gupta, H.K. and G.D. Gupta (Ed.) (1995) Uttarkashi Earthquake (20th October, 1991) Memoir 30 of the Geological Society of India, Bangalore (India), pp. 1-17.
- Ni, J. and M. Barazangi, (1984), Seismotectonics of the Himalayan Collision Zone : Geometry of the Underthrusting Indian Plate Beneath The Himalaya, J. Geophys. Res., Vol. 89, pp. 1147-1163.
- Olson, A. H., (1982), Ph. D. Thesis, Univ. of California, San Diego PDE, (1991), Preliminary Determination of Epicenters, No. 42-91, U. S. Department of the Interior, Geological Survey.
- PDE, (1991), Preliminary determination of epicenters, No. 42-91, US department of interior, Geological Survey.
- Rastogi, B. K., (1995), Seismological Studies of Uttarkashi Earthquake of October 20, 1991, Memoir Geological Survey of India , No. 30, 1995, pp. 43-50.

- Rastogi, B.K. and R.K. Chadha (1995) Intensity and Isoseismals of Uttarkashi Earthquake of October 20, 1991 in Gupta, H.K. and G.D. Gupta (Ed.) (1995) Uttarkashi Earthquake (20th October, 1991) Memoir 30 of the Geological Society of India, Bangalore (India), pp.19-24.
- Richter, C. F., (1958), Elementary Seismology, W.H. Freeman and Co., San Fransisco, pp.768
- Somerville, Paul G., James P. McLaren, Chandan K Saikia and Donald V. Helmberger (1990) The 25 November 1988 Saguenay, Quebec, Earthquake: Source Parameters and the Attenuation of Strong Ground Motion, Bull. of Seis. Soc. of America, Vol. 80, No. 5, pp. 1118-1143.
- Somerville, Paul G., M. Sen and B. Cohee, (1991), Simulation of Strong Ground Motions Recoding During the 1985 Michocan Mexico, and Valpazaiso Chili Earthquake, Bull. of Seis. Soc. of America, Vol. 81, No. 1, pp. 1-27.
- Swanger, H. J., and D. M. Boore , (1978), Simulation of Strong Motion Displacements using Surface Wave Model Superposition, Bull. of Seism. Soc. America, Vol. 68, pp. 907-922.
- Wald, David J, Donald V. Helmberger and Thomas H. Heaton, (1991), Rupture Model of the 1989 Loma Prieta Earthquake From the Inversion of Strong Motion and Broadband and Teleseismic data , Bull. of Seis. Soc. of America , Vol. 81, No. 5, pp.1540-1572.
- Yu, G., K. N. Khattri, J. G. Anderson, J. N. Brune and Y.Zeng, (1995), Strong Ground Motion from the Uttarkashi, Himalaya, India, Earthquake: Comparison of Observations with Synthetics Using the Composite Source Model, Bull. of Seis. Soc. of America , Vol. 85, No. 1, pp. 31-50.
- Zeng, Y., K. Aki and L. Teng, (1993a), Source Inversion of the 1987 Whittier Narrows earthquake, California, using the Isochrone Method, Bull. of Seis. Soc. of America, Vol. 83, pp. 358-377.
- Zeng, Y., K. Aki and L. Teng, (1993b), Mapping of the high frequency source radiation for the Loma Prieta earthquake, California, Bulletin of Seismological Society of America, Vol. 98, pp. 11981-11993.

- Zeng, Y., J. G. Anderson and G. Yu, (1994a), A composite Source Model for Computing Realistic Synthetic Strong Ground Motions, Geophys. Res. Lett., Vol. 21, pp. 725-728.
- Zeng, Y., J. G. Anderson and F. Su, (1994b), Source and Path Effects in Realistic Strong Ground Motion Simulation (abstract), Seism. Res. Lett., Vol. 65, 36p.